NTNU – Trondheim
Norwegian University of
Science and Technology

Modeling of a 1,2-Dichloroethane Cracker

Ingrid Nyeng

Chemical Engineering and Biotechnology
Submission date: June 2015
Supervisor: Tore Haug-Warberg, IKP

Norwegian University of Science and Technology
Department of Chemical Engineering

ABSTRACT

Polyvinyl chloride (PVC) is the second most widely used synthetic polymer plastic, where the largest consumption is in the building and construction sector. PVC is mainly produced through the polymerization of the monomer vinyl chloride (VCM), which is formed through the process of thermal dehydrochlorination (*cracking*) of 1,2-dichloroethane (EDC). One such cracker reactor is operated by INEOS in Porsgrunn, which is part of their VCM plant at the Rafnes site. Operation of this EDC cracker requires the largest heat input of all the units in the VCM plant, and is thus of special interest with respect to optimization of the plant.

In this study a simulation model for EDC cracking has been developed, which is based on a plug flow reactor (PFR) model and includes coupling of a heat transfer model with a kinetic model. Two kinetic models were implemented; one *global* kinetic model and one more *extensive* radical chain reaction model, where important byproducts in addition to one promotor and one inhibitor are included. The extensive kinetic model is based on a reaction mechanism developed by Schirmeister et al., which involves 31 reactions and 24 species. The developed heat transfer model includes radiative and convective heat transfer from the surrounding flue gas in the cracking furnace to the reaction coils.

Simulations were performed with regard to model verification and validation, and to evaluate the effect of temperature, promotor and inhibitor on the cracking process. In general, the developed simulation model is in good agreement with plant data from INEOS. The simulations suggest that an increase in temperature gives an increase in conversion and consequently a larger byproduct formation. A great sensitivity with respect to the feed concentration of the promotor, carbon tetrachloride (CCl_4), is observed for the extensive kinetic model. With increased inlet concentration of the promotor, the conversion and byproduct formation are increased, while the selectivity is observed to decrease. No clear effect of the inhibitor, 1,1-dichloroethane (1,1-EDC) is detected for the implemented extended kinetic model. The simulations indicate that the byproduct formation in the adiabatic volume (the last part of the reactor) is large, which illustrates the tradeoff between operating at high conversions and production rates of VCM, and maintaining a high selectivity and purity of the product.

SAMMENDRAG

Polyvinylklorid (PVC) er en polymer som brukes i PVC-plast og er den nest mest anvendte av alle plasttyper, hvorav den mest utstrakte bruken er i bygg- og anleggsbransjen. Polymeren fremstilles hovedsakelig ved friradikalpolymerisasjon av monomeren vinylklorid (VCM), som dannes ved termisk dehydroklorering (*cracking*) av 1,2-dikloretan (EDC). Cracking av EDC krever den største varmetilførselen av alle enhtetene i VCM-fabrikken, og denne reaktoren er derfor av spesiell interesse med tanke på optimalisering av fabrikken.

Gjennom arbeidet med denne masteroppgaven er det blitt utviklet en simuleringsmodell for en EDC-cracker, som er basert på en stempelstrømraktormodell, der en kinetikkmodell er koblet med en varmeoverføringsmodell. To kinetikkmodeller er implementert; henholdsvis én global reaksjonsmodell tilpasset fabrikkdata og én mer avansert kinetikkmodell fra litteraturen. Den utviklede varmemodellen inkluderer varmeoverføring i form av stråling og konveksjon til reaksjonsrørene, som befinner seg i et brennkammer.

Simuleringer med den utviklede modellen ble utført med tanke på modellverifikasjon og modellvalidering, samt for å evaluere effekten av temperatur, promotor og inhibitor på cracking-prosessen. Simuleringene er generelt i god overenstemmelse med fabrikkdata. Resultatene fra simuleringene indikerer at en økning i temperatur resulterer i både økt omsetning og økt mengde biprodukter, samt en redusert selektivitet. Den avanserte kinetikkmodellen viser seg også å være sensitiv med hensyn på innløpskonsentrasjon av promotoren karbontetraklorid, CCl_4. Ingen tydelig effekt av inhibitoren 1,1-dikloroetan (1,1-EDC) er funnet for denne spesifikke (avanserte) kinetikkmodellen. Den høye dannelsen av biprodukter i det adiabatiske volumet som er observert i simuleringene, illustrerer kompromisset mellom det å operere ved høy omsetning av EDC og produksjonsrate av VCM, og det å opprettholde en høy selektivitet og ren produktstrøm.

PREFACE

This master thesis was carried out as the final part of the integrated master's degree program in Chemical Engineering and Biotechnology at the Norwegian University of Science and Technology (NTNU). The thesis was completed during the spring semester 2015, at the Process Systems Engineering group at the department of Chemical Engineering. The work has been performed in cooperation with INEOS Norge. Supervising has been provided at NTNU from Associate Professor Tore Haug-Warberg, and externally from co-supervisor Torbjørn Herder Kaggerud from INEOS.

Declaration of compliance

I hereby declare that this is an independent work according to the exam regulations of the Norwegian University of Science and Technology.

Trondheim, 11.06.2015

INGRID NYENG

ACKNOWLEDGEMENT

First of all I wish to express appreciation for the help provided from my supervisors on this thesis. Associate Professor Tore Haug-Warberg has given invaluable guidance throughout the semester, and his theoretical insight into applied thermodynamics has been inspirational and important for the conducted work.

I also wish to express my gratitude towards Torbjørn Herder Kaggerud, for giving me the opportunity to work on this thesis in the first place. I have been met in a positive, enthusiastic and helpful way from first starting on this project, this also includes the other coworkers at INEOS. Help has been provided efficiently, despite the distance between Porsgrunn and Trondheim. I appreciate the visits Torbjørn had in Trondheim to provide help, and also the visits I had in Porsgrunn. It was interesting and helpful being able to actually see the plant I was modeling, and to talk to experts at INEOS. I would also like to thank John Morud and Magne Hillestad for useful input in meetings during the spring semester.

My classmates and friends deserve loads of credit for making the years in Trondheim unforgettable. During the master thesis, I would especially like to thank the guys at K4-320 (*lesesalen*) for help, support and cooperation on difficult tasks.

Last, but not least I would like to thank my family for support and encouragement, and for inspiring me to choose the best city to conduct my studies.

CONTENTS

LIST OF FIGURES

LIST OF TABLES

NOMENCLATURE

Abbreviations

BDF	Backward differentiation formulas
CFD	Computational fluid dynamics
EDC	1,2-dichloroethane (ethylene dichloride)
ODE	Ordinary differential equation
PFR	Plug flow reactor
PVC	Polyvinyl chloride
SNB	Statistical Narrow Band
VCM	Vinyl chloride monomer
WSGGM	Weighed sum of gray gases model

Greek symbols

α	Absorptivity	-
α	Thermal diffusivity	$\mathrm{m^2\,s^{-1}}$
ε	Emissivity	-
ζ	Spatial integration variable	-
λ	Excess air coefficient	-
ν	Kinematic viscosity	$\mathrm{m^2\,s^{-1}}$
ν	Stoichiometric coefficient	-
μ	Dynamic viscosity	$\mathrm{kg\,m^{-1}\,s^{-1}}$
$\dot{\boldsymbol{\xi}}$	(Vector of) specific reaction rates	$\mathrm{mol\,m^{-3}\,s^{-1}}$
ρ	Density	$\mathrm{kg\,m^{-3}}$
ρ	Reflectivity	-
σ	Stefan Boltzmann's constant	$\mathrm{W\,m^{-2}\,K^{-4}}$
τ	Space time	s
τ	Transmittivity	-

Latin symbols

A	Area	m^2
A	Frequency factor	s^{-1}
$\mathbf{c}$	(Vector of) moles per mass	$\mathrm{mol\,kg}^{-1}$
C	Circumference	m
C_p	Heat capacity	$\mathrm{J\,mol}^{-1}\,\mathrm{K}^{-1}$
d	Diameter	m
$\dot{E}$	Transported energy	$\mathrm{J\,s}^{-1}$
E	Emissive radiation power	$\mathrm{J\,m}^{-2}\,\mathrm{s}$
E	Energy	J
E_a	Activation energy	$\mathrm{J\,mol}^{-1}$
E_k	Kinetic energy	J
E_p	Potential energy	J
G	Generation	$\mathrm{mol\,s}^{-1}$
$\Delta H_\mathrm{f}^\circ$	Enthalpy (molar) of formation	$\mathrm{J\,mol}^{-1}$
h	Convection coefficient	$\mathrm{J\,s}^{-1}\,\mathrm{m}^{-2}\,\mathrm{K}^{-1}$
h	Specific enthalpy	$\mathrm{J\,mol}^{-1}$
$\dot{h}$	Transported enthalpy	$\mathrm{J\,s}^{-1}$
H	Enthalpy	J
$\mathbf{I}$	Identity matrix	-
k	Specific reaction rate constant	$\mathrm{mol\,m}^{-3}\,\mathrm{s}^{-1}$
k	Thermal conductivity	$\mathrm{J\,s}^{-1}\,\mathrm{m}^{-2}\,\mathrm{K}^{-1}$
$\mathbf{J}$	Jacobian matrix	-
L	Characteristic length	m
n	Mole	mol
$\dot{n}$	Mole flow	$\mathrm{mol\,s}^{-1}$
$\mathbf{N}$	Stochiometry matrix	-
Nu	Nusselt number	-
$\dot{M}$	Mass flow	$\mathrm{kg\,s}^{-1}$
p	Pressure	bar
Pr	Prandtl number	-
$\dot{Q}$	Heat rate	$\mathrm{J\,s}^{-1}$
$\dot{q}$	Heat flux	$\mathrm{J\,m}^{-2}\,\mathrm{s}^{-1}$
q	Heat (energy) per mass	$\mathrm{J\,kg}^{-1}\,\mathrm{m}^{-2}$
R	Ideal gas constant	$\mathrm{J\,K}^{-1}\,\mathrm{mol}^{-1}$
$\mathbf{r}$	Specific reaction yield (vector)	$\mathrm{mol\,m}^{-3}\,\mathrm{kg}^{-1}$
Re	Reynolds number	-
s	Selectivity	-

The list continues on the next page

T	Temperature	K
t	Time	s
$\dot{U}$	Transported internal energy	J
U	Internal energy	J
V	Volume	$\mathrm{m^3}$
$\dot{V}$	Volume flow	$\mathrm{m^3\,s^{-1}}$
v	Velocity	$\mathrm{m\,s^{-1}}$
v	Specific volume	$\mathrm{m^3\,kg^{-1}}$
$\dot{W}$	Work (rate)	$\mathrm{J\,s^{-1}}$
W_s	Shaft work	$\mathrm{J\,s^{-1}}$
x^c	Conversion, molar basis	-
x^w	Conversion, mass basis	-
x	Mole fraction	-
$\mathbf{x}$	Vector of primary state variables	-
z	Axial coordinate	-

Superscripts and subscripts

0	Initial value
f	Flue gas
i	Species i
ig	Ideal gas
p	Process gas
pi	Pipe, inner
po	Pipe, outer
rx	Reaction
vap	Vaporization
z	At position/coordinate z

Chapter 1

Introduction

Polyvinyl chloride (PVC) is the second most widely used synthetic polymer plastic, after polyethylene [1]. The monomer of PVC, vinyl chloride monomer (VCM), was first discovered in 1835. However, the application of the plastic was first described in a patent from 1913 [2]. Commercial uses of the polymer began in the 1930s, after B.F. Goodrich Company started blending the polymer with several additives, yielding a more easily processed and flexible material [3]. Currently, PVC has a wide range of applications. The widest use is in the building and construction sector, where it is used for e.g. waste water pipes and window frames [3]. Other applications are insulation of electrical cables, packaging and flooring.

PVC is prepared from polymerization of VCM, the latter is produced industrially through two processes; thermal dehydrochlorination[1] (*cracking*) of 1,2-dichloroethane (EDC) under high temperatures and hydrochlorination of acetylene. Currently EDC pyrolysis is the main commercial route, accounting for more than 90% of the VCM production worldwide [4]. One such production site is located at Rafnes, Norway, where the petrochemical company INEOS ChlorVinyls is operating three EDC cracking reactors, as part of their VCM plant. These EDC crackers are the main focus of this study.

1.1 Modeling of EDC pyrolysis

To run the VCM plant at the optimal operational conditions, both economically and in terms of energy efficiency, a simulation model is beneficial. The optimization of the plant includes tradeoffs between EDC cracker heat load versus de-coking intervals, the distillation operation and the EDC purity, and the energy consumption and efficiency of the VCM plant. The EDC cracker is

---

[1] Dehydrochlorination of 1,2-dichloroethane is also be referred to as *cracking* or *pyrolysis* of 1,2-dichloroethane.

of special interest in the optimization, as this unit has the highest heat input of all the units in the plant (about 65% of the total heat input to the plant). Therefore, the aim is to develop a simulation model of this specific unit. To be able to quantify and understand the effect of different operational parameters on the EDC cracking process, a robust model which includes heat, mass and momentum balances is necessary. A robust model is taken to be one that is numerically stable and a model which can run simulations for a wide range of input values.

Previously, several studies on the kinetics of EDC cracking have been performed, where different reactions mechanisms for the pyrolysis reactions have been suggested. These models vary in the number of reactions, and hence complexity. Also the heat transfer in the cracker furnace has been studied in detail, using e.g. computational fluid dynamics (CFD) simulations. At this point it is desired to develop a simulation model of the reactions in the EDC cracker and the heat transfer to the cracker. The cracker process can be modeled as a plug flow reactor (PFR), with heat transfer mainly in the form of radiation.

1.2 Main objectives

The master thesis is carried out as a part of the Chemical Engineering study at Norwegian University of Science and Technology (NTNU), and the work serves several purposes. First of all, the model is developed in cooperation with INEOS, which can be used in simulation of their industrial VCM plant. Secondly, the model is built on an already existing PYTHON program made for a modelling course at NTNU, *TKP4106 - Process Modeling*, developed by Associate Professor Tore Haug-Warberg. This program is used as a framework for the implementation of kinetic reaction mechanisms and a heat transfer model.

The given modelling objectives from INEOS are listed below.

1. Establish a reactor simulation model with simplified kinetics for EDC cracking, using data from the INEOS pilot EDC cracker. The model should preferably be a Plug Flow Reactor model, but an isothermal and isobar batch reactor model may be used.

   (a) Tune the reaction mechanism parameters to match pilot cracker data.

   (b) Include one initiator (carbon tetrachloride) and one inhibitor (1,1-dichloroethane) to the reaction mechanism.

2. Simulation of an industrial reactor with the model developed in part 1.

   (a) Evaluate effects of temperature profile, promotor and inhibitor on conversion and byproduct formation.

(b) Evaluate effect of process parameters on cracking under adiabatic conditions.

Additionaly, the scope of work includes model *validation* and *verification.* Verification in this case means testing that the code performs the tasks it is asked to do. Included in the validation part is comparing the output data from the model against plant data.

1.3 Literature survey

Several studies have been performed with regard to the development of kinetic models of EDC pyrolysis. Among these are Schirmeister et al.'s kinetic model appearing in the article *Influence of EDC Cracking Severity on the Marginal Costs of Vinyl Chloride Production* [5], which is the kinetic model the reaction model in this thesis is built upon. Other publications; E.g. Borsa's doctoral thesis from 1999, *Industrial Plant/Laboratory Investigation and Modeling of 1,2-dichloroethane Pyrolysis* [6], as well as publications from Choi et al. [7], Ranzi et al. [8] among others, have also been used as references for the part of the thesis covering reaction kinetics. A more extensive literature survey which covers the kinetic models is given in Chapter 2.

The main literary sources of the heat transfer theory applied in the thesis are Incropera, Dewitt et al.s *Fundamentals of Heat and Mass Transfer* [9], Geankoplis' *Transport Processes and Separation Process Principles* [10] and Bird et al.s *Transport Phenomena* [11]. The theory behind the thermodynamic state equations used in the framework model in the developed PYTHON program is elaborated in Warberg's *Den termodynamiske arbeidsboken* [12].

1.4 Structure of the report

The thesis is divided in three main parts; where the first part covers the *theory* behind pyrolysis of EDC and the kinetic and heat transfer models, which is found in Chapter 1, 2, 3 and 4. The second part elaborates on the *model development*, which covers the *overall* model development, the kinetic model, and the heat transfer model, described in Chapter 5, 6 and 7. Lastly, the results are presented in Chapter 8.

Chapter 2

Pyrolysis of 1,2-dichloroethane

This chapter is focused on the vinyl chloride monomer (VCM) plant and the pyrolysis reactor (the *cracker*[1]). Also, a literature review of the studies which previously have been conducted on the modelling of 1,2-dichloroethane (EDC) pyrolysis is given, with focus on the development of kinetic models, byproducts, inhibitors and promotors.

2.1 From gas to plastics

INEOS is a petrochemical company located in 11 countries worldwide. At Grenland in Norway, gas from the North Sea is converted into plastic raw materials. The process steps going from gas to finalized plastic products utilized by end users are illustrated in Figure 2.1.

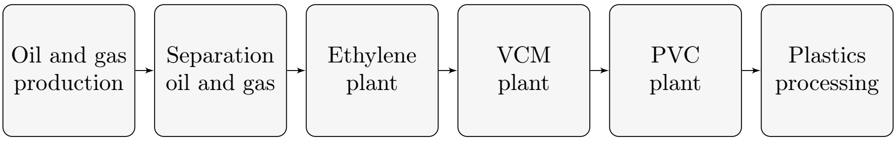

Figure 2.1. The petrochemical path from produced oil and gas to produced plastic.

As indicated in the figure, the whole process begins with the extraction of petroleum in the form of of crude oil and gas. The produced oil and gas goes through separation and purification, and is then ready for delivery at Noretyl's ethylene plant (cracker) at Rafnes, where ethylene is produced. Most of this

---

[1] Cracking is a process where organic molecules are decomposed to lighter molecules, usually hydrocarbons, by braking carbon-carbon bonds. In cracking, the decomposition of the molecules are induced by heat addition or presence of catalysts or solvents.

ethylene is transferred to INEOS' VCM plant, where the ethylene reacts with chlorine to produce VCM, via the process of EDC cracking. VCM is then transferred in pipes to the PVC plant at Herøya in Porsgrunn, to further react to PVC. The polymerization reaction is found in equation 2.1.

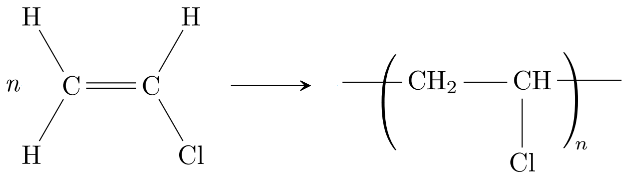

(2.1)

In this equation, the left hand side are the n monomers of vinyl chloride forming a polymer of PVC. Finally, the produced PVC is processed and converted into a wide range of products such as pipes and packaging [3].

2.2 The VCM plant

In the VCM plant the raw materials are salt, water, ethylene and oxygen, resulting in produced VCM, in addition to the side products hydrogen gas and sodium hydroxide (NaOH). A schematic flow sheet of the VCM plant is shown in Figure 2.2.

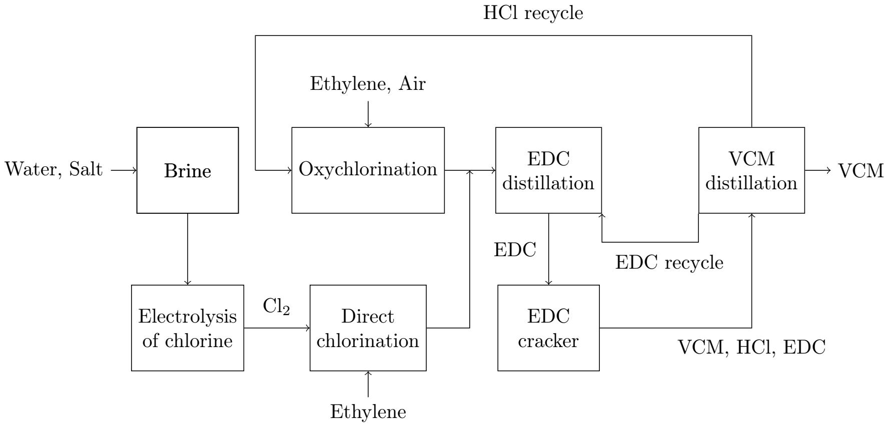

Figure 2.2. Schematic of the VCM plant.

As seen in Figure 2.2, the first step of the process is the *electrolysis* of salt (NaOH) and water to produce chlorine (Cl_2). Production of chlorine takes place at the on-site electrolysis plant. First the salt is dissolved in water to form a brine, which is converted to chlorine in the electrolysis cell. Electrolysis produces two side products, hydrogen gas and sodium hydroxide, as the overall equation shows. Hydrogen gas can be used as fuel gas, while the sodium hydroxide is sold as a product.

The produced chlorine is used in the *direct chlorination* process, which yields EDC. *Oxychlorination* also yields EDC, from the recycled HCl produced in the EDC cracker. In the EDC cracker, EDC is pyrolysed to VCM and HCl at high temperatures. The products are sent through several distillation units, to separate VCM, HCl and unreacted EDC. The separated HCl is recycled to the oxychlorination unit, EDC is recycled to the cracker and the VCM is sent to storage units.

The main chemical steps of the VCM plant

The corresponding chemical reactions to the presented VCM process are listed below, with the molar enthalpies of reaction [13].

1. Chlorine electrolysis:

$$2\mathrm{NaCl} + 2\mathrm{H_2O} \rightarrow \mathrm{Cl_2} + \mathrm{H_2} + 2\mathrm{NaOH} \qquad \Delta_{\mathrm{f}}H^{\ominus} = -1181\,\mathrm{kJ\,mol^{-1}} \tag{2.2}$$

2. Direct chlorination of ethylene to EDC:

$$\mathrm{C_2H_4} + \mathrm{Cl_2} \rightarrow \mathrm{C_2H_4Cl_2} \qquad \Delta_{\mathrm{f}}H^{\ominus} = -218\,\mathrm{kJ\,mol^{-1}} \tag{2.3}$$

3. Oxychlorination of ethylene (and HCl recovery) to EDC:

$$\mathrm{C_2H_4} + 2\mathrm{HCl} + 0.5\mathrm{O_2} \rightarrow \mathrm{C_2H_4Cl_2} + \mathrm{H_2O}\, \Delta_{\mathrm{f}}H^{\ominus} = -295\,\mathrm{kJ\,mol^{-1}} \tag{2.4}$$

4. Thermal cracking (pyrolysis) of EDC to VCM:

$$\mathrm{C_2H_4Cl_2} \rightarrow \mathrm{C_2H_3Cl} + \mathrm{HCl} \qquad \Delta_{\mathrm{f}}H^{\ominus} = 71\,\mathrm{kJ\,mol^{-1}} \tag{2.5}$$

As the molar reaction enthalpies in equation (2.2) to (2.5) indicates, the only endotherm reaction is the pyrolysis reaction. Overall, the process is exothermal, which means that the VCM plant should be able to cover most of its energy needs without external supply. This EDC cracker is the unit which is modeled in this thesis, and will hence be described in more details.

2.3 The EDC cracker

INEOS ChlorVinyls operates several EDC crackers. These include three at the Rafnes site in Norway and one at the Stenungsund in Sweden. In this study, the focus is on the crackers at the Rafnes site. The overall global reaction where EDC is thermally decomposed to VCM is was shown in equation (??).

As the global reaction is endothermic, the reactions require addition of heat to start the thermal decomposition, and to proceed throughout the reactor. Therefore, the tubular reactions coils are places in a furnace. The process is typically operated at pressures between 3 to 30 bar, and the EDC conversion is usually kept at 50-60 wt%. High selectivities are reported in literature for commercial EDC crackers, in the range 96-99% (on a mole basis), regarding VCM [14]. The pipe sizes are designed to ensure a space time of 20-30 s and a gas velocity between 10-20 $\mathrm{m\,s^{-1}}$. A schematic of an EDC cracking reactor, similar in principle (and not dimensions) to the one at Rafnes is illustrated in Figure 2.3.

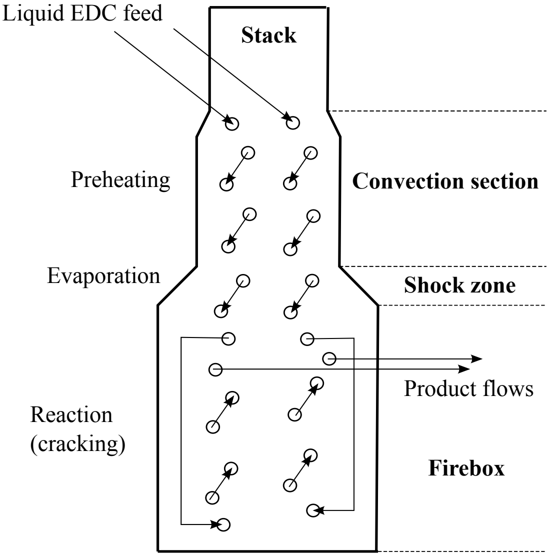

Figure 2.3. Schematic of the EDC cracker.

In the schematic of the cracker, the two parallel coil pipes are going into and out of the plane, seen from the short side of the cracker. Figure 2.3 also illustrates that the EDC cracker can be divided into different zones. The cracker to be studied in this thesis includes the following zones:

- The *convection* section
- The *shock* section
- The *firebox* (reaction zone)
- The *adiabatic volume*

The lowest part of the cracker is the firebox section. Here, the EDC starts to decompose at temperatures between 480-550 °C [13]. With addition of promotors or presence of promotors from upstream operations, the reaction could start at an earlier point. Burners are placed at the long sides of the furnace in the firebox section, supplying heat to the whole cracker. In the burners, a gas mixture of methane, hydrogen and ethane is combusted with an oxygen excess of 15-20%, to give a fired heat of 17.4 MW [15]. Due to the high temperatures in the this section, most of the heat is transferred through radiation. The two parallel pipes are slightly shifted vertically, to minimize shadow effects and maximise the heat absorption to the two coils in the firebox section.

The function of the first zone, the convection section, is to preheat the liquid EDC feed to reach the boiling point. As the name indicates, most of the heat transfer in this zone is through convection from the flue gas to the coil. In the shock zone, both radiative and convective modes of heat transfer are occurring, as the surrounding temperature around the coil (i.e. the flue gas) is higher in this section. This section's function is to evaporate the EDC and superheat it to approximately 20 °C above boiling point. The evaporated EDC then reaches the firebox, where it is further heated until the reaction starts. The product flow is sent through the adiabatic volume section, where the reaction proceeds further, without heat supply, until the temperature falls below cracking temperature. Finally, the product gas is quenched, and the temperature drop prevents the cracking reactions to occur any further.

Process control of cracker operation

Control of the EDC cracker is performed with the outlet temperature of the process fluid from the cracker as the measured (i.e. input) variable. This temperature is monitored to control the conversion in the reactor. The manipulated variable is the fired heat to the reactor, which is regulated based on the outlet temperature. If the cracker is approaching a shut down, with coke building up in the coil pipes, the measured temperature will be lower, and thus more fired heat is required. Development of coke will be further described in this section.

2.4 Literature review - the reaction mechanism of EDC pyrolysis

Thermal cracking of EDC is considered to proceed trough a complex radical chain mechanism [1]. The complex thermal cracking reactions of EDC have been widely studied and improved by various researchers during the past 60 years. These studies include proposed reaction mechanisms and reaction kinetics, which is found in literature [5–8, 16–24].

One of the earliest studies of the reaction mechanism of EDC pyrolysis, conducted by *Barton et al.* [16] during 1940 and 1941, examined the effect of addition of volatile substances on the reaction rate of thermal decomposition of EDC. Barton suggested that the decomposition rate was greatly increased by addition of small amounts of oxygen or chlorine. He also concluded that the decomposition induced by oxygen or chlorine was of the radical chain reaction type, and that the oxygen induced decomposition was inhibited by all aliphatic and alicyclic hydrocarbons. Barton and *Howlett* continued the study [17], and purposed that the decomposition proceeds by a homogeneous, nearly first order overall reaction to give vinyl chloride and hydrogen chloride. They postulated a reaction mechanism which gave the possibility to estimate qualitatively the propylene inhibition. Howlett further examined the reaction mechanism [18] in 1951, and stated that the first-order rate constant was independent of pressure in a certain range. The radical chain-mechanism suggested by Barton and Howlett was modified to account for experimental observations, by *Holbrook et al.* in 1968 [19]. In 1980 new experimental studies were performed by *Ashmore et al.* [20]. They purposed three main propagating steps in the mechanism, and investigated the effect of reaction conditions on the production rates.

Later studies on EDC pyrolysis have given more attention to coke and byproduct formation, as well as the effect of inhibitors and promotors. The kinetic reaction model has also been improved and studied in more detail. A detailed quantitative description of the EDC pyrolysis reactions was presented by *Incavo* [21] in 1996, by using inline gas chromatography. Incavo provided quantitative information about how promotors affected the yield of VCM and EDC, in addition to determining several byproducts. The same year, *Mochida et al.* [25] investigated the formation of cokes in the different stages of a commercial EDC cracking unit.

A kinetic model with more than 200 elementary reactions and more than 40 molecular species and radicals was in 1992 introduced by *Ranzi et al.* [8]. The most extensive and detailed chemical reaction kinetic model is the one developed by *Borsa* [6] in his doctoral thesis from 1999. This reaction mechanism includes as many as 71 molecular species, 64 radicals and 818 elementary reactions. *Choi et al.* [7] proposed a reaction model based on 108 reversible elementary reactions and 47 molecular and radical species in 2001, based on thermochemical kinetic theories. This is the first study where the addition of the promotor carbon tetrachloride (CCl_4) was investigated. Another complex model was developed by *Lee* [23] in 2002, which involves 44 gas phase species and 260 elementary forward and backward reactions. In this study, several important reaction pathways were identified. The pyrolysis mechanism was simplified by *Schirmeister et al.* [5] presented in a study from 2009. The suggested model is based on 31 reactions, 16 molecular species and 8 radicals, which cover the most relevant and important products, intermediates and byproducts.

The reaction classes

Radical reaction mechanisms consist of three main steps: initiation, propagation and termination. These steps can be further categorised in several reaction classes. Division of the classes varies with the complexity of the reaction mechanism. An example of reaction class division is shown in Figure 2.4.

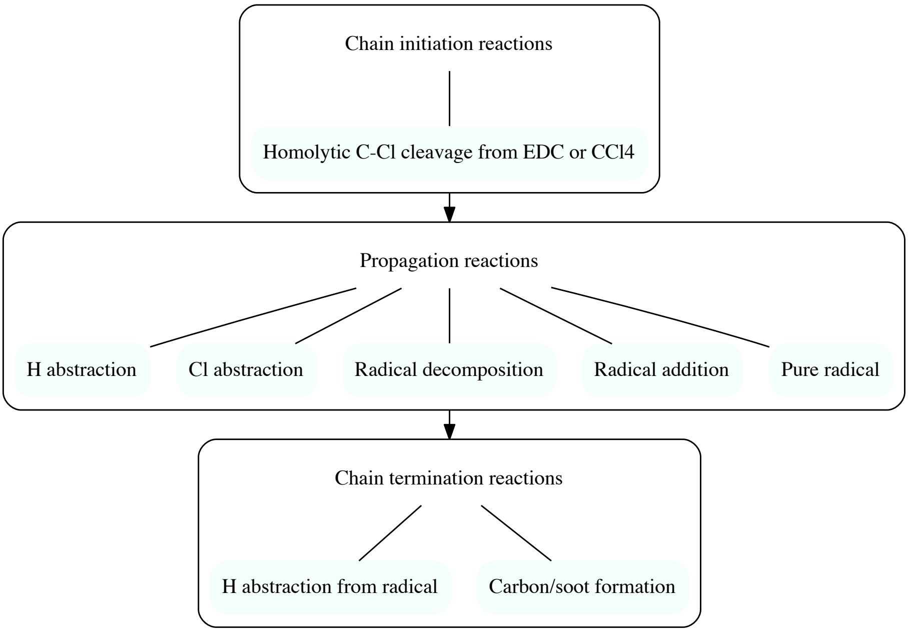

Figure 2.4. Reaction class division of the chain reaction mechanism of EDC pyrolysis.

As the figure indicates, the initiation step of EDC pyrolysis involves *cleavage of carbon-chloride bonds* from molecular species. In addition to cleavage of EDC, this could also involve thermal cleavage of a promotor, in this case CCl_4. These both yield Cl radicals, which starts the propagation reactions.

$$\mathrm{CH_2Cl - CH_2Cl \rightarrow CH_2Cl - CH_2{}^{\bullet} + Cl^{\bullet}} \tag{2.6}$$

$$\mathrm{CCl_4 \rightarrow CCl_3{}^{\bullet} + Cl^{\bullet}} \tag{2.7}$$

The main propagation step is the *abstraction of hydrogen* by Cl radicals [7]. In these reactions, the Cl radical abstracts an hydrogen atom in a chlorinated hydrocarbon, yielding a chlorinated hydrocarbon radical. An example of this the following equation.

$$\mathrm{CH_2Cl-CH_2Cl+Cl^{\bullet}\rightarrow CH_2Cl-CHCl^{\bullet}+HCl} \tag{2.8}$$

The produced radical from equation (2.8) could decompose (*radical decomposition*) to form VCM and a new Cl radical, which is another form of propagation reaction:

$$\mathrm{CH_2Cl-CHCl^{\bullet}\rightarrow CH_2{=}CHCl+Cl^{\bullet}} \tag{2.9}$$

Chain termination and decrease in the total radical concentration can take place when a *H is abstracted from a radical*, yielding two stable species (VCM and HCl).

$$\mathrm{Cl^{\bullet}+CH_3-CHCl^{\bullet}\rightarrow CH_2{=}CHCl+HCl} \tag{2.10}$$

Examples of the other types of reaction classes as well as their reactions can be found in Choi et al [7], Schirmeister et al [5] (elaborated in Chapter 6), and an extensive set of equations can be found in Borsa [6], among others.

Promotors and inhibitors

Addition of promotors increase the reactivity of the system. In the case of a radical reaction mechanism, the promotor's role is to supply radicals which are necessary for the propagation steps of the mechanism. EDC cracking is assumed to be Cl-catalyzed, and thus a Cl supplying species can act as a promotor. CCl_4 is known to be an efficient source of Cl radicals, and hence a suitable promotor [7]. The role of CCl_4 is the same as that of Cl_2 in chlorination models [5]. The reason why these compounds increase the conversion is that the rates and the equilibrium constants for the reactions donating a Cl radical are much greater compared to the reaction where EDC is donating a Cl radical [7]. An inhibitor, on the other hand, could slow or prevent a reaction from occuring, by "stealing" radicals or by creating alternative reaction pathways, which may compete with the desired reaction pathway. An example of such inhibitors could be 1,1-dichloroethane (1,1-EDC).

Studies have shown that impurities on a ppm level can act as promotors or inhibitors [20, 26]. When considering taking advantage of impurities in the form of promotors which increase the conversion (and reduce the fuel gas consumption), it must be taken into account the increased cost such impurities could introduce, as they could also affect byproduct formation. An increase in EDC conversion could be offset by increased maintenance costs related to coke, byproducts and increased frequency of plant shutdowns as a consequence of decoking[2] [26].

Formation of coke and other byproducts

Coke is one of the byproducts of major concern of pyrolysis of EDC [21, 25–27]. It is a carbonaceous material which is formed in the reactor coils from the firebox to the quenching point, and deposits at the coil walls. Several studies conclude that the deposition of coke is not uniformly distributed in the reaction pipes and that it has different composition depending on the location in the plant [5, 6]. Formation of coke causes three forms of principal process inefficiencies [6]. First of all, it decreases the heat transfer coefficient (as it increases the heat resistance because of the low heat conductor properties), leading to the need of a higher heat input to reach the desired temperature inside the reaction coils. Secondly, the coke layer decreases the cross sectional area of the coils, and thus slowly increases the pressure drop throughout the coils. Coke particles formed in the gas phase could also result in problems with downstream operations in the liquid stream such as plugging [6].

Two types of coke are discussed in studies of coke formation; *soft coke* which is transported by the process fluid, and *hard coke* which is the coke layers deposited on the coil walls [5, 6, 25]. A study by Borsa et al. [27] concluded that coke is formed in the gas phase as tar droplets in the high temperature regions of the furnace, and that a second source of coke formation is the section where EDC is evaporated by subsequent condensation. Another study by Borsa et al. [26] found that the only component which strongly correlated with coke formation was chloroprene, in their laboratory quartz tube reactor. This was confirmed by Zychlinski et al [28]. It was also concluded that benzene was not an important coke precursor, and that acetylene only had a small impact [26, 28]. Studies have also discussed whether or not there is a correlation between coke formation and promotors such as CCl_4. It is suggested that the increase in coke formation is due to the increased conversion as a consequence of the promotor, and is thus only *indirectly* linked to the promotor [28].

Low amounts of byproducts (less than 1wt %) as a result of side reactions have been reported in literature [5, 6]. However, these small amounts may still alter the process and cause inefficiencies. As mentioned, they could act as inhibitors or promotors. In addition, gas phase products such as chloroprene and butadiene may cause difficulties in downstream operations e.g. distillation columns [6].

---

[2] Decoking involves burning the coke with air and steam.

CHAPTER 3

METHODOLOGY AND CONCEPTS OF THE PLUG FLOW REACTOR

As the pyrolysis reactions of the 1,2-dichloroethane (EDC) cracking occur in two long, parallel coils, a tubular reactor model, or more specifically a plug flow reactor (PFR) model can be used for modeling and simulation of this system. The purpose of this chapter is to establish the mathematical equations and terms used for modeling of the *steady state* operation of the PFR. Derivations of mass and energy balances will be given in detail, as these provide the basis for the governing equation set used in the thesis. Most of the details here are taken from Haug-Warberg's *Plug Flow Reactor* [29]. Notation and units introduced in this chapter will be used consistently through the thesis.

A PFR model is an idealised, non-diffusive reactor model which is used for practical chemical engineering applications [30]. This type of reactor is a continuous flow tubular reactor, where the fluid going through the reactor is modelled as a series of infinitely thin discs (or *plugs*) with uniform properties [31]. A key assumption is that there are no radial gradients, meaning no mixing along the parallel streamlines with equal velocity. Thus, the fluid is assumed to be perfectly mixed in the radial direction.

3.1 The mass balance

For development of the balance equations of mass and energy, the continuity approach is used, given in the general form as

$$\begin{pmatrix} \text{Rate of} \\ \text{accumulation} \\ \text{of quantity} \end{pmatrix} = - \begin{pmatrix} \text{Net amount of} \\ \text{quantity leaving} \\ \text{boundary} \end{pmatrix} + \begin{pmatrix} \text{Net} \\ \text{generation} \\ \text{of quantity} \end{pmatrix} \tag{3.1}$$

where the boundary in this case is the reactor segment from z to $z + \Delta z$, as illustrated in Figure 3.1.

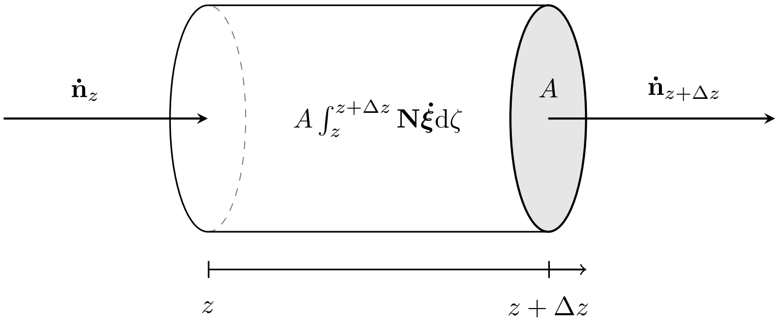

Figure 3.1. Schematic of a plug flow reactor, with relevant variables for the mass balance. $\dot{\boldsymbol{n}}_z$ and $\dot{\mathbf{n}}_{z+\Delta z}$ are the (vectors of) mole flows in and out of reactor segment with length Δz. A is the cross section area of the reactor.

Expressing this mathematically, the general mole balance for the reactor is written according to equation (3.1), formulating the rate of molar accumulation as

$$\left(\frac{\partial \mathbf{n}}{\partial t}\right)_z = \dot{\mathbf{n}}_z - \dot{\mathbf{n}}_{z+\Delta z} + A \int_z^{z+\Delta z} \mathbf{N}\dot{\boldsymbol{\xi}} d\zeta \tag{3.2}$$

where $\dot{\mathbf{n}}_z$ and $\dot{\mathbf{n}}_{z+\Delta z}$ are the vectors of molar flows of the respective species in the system. The integration term represents the *generation* of the respective species in the system, where $\dot{\boldsymbol{\xi}}$ represents the (vector of) independent *reaction rates* (moles per unit time and volume) and $\mathbf{N}$ is the stoichiometry matrix of the reactions and species, which is dimensionless. A is the area of the reactor segment perpendicular to the flow direction, as illustrated i Figure 3.1. Multiplying with A and integrating over the reactor length is equivalent to integrating over the volume of the reactor (segment), which perhaps is a more familiar form of the PFR model. $\mathbf{N}$ and $\dot{\boldsymbol{\xi}}$ are specific for the set of reactions. The reaction rates are usually dependent on temperature according to the Arrhenius equation, and on the concentrations of certain species in the system, depending on the kinetic model. The terms will be further clarified when utilised for the specific kinetic models given in Chapter 6. Further developing equation (3.2), the steady state assumption is used by requiring the partial derivative of $\mathbf{n}$ to be $(\partial \mathbf{n}/\partial t) = 0$, which yields

$$\dot{\mathbf{n}}_{z+\Delta z} - \dot{\mathbf{n}}_z = A \int_z^{z+\Delta z} \mathbf{N}\dot{\boldsymbol{\xi}} d\zeta \tag{3.3}$$

The flow of mass is then factored into a mass term and a composition term, and the conservation of mass principle is introduced as follows

$$\dot{n} = \dot{M}\mathbf{c} \tag{3.4a}$$

$$\dot{M}_{z+\Delta z} - \dot{M}_z = 0 \implies \dot{M}_{z+\Delta z} = \dot{M}_z \triangleq \dot{M} \tag{3.4b}$$

where $\dot{M}$ is the total mass in the system, and the composition (mole) vector $\mathbf{c}$ represents moles per mass of the respective species. Using the definitions from equation (3.4a) and (3.4b) gives:

$$(\dot{M}\mathbf{c})_{z+\Delta_z} - (\dot{M}\mathbf{c})_z = A\int_z^{z+\Delta z} \mathbf{N}\dot{\boldsymbol{\xi}}\mathrm{d}\zeta \tag{3.5}$$

Proceeding through dividing by $\dot{M}$ on both sides gives the expression:

$$\mathbf{c}_{z+\Delta_z} - \mathbf{c}_z = A\int_z^{z+\Delta z} \mathbf{N}\dot{\boldsymbol{\xi}}\dot{M}^{-1}\mathrm{d}\zeta \tag{3.6}$$

Taking the limit and then rearranging by dividing by Δz gives the following expression:

$$\lim_{\Delta z \to 0} \frac{\mathbf{c}_{z+\Delta z} - \mathbf{c}_z}{\Delta z} = A\mathbf{N}\dot{M}^{-1}\dot{\boldsymbol{\xi}} \tag{3.7}$$

The specific reaction rate, $\dot{\xi}$, is substituted by the introduced *specific reaction yield*, $\mathbf{r}$, defined as

$$\mathbf{r} \triangleq \dot{\boldsymbol{\xi}}\dot{M}^{-1} \tag{3.8}$$

where the elements of $\mathbf{r}$ have the unit moles per unit mass and volume. By using this definition, and observing that the left hand side of equation (3.7) is the partial derivative of $\mathbf{c}$ with respect to z, finally gives the steady state mass balance of the plug flow reactor, as given below.

$$\left(\frac{\partial \mathbf{c}}{\partial z}\right)^{(ss)} = A\mathbf{N}\mathbf{r} \tag{3.9}$$

3.2 The energy balance

The derivation of the energy balance begins with the statement which says that energy is a *conserved* quantity. Although it is well known that this is not entirely true (regarding e.g nuclear reactions), as Einstein proved in his mass-energy equivalence equation. However, for this process, the assumption of conservation (and independence) of mass and energy, holds for practical measures.

Performing the energy balance for the *open* flow system illustrated in Figure 3.1, the change in energy, E, is written

$$\left(\frac{\partial E}{\partial t}\right)_{z,\Delta z} = \dot{E}_z - \dot{E}_{z+\Delta z} + \dot{Q} + \dot{W} \tag{3.10}$$

where $\dot{E}_z$[1] and $\dot{E}_{z+\Delta z}$ refers to *transported* energy at the spatial points z and $z + \Delta z$. $\dot{Q}$ and $\dot{W}$ are the transferred heat from the environment to the system and work performed on the system, where system means the segment of the reactor from z to $z + \Delta z$. Energy, $\dot{E}$, has several contributions, as illustrated below

$$E = U + E_p + E_k + \cdots \tag{3.11}$$

where U is *internal* energy, E_p is potential energy and E_k is kinetic energy. Usually, all terms except the internal energy term can be neglected, which is done in this case. Thus, it is assumed that the energy of the system is equal to the internal energy, $E = U$. With this assumption, the energy balance becomes

$$\left(\frac{\partial U}{\partial t}\right)_{z,\Delta z} = \dot{U}_z - \dot{U}_{z+\Delta z} + \dot{Q} + \dot{W} \tag{3.12}$$

where the work term can be divided into a mechanical contribution of shaft work, W_s, and a pressure-volume contribution, $p\dot{V}$:

$$\dot{W} = \dot{W}_s + p\dot{V} \tag{3.13}$$

It is now convenient to introduce the enthalpy relation, as given below:

$$\dot{H} = \dot{U} + p\dot{V} \tag{3.14}$$

---

[1] The notation $\dot{E}$ should not be confused with the time derivative of the mathematical function E.

where $\dot{H}$ is the transported enthalpy, p is the pressure and $\dot{V}$ the volume flow. Combining equation (3.15), (3.13) and (3.14), yields the following expression:

$$\begin{aligned}\left(\frac{\partial U}{\partial t}\right)_{z,\Delta z} &= \dot{U}_z - \dot{U}_{z+\Delta z} + (p\dot{V})_z - (p\dot{V})_{z+\Delta z} + \dot{Q} \\ \implies \left(\frac{\partial U}{\partial t}\right)_{z,\Delta z} &= \dot{H}_z - \dot{H}_{z+\Delta z} + \dot{Q}\end{aligned} \tag{3.15}$$

To find the transferred heat $\dot{Q}$, the heat per surface area perpendicular to the heat transfer, $\dot{q}$, is integrated over the surface area, as given below.

$$\dot{Q} = C \int_{z}^{z+\Delta z} \dot{q} \mathrm{d}\zeta \tag{3.16}$$

Here, C is the circumference of the reactor. When integrating over the reactor length, this is equivalent to integrating over the surface area perpendicular to the heat transfer, as illustrated in Figure 3.2.

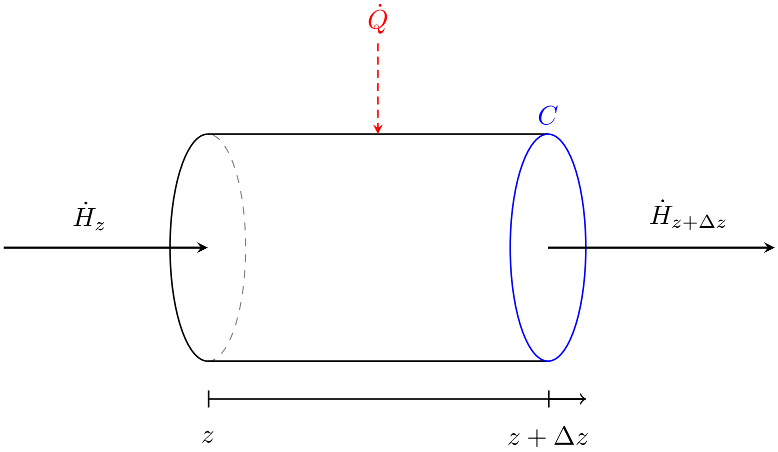

Figure 3.2. Schematic of the heat transfer to the plug flow reactor. $\dot{H}_z$ and $\dot{H}_{z+\Delta z}$ represent the state of (transported) enthalpy in and out of the reactor, respectively. C is the circumference of the reactor.

Combining this expression with equation (3.15) gives

$$\left(\frac{\partial U}{\partial t}\right)_{z,\Delta z} = \dot{H}_z - \dot{H}_{z+\Delta z} + C \int_{z}^{z+\Delta z} \dot{q} \mathrm{d}\zeta \tag{3.17}$$

Finally, the *steady state* solution of this equation is obtained, as $\frac{\partial U}{\partial t} = 0$:

$$(\dot{H}_{z+\Delta z} - \dot{H}_z)^{ss} = C \int_z^{z+\Delta z} \dot{q} \mathrm{d}\zeta \tag{3.18}$$

which is a time-independent steady state form of the energy balance. The specific enthalpy is then introduced[2];

$$\dot{H} = h\dot{M} \tag{3.19}$$

where h is the specific enthalpy, with specific referring to enthalpy per mass. Using the definition from equation (3.19) on the obtained energy balance gives:

$$(h\dot{M})_{z+\Delta z} - (h\dot{M})_z = C \int_z^{z+\Delta z} \dot{q} \mathrm{d}\zeta \tag{3.20}$$

Again, the conservation of mass principle as given in equation (3.4b) is used, and division by $\dot{M}$ on both sides gives the form:

$$h_{z+\Delta z} - h_z = C \int_z^{z+\Delta z} \dot{M}^{-1} \dot{q} \mathrm{d}\zeta \tag{3.21}$$

In similarity with the development of the mass balance, the limit is taken and the equation is rearranged. The result is as follows:

$$\lim_{\Delta z \to 0} \frac{h_{z+\Delta z} - h_z}{\Delta z} = C \dot{q} \dot{M}^{-1} \tag{3.22}$$

For the right hand side of equation (3.22), heat load is substituted according to the definition

$$q \triangleq \frac{\dot{q}}{\dot{m}} \tag{3.23}$$

so that q is the specific heat load per mass and area. Eventually, the final form of the steady state energy balance is achieved, as given below.

$$\left(\frac{\partial h}{\partial z}\right)^{(ss)} = Cq \tag{3.24}$$

The mass and energy balance developed here provide, as mentioned, the basis for the cracker simulation model, together with the momentum balance. The right hand sides of the differential equations will be given by the respective kinetic and heat models, which will be further elaborated.

---

[2] This specific enthalpy relation (or scaling) is an example of an *Euler homogeneous* function.

3.3 General terms associated with sizing of the system

Designing the size of a PFR is dependent on the desired *conversion* of the reactor system. In this study, conversion is defined according to the following equation on a molar basis[3]:

$$x_{\mathrm{EDC}}^{\mathrm{c}} \triangleq \frac{c_{\mathrm{EDC},0} - c_{\mathrm{EDC}}}{c_{\mathrm{EDC},0}} \tag{3.25}$$

The conversion, $x_{\mathrm{EDC}}^{\mathrm{w}}$, is in this case the ratio of the moles of reacted EDC to the number of moles of EDC which is fed to the reactor. In this report, conversion on a mass basis is also considered, which is calculated in a similar manner, as in equation (3.26).

$$x_{\mathrm{EDC}}^{\mathrm{w}} \triangleq \frac{\dot{m}_{\mathrm{EDC},0} - \dot{m}_{\mathrm{EDC}}}{\dot{m}_{\mathrm{EDC},0}} \tag{3.26}$$

Multiple reactions introduce the need of the term *selectivity.* In this thesis, selectivity is defined as the ratio of moles of desired product formed (VCM), to the number of moles of reacted EDC:

$$S \triangleq \frac{c_{\mathrm{VCM}} - c_{\mathrm{VCM},0}}{c_{EDC} - c_{\mathrm{EDC},0}} = \frac{c_{\mathrm{VCM}}}{\Delta c_{\mathrm{EDC}}} \tag{3.27}$$

It is also assumed here that there is initially no VCM in the feed to the reactor. However, in the real reactor there is a small quantity of VCM present in the feed (ppm level), as will be shown later, for the modeling input values. However, this is negligible compared to the quantity of VCM formed in the reactor. Note that through the report, the *weight* basis of conversion will be used, and selectivity is defined on a *molar* basis.

A final term which is connected to the size of the system is the *space time* (or *mean residence time*). The space time is found by dividing the volume of the reactor by the volumetric flow rate entering the reactor, $\dot{V}_0$ [m^3/s]:

$$\tau \triangleq \frac{V}{\dot{V}_0} \tag{3.28}$$

In other words, space time represents the time necessary to process the reactor volume of fluid, with the given entrance conditions ($\dot{V}_0$) [31].

---

[3] This gives the same form as the regular mole basis conversion applied in chemical engineering.

CHAPTER 4

HEAT TRANSFER THEORY

If there exists a spatial temperature difference between media or in a medium, heat transfer (or *thermal energy in transit*) must occur. In the cracker furnace, heat is absorbed by the coil pipe from the flue gas, in the form of *convection* and *radiation*. In addition, *conduction* through the pipe walls also occurs. These modes of heat transfer, as well as their rate laws, will be presented in this chapter. This also includes *gas radiation* from polar gases, e.g. CO_2 and H_2O.

4.1 Convection

Convection refers to the heat transfer process where heat is transferred between a surface and a moving fluid. This heat process has two contributions; *diffusion* (random molecular movement) and *bulk movement* (macroscopic movement of the fluid). For both *natural* and *forced* convection[1], the heat flux equation takes the form [9]:

$$\dot{q}_{\mathrm{conv}} = h(T_{\mathrm{s}} - T_{\infty}) \tag{4.1}$$

This equation is known as *Newon's law of cooling.* $\dot{q}_{\mathrm{conv}}$ is the heat flux (energy per time and area), T_{s} and T_{∞} are the surface temperature and the fluid temperature, respectively. The *convection heat transfer coefficient*, h [$\mathrm{J\,s^{-1}\,K^{-1}\,m^{-2}}$], is discussed in the following section. To find the total heat transfer rate $\dot{Q}_{\mathrm{conv}}$, the heat flux must be multiplied by the *perpendicular* surface area to the heat transfer flux, according to the introduced notation:

---

[1] Natural (free) convection is a result of temperature differences which affect the relative buoyancy of the fluid, leading to bulk motion. In forced convection, the fluid movement is a result of external forces, such as a pump [9].

$$\dot{Q} \triangleq A\dot{q} \tag{4.2}$$

The convection coefficient

The convection coefficient is dependent on conditions in the boundary layer, such as the nature of the fluid motion, fluid thermodynamics, transport properties and the surface geometry[2] [9]. Thus, it is determined by both the fluid properties (flow conditions) and also the surface geometry. The *Nusselt number*, Nu, is a dimensionless parameter which can be used to estimate the convection coefficient, which is defined as follows

$$Nu \triangleq \frac{hL}{k} \tag{4.3}$$

where L is the characteristic length[3], and k $[\mathrm{J\,m^{-1}\,K^{-1}}]$ is the *thermal conductivity* of the fluid. The Nusselt number is the dimensionless temperature at the surface, and thus provides a measure of the convective heat transfer [9]. For a prescribed geometry, the Nusselt number is a function of the *Reynold's number* and the *Prandtl number* [9, 11]:

$$Nu = f(x, Re_L, Pr) \tag{4.4}$$

where x is a spatial variable, which is a point at the surface which is exchanging heat with the surrounding fluid. By integrating over the surface or using average values for the properties of the surface area, the average Nusselt number can be found. Different correlations for the Nusselt number for various surface geometries and different internal and external flow patterns exist in literature [9–11].

The *Reynolds number* is a measure of the ratio of inertial forces to viscous forces[4]. For an internal flow in a pipe, the dimensionless Reynolds number, Re_{D}, can be defined as

$$Re_D \triangleq \frac{vD}{\nu} = \frac{\rho v D}{\mu} \tag{4.5}$$

where ρ is the density of the fluid, v is the fluid velocity, D is the diameter of the pipe, and ν $[\mathrm{m\,s^{-2}}]$ is the *kinematic viscosity*. The Reynolds number can

---

[2] Typical values for the convection coefficient are 2-250 W/m^2,K for gases, and 50-20 000 W/m^2,K for liquids, depending on whether the convection is free or forced (where forced has a higher rate) [9].

[3] E.g for a pipe, the characteristic length is the diameter of the pipe.

[4] Inertial forces are due to the momentum of the fluid, and viscous forces are frictional shear forces [11].

also be expressed through the *dynamic viscosity*, μ [$\mathrm{kg\,s^{-1}\,m^{-1}}$], by using the definition $\nu = \mu/\rho$, as shown in equation (4.5).

The *Prandtl number* is defined as the ratio between momentum (viscous) and thermal diffusivities:

$$Pr \triangleq \frac{C_p\mu}{k} = \frac{\nu}{\alpha_f} \tag{4.6}$$

In this equation, C_p [$\mathrm{J\,K^{-1}\,kg^{-1}}$] is the heat capacity of the fluid, α_f [$\mathrm{m^2/s}$], is the thermal diffusivity of the fluid and k [$\mathrm{J\,s^{-1}\,m^{-1}\,K^{-1}}$] is the *thermal conductivity* of the fluid. The definitions $\alpha = k/\rho C_p$ and $\nu = \mu/\rho$ are used on the right hand side of the equation. The Prandtl number describes the relative ease of momentum and energy transport in flow systems, and involves only physical properties of the fluid [11]. A typical value for the Pr number of gases is $Pr = 0.7$, whereas liquids typically have higher values [11].

4.2 Conduction

Conduction is a heat transfer process occurring in a stationary medium, which may be a solid or a liquid. The heat is transferred within and through the body itself. This heat transfer is a result of interaction between particles (molecular and atomic movement), where the heat is transferred from the more energetic particles to the less energetic particles [9]. In a solid, where the atoms have limited movement, the transfer is due to atomic activity in the form of lattice vibrations. To quantify the conductive heat flux, *Fourier's law* can be applied [9,11]:

$$\dot{q}_{\mathrm{cond}} = -k\frac{dT}{dx} \tag{4.7}$$

Equation (4.7) represents the one-dimensional version of Fourier's law, with a temperature distribution $T(x)$, where x is the spatial variable. $\dot{q}_{\mathrm{cond}}$ is the conductive heat flux, which similarly to the convective heat flux must be multiplied by the perpendicular area to obtain the total heat rate. In this case, the heat flux is proportional to dT/dx, which is the temperature gradient in the x direction. Here, the thermal conductivity, k, is a transport property parameter which is characteristic of the specific material and tells how effectively the material conducts heat[5].

---

[5] Heat insulators have a low conductivity, while materials with high conductivities are better heat conductors and have a lower heat resistance. Typical values for thermal conductivity range from about 0.1 W/m,K for gases and up to approximately 1000 W/m,K for pure metals [11].

Under steady *state conditions*, if the conductivity is assumed to be constant through the medium, the temperature will have a linear profile through the medium:

$$\dot{q}_{\mathrm{cond}} = -k\frac{\Delta T}{L} \tag{4.8}$$

In equation (4.8), L is the thickness of the medium (typically a wall), and ΔT is the temperature difference through the medium.

4.3 Radiation

Radiation is a mode of heat transfer which occurs from all surfaces with a finite (above absolute zero) temperature, in the form of electromagnetic waves [9]. This heat transfer will thus also occur in the absence of an intervening material medium. Both solid surfaces, liquids and gases may emit energy in the form of radiation. The emitted energy is due to changes in the electron configuration in the body's molecules or atoms [9].

When thermal radiation reaches a body, part of the radiation is absorbed by this body as heat, part is reflected back into the surroundings and some of the radiation might be transmitted through the body. The sum of the fractional contributions are equal to 1, according to

$$\alpha + \rho + \tau = 1 \tag{4.9}$$

where α is the *absorptivity* or fraction of heat which is absorbed, ρ is the *reflectivity* or reflection fraction and τ is the fraction of transmitted heat (*transmitivity*) [10]. In process engineering, bodies are usually assumed to be opaque to transmission. In these cases, the τ term is neglected ($\tau = 0$) [10]. A *black body*, or ideal radiator, is per definition absorbing all incoming radiation, hence:

$$\rho_b = \tau_b = 0 \implies \alpha_b = 1 \tag{4.10}$$

where α_b refers to the black body absorptivity. *Kirchoff's law* states that for each wavelength and temperature, the absorptivity has to equal its *emissivity* [10]:

$$\alpha_1 = \varepsilon_1 \tag{4.11}$$

For a black body the emissivity is thus equal to 1. The emissivity is defined as the ratio of the emissive power to that of a black body [10]. Equation (4.11) holds for all black or nonblack surfaces. Emitted radiation from a black body ($\varepsilon = 1$) is expressed through *Stefan Boltzmann's law*:

$$E_b = \sigma {T_s}^4 \tag{4.12}$$

where E_b is the *emissive power* or heat flux of the blackbody [$\mathrm{J\,s^{-1}\,m^{-2}}$], σ is *Stefan Boltzmann's constant* (σ = 5.67*10$^-8$ $\mathrm{W\,m^{-2}\,K^{-4}}$) and T_s is the absolute surface temperature. As the equation indicates, the radiation from a blackbody depends only on the surface temperature. A real surface will emit less radiation at the same temperature, as the emissive power is reduced by the factor ε:

$$E = \varepsilon\sigma {T_s}^4 \tag{4.13}$$

where the emissivity is in the range $0 \leq \varepsilon \leq 1$. This variable is dependent on several factors e.g. the material and the nature of the surface. Substances that have $\varepsilon < 1$, which apply to all real materials, are called *gray bodies.*

4.4 Gas radiation - radiative heat exchange with absorbing media

Up to this point in the introduction of radiation, bodies have been assumed to be *opaque*, which means they are completely transparent to radiation. This does not apply to gas radiation, or stated differently; radiation in absorbing media. Gas radiation is a *volumetric* phenomenon, rather than a surface phenomenon. In combustion, radiation is an important contributor to the heat transfer, due to the high temperatures. Combustion processes produce flue gases with a composition dependent on the fuel used, air-to-fuel ratio, pressure and ambient temperature [32]. Some of the compounds of the flue gas absorb and emit radiation selectively at different discrete wavelengths and temperatures (and hence frequencies)[6] [9]. However, studies have shown it is safe to assume that they do not *scatter* emission significantly, unless e.g. large soot particles are involved [32]. Polar gas molecules, such as CO_2 and H_2O, which are typical combustion flue gases, emit and absorb radiation at a wide range of temperatures [33]. Most monatomic or diatomic gases such as N_2, O_2 and Ar are virtually transparent, and are practically nonradiating [10, 33]. As the radiation properties of the radiative gases (emissivities and absorptivites) varies with the electromagnetic spectrum, different models have been developed to account for this variation [32]. The most important types of models are briefly described in the next sections.

---

[6] Solids and liquids emit radiation over a *continuous* spectrum in contrast to gases.

Band models

As previously mentioned, radiation is not continuous, but concentrated in spectral bands [32]. To account for the dependency of the radiative properties of the electromagnetic spectrum, calculations can be performed dividing the wavelength spectrum into bands with discrete spectral lines, employing different *band models*. These band models, along with better measurements and modelling tools such as the *Monte Carlo* method, have improved the understanding and procedures for dealing with the radiative properties of gases [34]. The most accurate description of the spectral lines is the *line-by-line model*, where each band is divided into thousands of wavelength intervals which all have a value for the absorption coefficient [33]. More simple band models, which require less computational cost, include the *wide band model* and the *Statistical Narrow Band* (SNB) model. In these models, the spectrum is divided into a number of spectral bands (intervals) and different absorption coefficients are estimated for each interval [33].

The gray gas model

In the gray gas model, first proposed by Hottel [35], the absorption coefficient is based on an average value over the whole spectrum, and is thus not a function of wavelength as in the band models [33][7]. It is thus a less accurate, but more manageable method. Because of its simplicity, this model as well as the *weighed sum of gray gases model* (WSGGM), have traditionally been the most used for industrial configurations and computational fluid dynamics (CFD) simulations [33, 36]. The WSGGM is a slightly more complex approach, which postulates that the total emissivity and absorptivity may be represented by the sum of grey gas emissivity factors, which is weighed by a temperature dependent factor [37].

Wang et Al [33] evaluated the gray gas model to correctly predict the relative radiation heat transfer flux distribution, but stated that the model overpredicts the total heat transfer rate quantitatively. Soufiani et al [36] concludes that in the case of significant temperature gradients, the weighted gray gas model representation (and the simple gray gas model) of inaccurate gas absorptivities can lead to important errors.

Analytical calculations with the gray gas model

The gray gas model method was first used to determine the incident radiant heat flux from CO_2 and H_2O on a furnace wall [33]. Assuming equation (4.18) is valid, the gray gas method can be used to estimate the total gas emissivity. The gas emissivity, ε_g, is assumed to be a function of temperature, gas composition,

---

[7] The *gray* term refers to the independency of the absorbtion coefficient of wavelength over the spectral regions, and can be used for surfaces or gases [9].

pressure and characteristic length of the combustion chamber, L [33]. The characteristic length can be approximated by [33]:

$$L = 3.6\frac{V_\mathrm{f}}{A_\mathrm{f}} \tag{4.14}$$

where V_f and A_f is the volume and surface area of the furnace (combustion chamber), respectively, used when the heat exchange is between the combustion gases and the walls of the combustion chamber. The mixture emissivity of the gas, ε_g, containing CO_2, H_2O and other nonradiating gases, can be obtained from Hottel's charts and the equation [33]:

$$\begin{split}\varepsilon_\mathrm{g} = C_{\mathrm{H_2O}}(p, p_{\mathrm{H_2O}}, L)\varepsilon_{\mathrm{H_2O}}(T_\mathrm{g}, p_{\mathrm{H_2O}}, L) + C_{\mathrm{CO_2}}(p, p_{\mathrm{CO_2}}, L)\varepsilon_{\mathrm{CO_2}} - \\ \Delta\varepsilon(T_\mathrm{g}, p_{\mathrm{H_2O}}, L)(T_\mathrm{g}, p_{\mathrm{H_2O}}, p_{\mathrm{CO_2}}, L)\end{split} \tag{4.15}$$

In this equation $C_{\mathrm{H_2O}}$ and $C_{\mathrm{CO_2}}$ are the pressure correction factors which are used if the total pressure, p, deviates from 1atm. $p_{\mathrm{H_2O}}$, and $p_{\mathrm{CO_2}}$ are the partial pressures of CO_2 and H_2O, respectively. $\Delta\varepsilon$ is the mixture correction factor, which accounts for the spectrum overlap of H_2O and CO_2. The same procedure is also used to find the gas absorption coefficient given as

$$\alpha_g = \alpha_{H_2O} + \alpha_{CO_2} - \Delta\alpha \tag{4.16}$$

where $\Delta\alpha_\mathrm{g}$ is the correction factor, similar to the correction factor for the gas emissivity. For equation (4.16), the absorptivities of H_2O and CO_2 ($\alpha_{\mathrm{H_2O}}$ and $\alpha_{\mathrm{CO_2}}$) can also be found from the charts, according to the equations:

$$\alpha_{\mathrm{H_2O}} = C_{\mathrm{H_2O}}\left(\frac{T_\mathrm{g}}{T_\mathrm{s}}\right)^{0.45}\varepsilon_{\mathrm{H_2O}}\left(T_\mathrm{s}, p_{\mathrm{H_2O}}L\frac{T_\mathrm{s}}{T_\mathrm{g}}\right) \tag{4.17a}$$

$$\alpha_{\mathrm{CO_2}} = C_{\mathrm{CO_2}}\left(\frac{T_\mathrm{g}}{T_\mathrm{s}}\right)^{0.65}\varepsilon_{\mathrm{CO_2}}\left(T_\mathrm{s}, p_{\mathrm{CO_2}}L\frac{T_\mathrm{s}}{T_\mathrm{g}}\right) \tag{4.17b}$$

$$\Delta\alpha = \Delta\varepsilon\left(T_\mathrm{s}, p_{\mathrm{H_2O}}, p_{\mathrm{CO_2}}, T_\mathrm{s}\frac{L}{T_\mathrm{g}}\right) \tag{4.17c}$$

The emissive radiation from the radiating gases, E_g, can then be calculated in a similar manner as surface radiation through the equation:

$$E_\mathrm{g} = \varepsilon_\mathrm{g}\sigma {T_\mathrm{g}}^4 \tag{4.18}$$

In the this case, T_g is the gas temperature and ε_g is the gas emissivity. The *net rate* of heat exchange between a black surface at $T = T_\mathrm{s}$ and a gas at $T = T_\mathrm{g}$ is [9] can be expressed as follows

$$q_{\mathrm{net}} = A_{\mathrm{s}} \sigma \left(\varepsilon_{\mathrm{g}} T_{\mathrm{g}}^4 - \alpha_{\mathrm{g}} T_{\mathrm{s}}^4 \right) \tag{4.19}$$

where α_g is the absorptivity of the gas mixture to the incident radiation from the blackbody surface, which has a temperature of T_s.

CHAPTER 5

MODEL DEVELOPMENT

In this chapter the framework and general equations of the cracker model are described, in addition to scaling of the model, the thermodynamic state equations and implementation of the model in PYTHON. Details of the kinetic model and the heat transfer model are given in Chapter 6 and 7.

5.1 Model areas, framework program and notation

The simulation model covers three main areas, which are partly discussed in the previous chapters;

- **Reaction kinetics** - Reaction rate expressions, dependent on reactant concentrations and exponentially dependent on temperature according to the Arrhenius equation (equation(6.4)).
- **Transport phenomena** - Based on conservation of mass, energy and momentum. Heat transfer rates are dependent on dimensionless parameters such as the Reynolds number and the Prandtl number.
- **Thermodynamics** - Thermodynamic state equations are based on the ideal gas law and heat capacities are dependent on temperature.

The kinetic model, heat transfer model and the thermodynamics have their respective models and model equations, whereas the general mass and energy balance were developed in Chapter 3. As the kinetics are dependent on the process temperature, coupling of the heat transfer model and the kinetic model is necessary.

The PYTHON program

PYTHON is used as the programming language for the reactor model, which is based on a program developed by Associate Professor Tore Haug-Warberg [29]. This PYTHON program is used as a framework for implementation of kinetic models and a developed heat transfer model. Parts of the framework program are also modified and extended for this study. This applies to the thermodynamics, and also the numerical scheme is expanded to tackle the stiff equation system which is introduced, especially by the kinetic model. The framework model is developed in a general manner, to make implementation of additional kinetic and heat transfer models is possible. It is also possible to implement several models for both heat transfer and kinetics, and switch between these for different simulation cases.

Notation of variables

As a reminder, boldface text for variables or parameters denotes a *vector* or a *matrix*. Also, a few definitions from the previous chapters are given here, in addition to a fourth definition of the specific volume, v:

$$
\begin{aligned}
\dot{n} &\triangleq c\dot{M} \\
\dot{q} &\triangleq q\dot{M} \\
\dot{H} &\triangleq h\dot{M} \\
\dot{V} &\triangleq v\dot{M}
\end{aligned}
$$

In these equations, the capitalized versions of the variables denote the *extensive* variables, depending on the size of the system. The lower case variables are the *specific* quantities, which are defined per mass. This notation will be used consistently throughout the thesis. $\dot{M}$ is the total mass of the system, q is the specific heat (per unit area and mass), h is the specific enthalpy per mass and c is given as moles per unit mass.

5.2 The governing equations

The three governing equations of the model are the three differential equations based on the mass, energy and momentum balances. Development of the mass and energy balance were given in Chapter 3. The model is based on the steady state operation of the reactor, hence the "*ss*" exponent. The assumption of steady state means that the model is not applicable for simulating the dynamic start up (or shut down period) of the process. According to the steady state assumption, thermodynamic properties will vary over the axial length, but remain unchanged at any given axial *point* in the reactor for a given set of initial conditions and parameters. The model is one-dimensional, which mean radial gradients are not included for the state properties in the reactor.

Mass balance

The mass balance is represented by a the previously introduced steady state balance equation:

$$\left(\frac{\partial \mathbf{c}}{\partial z}\right)^{(ss)} = A\mathbf{N}\mathbf{r} \tag{5.2}$$

where $\mathbf{N}$ is the stoichiometry matrix and $\mathbf{r}$ is the specific reaction yield vector (moles per volume and mass). A is the reactor pipe cross section area. Integrating this expression over the reactor length is equivalent to integrating over the volume of the reactor. However, it is convenient to scale the equations to be integrated from $z = 0$ to $z = 1$. This scaling is covered in the next section.

A kinetic model for the reaction rates and the stoichiometry matrix $\mathbf{N}$ is required in order to solve the mass balance equation. The kinetic model is discussed in Chapter 6.

Energy balance

Derivation of the energy balance involves neglecting kinetic and potential energy and friction. As a result, only the internal energy is considered, as shown in Chapter 3. The simplifications lead to an energy balance given as

$$\left(\frac{\partial h}{\partial z}\right)^{(ss)} = Cq \tag{5.3}$$

where h is the specific enthalpy, C is the circumference of the PFR (when integrated over z this becomes the area perpendicular to the heat transfer). To solve the energy balance, a model for the overall heat transfer q (energy per mass), is developed. This model is described in detail in Chapter 7.

Momentum balance

The final governing equation represents the momentum balance. This is needed to obtain the pressure distribution through the reactor. In this model, the momentum balance is replaced by a constant (in this case *linear*) pressure drop through the reactor according to:

$$\left(\frac{\partial p}{\partial z}\right)^{(ss)} = \Delta p \tag{5.4}$$

In this case, the pressure gradient (∇p) have reduced to the difference, Δp, as a linear pressure drop was assumed. The difference in pressure could be to 0 or given a negative value to model a pressure drop from the inlet to the outlet of the reactor. For the firebox section, the pressure drop was set to 3 bar, and 1 bar for the adiabatic volume. Here it is assumed that the pressure drop in the two first sections of the EDC cracker, the convection section and the shock section is 1.5 bar. Overall this gives a pressure drop of 5.5 bar, which is a typical pressure drop value reported from INEOS [15], from the inlet to the cracker to the quenching point, which is the end of the adiabatic volume. In literature, more complex relations for pressure drop are given [7]. Some models also take into account the higher pressure drop at the bending zone (see e.g Choi et al. [7]).

5.3 Integration of governing equations

For simulations of the industrial cracker, the governing equations must be integrated over the reactor volume of the firebox section and the adiabatic section. The matrix form of the model is given as [29]

$$\overset{\mathbf{J}(\mathbf{x})}{\begin{pmatrix} \left(\frac{\partial h}{\partial T}\right)_{v,\mathbf{c}} & \left(\frac{\partial h}{\partial v}\right)_{T,\mathbf{c}} & \left(\frac{\partial h}{\partial \mathbf{c}}\right)_{T,v} \\ \left(\frac{\partial p}{\partial T}\right)_{v,\mathbf{c}} & \left(\frac{\partial p}{\partial v}\right)_{T,\mathbf{c}} & \left(\frac{\partial p}{\partial \mathbf{c}}\right)_{T,v} \\ 0 & 0 & \mathbf{I} \end{pmatrix}} \overset{\nabla\,\mathbf{x}}{\begin{pmatrix} \frac{\mathrm{d}T}{\mathrm{d}z} \\ \frac{\mathrm{d}v}{\mathrm{d}z} \\ \frac{\mathrm{d}\mathbf{c}}{\mathrm{d}z} \end{pmatrix}} = \overset{f(z,\mathbf{x})}{\begin{pmatrix} Cq \\ \Delta p \\ A\mathbf{N}\mathbf{r} \end{pmatrix}} \tag{5.5}$$

$J(\mathbf{x})$, is the *Jacobian matrix*[1] which is defined as

$$\mathbf{J} = \left(\frac{\partial \mathbf{y}}{\partial \mathbf{x}^T}\right) \tag{5.6}$$

$\mathbf{I}$ is the *identity matrix*, which is an $n \times n$ matrix (n is the number of species), with ones on the diagonal and zeros elsewhere. Multiplication with $\mathrm{d}\mathbf{c}/\mathrm{d}z$ yields all the differential quotients of the respective species in the kinetic model (one for each). The equation system thus consists of $n + 2$ differential equations, where n is the number of species in the kinetic model and the two last differential equations are represented through p and h.

The left hand side of equation (5.5) is equivalent to the *differential quotients*[2]. $\mathrm{d}h/\mathrm{d}z$, $\mathrm{d}p/\mathrm{d}z$ and $\mathrm{d}\mathbf{c}/\mathrm{d}z$. These differential quotients are estimated through

---

[1] The Jacobian matrix yields the best linear approximation of a function f near x.

[2] $\left(\frac{\mathrm{d}h}{\mathrm{d}z}\right) = \left(\frac{\partial h}{\partial T}\right)_{v,c_1,c_2,..}\left(\frac{\mathrm{d}T}{\mathrm{d}z}\right) + \left(\frac{\partial h}{\partial v}\right)_{T,c_1,c_2,..}\left(\frac{\mathrm{d}v}{\mathrm{d}z}\right) + \left(\frac{\partial h}{\partial c_1}\right)_{T,v,c_2,c_3,..}\left(\frac{\mathrm{d}c_1}{\mathrm{d}z}\right) + \cdots$

the respective models for heat, kinetics and pressure drop, which are represented by the right hand side of the equation. As the equation indicates, the Jacobian matrix is independent of spatial position z (and of the transport properties), while the models for h, p and $\mathbf{c}$ ($f(z, \mathbf{x})$) are dependent on both spatial coordinate and the thermodynamic state variables.

To calculate the temperature and mole profiles through the reactor, in addition to other model variables of interest, the equations are integrated according to the following anti-derivative of the reactor model:

$$\mathbf{x}(z) = \mathbf{x}_0 + \int_0^z \mathbf{J}^{-1}\mathbf{f}(z, \mathbf{x})\mathrm{d}z \tag{5.7}$$

This equation can be solved using various ordinary differential equation (ODE) solvers, with different complexity and benefits. The solution using such numerical integrator schemes is covered in more detail in section 5.4.

Scaling of the model to industrial size

In order to have consistency between the model and the industrial process for simulations of the cracker, the scaling of the model must be according to the industrial (*real*) dimensions. The model will be based on one of the three crackers at INEOS' Rafnes site (the three crackers are equal in size). There are two pipes in parallel in each cracker. These two will be modeled as one pipe, whereas the two respective volumes are added. This means that the mass rate will be based on the total mass input to the two pipes. In the model, the system is based on a mass flow of 1.0 $\mathrm{kg\,s^{-1}}$ instead of the 15 $\mathrm{kg\,s^{-1}}$ which is the real mass flow entering the two cracker coils.

Scaling of the kinetic model lays in the transformation from integrating over the volume, V to integrating over the dimensionless reactor coordinate z. For the heat transfer equations, the transformation is from integrating over surface area A to integrating over z. A conceptual illustration of the reactor with thermodynamic state variables and reactor coordinate, z, is found in Figure 5.1.

Integrating over a dimensionless interval from z to Δz, requires the equations to be multiplied by the real length L, as given below in equation (5.8) and (5.9). Here, the balances for the coil segment in Figure 5.1 are shown, illustrating the scaled forms which are implemented in the PFR program.

$$c_{z+\Delta z} - c_z = AL \int_z^{z+\Delta z} \mathbf{N}\mathbf{r}\mathrm{d}z \tag{5.8}$$

$$h_{z+\Delta z} - h_z = CL \int_z^{z+\Delta z} q\mathrm{d}z \tag{5.9}$$

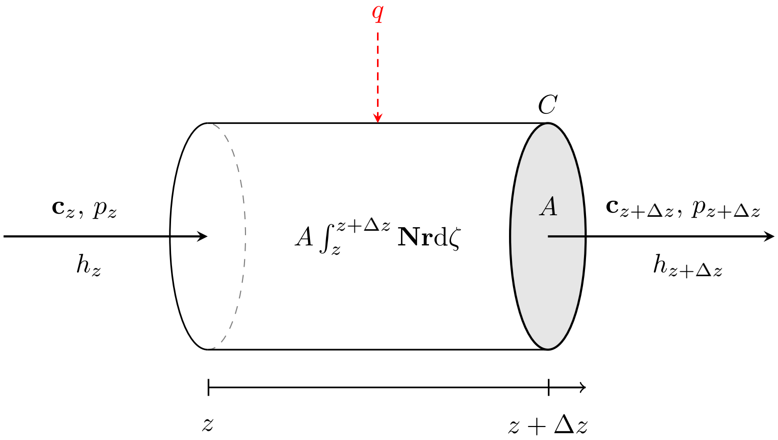

Figure 5.1. Schematic of a plug flow reactor, with state variables h, p, $\mathbf{c}$ (vector containing moles per kilogram for all species), in and out of a reaction segment with the dimensionless length Δz. q represents the heat transferred to the reactor segment, per mass and area. A is the cross section area of the coil (reactor) and C is the circumference.

Again, note that q and $\mathbf{r}$ are *per mass.*

The respective sections modeled as PFRs in series

The firebox section and the adiabatic section are integrated in two different operations, as the dimensions and models differ for these two cases. The two models are identical with respect to the kinetics, but the heat transfer models differ. For the adiabatic volume, the heat transfer model simply reduces to $q = 0$, while the firebox section has a more complex model (see Chapter 7).

The firebox zone is scaled according to the dimensionless reactor coordinate in the range $0 \le z < 1$ and the adiabatic volume is scaled in the range $1 \le z \le 1.5$. At the point $z = 1$, the heat model is switched to adiabatic conditions, as in equation (5.10).

$$q(z) = \begin{cases} q_{\mathrm{rad}} + q_{\mathrm{conv_f}}, & \text{if } 0 \le z < 1. \\ 0, & \text{if } 1 \le z \le 1.5 \end{cases} \tag{5.10}$$

The two terms of the heat model of the firebox section, q_{rad} and $q_{\mathrm{conv_f}}$ are radiative and convective heat transfer from the flue gas in the furnace to the reaction coils. The f subscript denotes the external convection, and not the internal convection in the reaction coils. These terms are further discussed in the description of the heat transfer model, in Chapter 7.

5.4 The simulation step by step - numerical solution procedure

Running a simulation case for the cracker model involves initialisation of primary state variables, execution of the PYTHON program, with following integration through the reactor with corresponding state updates for each step taken during the integration. A block diagram which covers the different steps of the simulation model is illustrated in Figure 5.2.

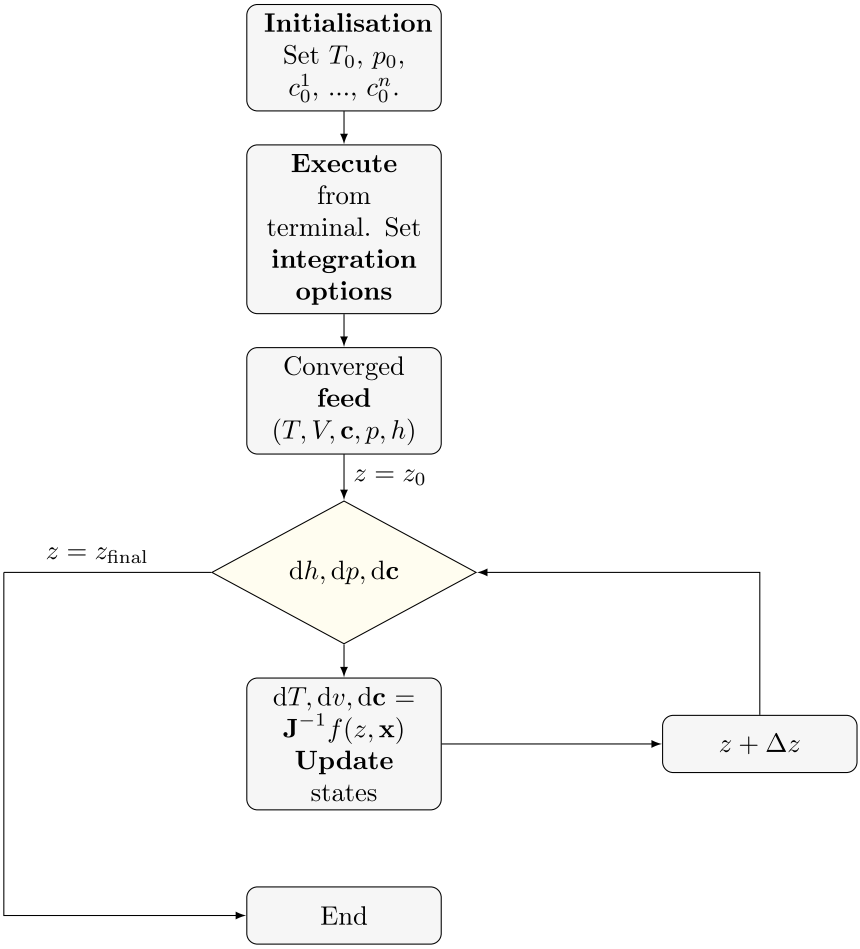

Figure 5.2. Simulation block diagram for the cracker model (PFR model).

As the figure indicates, before a simulation is executed, the *initial values* of the state variables T, p and $\mathbf{c}$ of the feed stream are specified. This is done in the main script, `vcm_reactor.py`. Also, the kinetic and heat transfer model must be chosen, as different models are implemented. For the kinetic model, the choice is between the global reaction model and the extended kinetic model, which is described in the next chapter. The heat transfer model is chosen to be the developed heat transfer model, as described in Chapter 7. However, it is also possible to simulate with more simple heat model cases, e.g. constant heat transfer rate.

Options when executing the simulation

Execution of the simulation is done manually through the terminal, where several options can be specified. These are listed in Table 5.1. As seen in the Table 5.1, the differential equations are integrated with a chosen numerical integrator. *Euler*'s method, as well as *Runge Kutta* second and fourth order were already implemented in the framework PFR model. Two additional integrators were added to the program. The integrators, and explicit/implicit update schemes are more carefully described in section 5.4. In the Python program, the parameter `nz` refers to the number of steps which is taken by the numerical integrator during the integration[5], which must be an integer. Each step interval will be of the dimensionless length

Table 5.1. The options to be specified when running the program from the terminal and the possible choices.

Parameter/ Method	Description	Options
Integrator	Numerical integrator	Euler, RK2, RK4, `SciPy` [38]
Update	Explicit or implicit update	Implicit, explicit
`Nz`	Number of steps	Integer[3]
`Maxiter`	Maximum number of iterations	Integer[4]
Plots	Generation of plots	True, False

$$dz = \frac{z_{\text{final}} - z_0}{nz} \tag{5.11}$$

for the integrators, where z_{final} and z_0 are the initial and final value of z, respectively. The parameter `maxiter` represents the integer of the maximum allowed iterations spent on the thermodynamic state calulations. If this parameter is ascribed a negative value, the program interprets this as an explicit update scheme. In this case, exactly the absolute value of `maxiter` is the number of iterations taken, independent on the residual norm and whether or not full

---

[3] The step size is the integration length divided by the number of steps. Thus, a high values means smaller step length.

[4] Giving a negative value as input here means an explicit update.

[5] For the `SciPy` integrators, the value of `nz` represents the number of data points to be written out at the end of the integration.

convergence is reached. Finally, the *Plot* option gives the possibility to generate and display plots of the chosen state variables[6], which are stored during integration through the reactor.

Newton-Raphson iterations for converged feed stream

The thermodynamic state equations are explicit in the free variables T, v, $\mathbf{c}$, and not pressure. Therefore, the relation

$$p(v) = p_0 \tag{5.12}$$

must be solved to find the volume giving the specified pressure. This is achieved using a *Newton-Raphson* iteration scheme until the feed stream is converged. The convergence criterion is set in the program to be $1.0 \cdot 10^{-8}$, so that convergence is reached when the residual is equal to or lower than this value. The returned free variables T, v and $\mathbf{c}$ are then used to update the other thermodynamic state variables in the model, as well as other defined variables in the model[7].

Integration through reactor

After the simulation is executed and the feed stream is converged, the next step is to start the integration of the governing equations throughout the reactor, from $z = z_0$ to $z = z_{\text{final}}$. How this is performed is dependent on the numerical method chosen (see section 5.4).

Based on the implemented heat transfer model and the kinetic model, which are implemented as so called `lambda` functions[8], the heat transfer rate and the reaction rates are calculated. The heat transfer rate and the reaction rates are functions of the thermodynamic state variables. The first values to be passed to the heat and kinetic models are the values from the converged feed. The heat model yields the heat transfer rate and the kinetic model yields the rate of generation or consumption of moles of the different species in the model. These values gives the changes in h and $\mathbf{c}$, while the pressure drop is given from (5.4).

State updates after model calculation of h, p and $\mathbf{c}$

Update of the state variables T, v and $\mathbf{c}$ is the next step after the respective (coupled) models have estimated the change in h, p and $\mathbf{c}$. This is done by using

---

[6] The plot options must be set in the script *vcm_reactor.py*, but whether or not these should be generated and displayed can be determined in the execution of the script.

[7] State variables are e.g. enthalpy, entropy and chemical potential.

[8] A `lambda` function in PYTHON creates a function definition which is assigned to a variable in the *local* namespace, using the reserved word `lambda`.

a thermodynamic equation solver, the function `hpn_vs_tvn_solver()`, which is part of the framework program. The function iterates on T, v and $\mathbf{c}$ to meet the given specification of h, p and $\mathbf{c}$ (constraints), according to equation (5.5). After convergence, or a predetermined number of iterations are performed, the values of T, v and $\mathbf{c}$ are passed to the *thermodynamics module* in the script `Thermodynamics.py`, for calculation of all thermodynamic states defined in this module. Hence, all thermodynamic states are thus updated according to the developed models. The obtained updated thermodynamic states are then passed to the heat model and kinetic model, for new model estimations, and another loop in Figure 5.2 is started. This loop is continued until the final step is taken, when z reaches z_{final}.

Unphysical values during integration

The thermodynamic script is set up to only proceed with the updates if the system is physical. If for instance the kinetic model gives negative mole rates, due to a negative rate which is larger than the last mole state for a certain species, the program proceeds without updating the thermodynamic states. The same applies to negative pressures or volumes. After this point, the models returns the same rates throughout the integration, as the models receive the same thermodynamic state variable inputs for each step. These results are thus not thermodynamically valid (not physical), hence this is an undesired outcome. Unphysical rates could be due to numerical issues or errors in the implemented heat and kinetic models. Such unphysical values were observed in this work. Different procedures which were tested to tackle these unphysical values and the stiffness of the system are described in Chapter 6.

Numeric integrators

The choice of numerical integrator depends on the stiffness of the differential equation set and also computation time considerations and required data accuracy. J. D. Lambert defined *stiffness* as follows [39]:

> “If a numerical method with a finite region of absolute stability, applied to a system with any initial conditions, is forced to use in a certain interval of integration a steplength which is excessively small in relation to the smoothness of the exact solution in that interval, then the system is said to be stiff in that interval.”

Thus, if the differential equations in the set have sufficiently different time scales, the system is stiff. A typical example in chemical engineering is reactions mechanisms with fast and slow reaction rates, especially the ones involving radicals. This case will be further explored in the next chapter, when the kinetics of the model are discussed.

For a simple, non-stiff equation set, an explicit *Euler* integrator might be sufficient. However, for most cases in this thesis, more advanced numerical integrators are required. The *Runge Kutta methods* belong to a family of explicit and implicit integration methods, developed around 1900 by C. Runge and M.W. Kutta [40]. This method uses an intermediate step at the midpoint of the step interval, to minimize lower order error terms [40]. In the PYTHON program, both the second order and fourth order Runge-Kutta methods are implemented as part of the framework program. The Runge Kutta method of fourth order pose a much higher accuracy than the classical Euler method [41]. However, an explicit Euler method might in some cases be sufficient, and is also less time consuming due to its simple form and the fact that no intermediate steps are taken.

Implementation of additional integrators for stiff systems

In the present work, two additional integrators were added to the program, due to the stiffness of the kinetic model differential equations. These two are both from PYTHON's `SciPy`[9] package built on the `Numpy` extension [38]. As opposed to the Euler and Runge Kutta methods, these implemented integrators from `Scipy` have *adaptive step length*, meaning the integrators are adapting the length of the step to the differentials during the integration.

The first integrator implemented from `Scipy` is `odeint` (which is part of `Scipy`'s `integrate`). This integrator can in general be used for integration of ordinary differential equations. Required input to the solver is a function for the differential equations to be solved, initial values and the range of data points to be returned from the solver. In addition, several parameters can be set, e.g. maximum allowed step size, critical points of integration, to mention a couple of the possible choices. Is this integrator detects a stiff system, it utilises a *backward differentiation formula* (BDF) method. BDF methods approximate the derivatives of the given function using information from already computed derivatives, hence the backwards term [42].

A second integrator was added, `ode` [38], which is also from `SciPy` (which is part of `Scipy`'s `integrate`). This integrator provides a generic interface class for different numeric integrators, which are selected through the *set integrator* method. In this thesis, the integrator `vode` is used, where "vode" stands for Real-valued Variable Ordinary Differential Equation solver. The `ode` integrator also has the possibility to set the type of integrator method. The previously mentioned backwards differential method is chosen, as the problem is stiff.

---

[9] For `Scipy` documentation, see `http://www.scipy.org/`.

Implicit versus explicit updates

Implicit approaches for numerical integration calculate the state of the system at a later time from the current time state, whereas *explicit* approaches use equations involving both the current state and the later state [43]. Implicit methods normally perform higher than the explicit methods, especially when it comes to stiff systems of differential equations. It is worth noting that in theory also the explicit methods could solve stiff differential systems if the integration step was set sufficiently small. However, using extremely small steps is time consuming, and the implicit methods are in such cases usually preferable. To sum this up, there is a trade-off between the time consumption and performance of the integrator, and the choice of integrator is thus dependent on the specific equation system.

Verification of numerical integrators

To verify that the implemented integrators have the desired behavior, they were tested for a set of differential equations where the analytical solution is known. The following set of (two) differential equations was tested.

$$\begin{pmatrix} \mathrm{d}x/\mathrm{d}t \\ \mathrm{d}y/\mathrm{d}t \end{pmatrix} = \begin{pmatrix} 0 & 1 \\ \text{-c} & 0 \end{pmatrix} \begin{pmatrix} x \\ y \end{pmatrix} \tag{5.13}$$

Here, the value of c was set to 1.0, and the initial conditions were $x_0 = 0$ and $y_0 = 0$, respectively. The integrators behaved as desired, proving negligible deviations from the analytical solution. This does not necessarily mean that they are able to tackle all sorts of differential equations, but give an indication that the integrators are correctly implemented and works as desired for this case. Details of the testing and plots are found in Appendix F.

5.5 Input values for simulation

For the simulations with the PFR model in PYTHON, the initial values for the mass composition of the feed are based on average cracker feed values from INEOS from the last 12 months [15]. This set of initial values will be referred to as the *nominal case* in the rest of the thesis. The nominal weight fractions in the feed are listed in Table 5.2[10].

As the table with initial composition shows, there are several species present in the feed stream in addition to EDC. These species are a result of upstream operations and recycling of distilled products, where 100% separation is not achieved. These are the input data to the firebox section, which gives the

---

[10] Dichloroethylene includes 1,1-dichloroethylene and 1,2-cis/trans-dichloroethylene, according to Schirmeister et al. [5].

Table 5.2. The nominal feed composition, based on weight fractions from plant data from INEOS.

Compound	Concentration [wt. ppm]
CCl_4	146
1,1-dichloroethane	476
Trichloroethane	205
Dichloroethylene	14
Benzen	982
Ethyl chloride	3
Trichloromethane	163
Chloropren	15
Trichloroethylene	2432
VCM	29

specification for the feed stream to this section. For integration through the adiabatic volume section, the initial conditions will be the final values after integrating through the firebox section.

The initial values of total mass flow, temperature and pressure are given in Table 5.3.

Table 5.3. Input values for simulation with PYTHON program.

State variable	Symbol	Initial value	Unit
Temperature	T_0	521	K
Total mass flow rate[11]	$\dot{m}$	15.4	$\mathrm{kg\,s^{-1}}$
Pressure	p_0	23.5	bar

5.6 Thermodynamic state model

The equations of state for the process gas is based on the ideal gas model, which is assumed to be sufficient for this model. As the governing equations are integrated through the reactor length, the thermodynamic states must be updated, according to the ideal gas law given as

$$p^{ig} = \frac{\sum_i c_i RT}{v} \tag{5.14}$$

where v is the specific volume per mass, c_i is given as mole per mass, R is the ideal gas constant and T is the temperature. For numerical stability reasons, the units of the different state variables in the thermodynamic code (part of the framework model) are as shown in Table 5.4.

Table 5.4. The units of the thermodynamic state variables.

State variable	Symbol	Unit
Temperature	T	10^3 K
Volume (per mass)	v	$\mathrm{dm^3\,kg^{-1}}$
Mole number (per mass)	c	$\mathrm{mol\,kg^{-1}}$
Energy (per mass)	q, h	10^5 $\mathrm{J\,kg^{-1}}$

To find the enthalpy of each species in the ideal gas mixture, at other values of temperature and pressure than the tabulated standard values, equation (5.15) is used. This equation is developed from the total differential equation of enthalpy, which gives the result that ideal gas enthalpy is independent on pressure. Here, the equation is given on the specific form:

$$h^{ig} = \sum_i c_i \left(h_i^0(T_r) + \int_{T_r}^{T} C_p(T) dT \right) \tag{5.15}$$

T_r is the reference temperature (298.15 K) and T is the state temperature. As the enthalpy equation suggests, the heat capacities are functions of the temperature. To find the value of the heat capacities of the species in the model for different state temperatures, the DIPPR model for ideal gas was used [44][12]. The temperature dependent heat capacities follows equation (5.16).

$$C_\mathrm{p}^\mathrm{ig} = c_1 + c_2 \left(\frac{\frac{c_3}{T}}{\sinh\left(\frac{c_3}{T}\right)} \right)^2 + c_4 \left(\frac{\frac{c_5}{T}}{\cosh\left(\frac{c_5}{T}\right)} \right)^2 \tag{5.16}$$

In the equation, c_1 to c_5 are the DIPPR coefficients from the DIPPR database. These values are found in Appendix A.

---

[12] See `http://dippr.byu.edu/students/chemsearch.asp`.

Chapter 6

The kinetic model

The kinetic models include a reaction mechanism with corresponding kinetic parameters, which are implemented in the framework plug flow reactor (PFR) model, in addition to the coupled heat transfer model. Two kinetic models are implemented. The first is a global reaction model and the second is a more extensive model, which includes different byproducts as well as one promotor and one inhibitor. In this chapter, the reaction mechanisms and the implementation of these are presented.

6.1 Implementation of kinetic model

Given a system of m species and n reactions, the general form of the implementation of the kinetic model is elaborated. First, attention is given to the mass (mole) balance, as given in its general form in Chapter 5.

$$\left(\frac{\partial \mathbf{c}}{\partial z}\right)^{(ss)} = A\mathbf{N}\mathbf{r} = A\mathbf{N}\mathbf{r}(T, \mathbf{c}^{\mathrm{vol}}) \tag{6.1}$$

In this equation, $\mathbf{c}$ [$\mathrm{mol\,kg^{-1}}$] is the mole vector (per mass) of the m species and $\mathbf{r}$ [$\mathrm{mol\,kg^{-1}\,m^{-3}}$] is the vector of *specific reaction yield* (as defined in Chapter 3), and $\mathbf{N}$ is the reaction stoichiometry matrix. As the equation indicates, the reaction yields (or essentially rates) are dependent on the process state temperature and the concentration vector $\mathbf{c^{vol}}$ [$\mathrm{mol\,m^{-3}}$]. The *vol* superscript denotes the *volume* concentration, not to confuse it with the mole per mass vector, $\boldsymbol{c}$, as defined in this thesis.

The general rate laws for a reaction mechanism with n *elementary* reactions and m species A, B,...,m are dependent on the order of the elementary reaction. The general rate law for an elementary reaction i of first order is as follows

$$\dot{\xi}_i = k_i(T)c_r^{vol} \tag{6.2}$$

where $k_{\mathrm{i}}(T)$ is the temperature dependent rate constant and c_r^{vol} is the concentration of the reactant. Recall that $\dot{\xi}$ was defined as $\dot{\xi} = r\dot{M}$. For an elementary reaction of second order, the reaction rate of reaction i is written

$$\dot{\xi}_i = k_i(T)c_{r1}^{\mathrm{vol}}c_{r2}^{\mathrm{vol}} \tag{6.3}$$

where c_{r1}^{vol} and c_{r2}^{vol} are the concentrations of the two reactants of the reaction. The *Arrhenius equation* gives the temperature dependence of the specific reaction rate for reaction i [31].

$$k_i = A_i \exp^{-E_a/RT} \tag{6.4}$$

A_i is the *frequency factor*, where the unit is dependent on the reaction order[1], and E_a [J/mol] is the *activation energy.* Implementing the set of n reactions to the plug flow reactor model requires the specific stoichiometry matrix, $\mathbf{N}$, where ν_{ij} is the stoichiometric coefficient for species i in chemical reaction j, as given in equation (6.5).

$$\mathbf{N} = \{\nu_{ij}\} \tag{6.5}$$

Using arbitrary chosen values for the coefficients, to provide an example, the matrix can take the form:

$$\mathbf{N} = \overset{n \text{ reactions}}{\begin{pmatrix} 1 & -1 & 1 & \cdots & 1 \\ 0 & 2 & -2 & \cdots & 0 \\ \vdots & \vdots & \vdots & \ddots & \vdots \\ 1 & 1 & 0 & \cdots & -1 \end{pmatrix}} \; m \text{ species}$$

As the equation indicates, the dimension of the matrix is $n \times m$. The matrix is dependent on the reaction mechanism, where the columns can be read as the reactions, and the rows represents the species. A negative value indicates the species is being consumed, while a positive number indicates the species is being formed.

The *net* reaction rate for a species A is the sum of all the contributions of all the n reactions:

---

[1] For a first order reaction, the unit of the frequency factor is s^{-1} and for a second order reaction the unit is $\mathrm{m}^3\mathrm{mol}^{-1}\mathrm{s}^{-1}$.

$$\dot{\xi}_{\mathrm{A}} = \sum_{i=1}^{n} \dot{\xi}_{iA} = \dot{\xi}_{1A} + \dot{\xi}_{2A} + ... + \dot{\xi}_{nA} \tag{6.6}$$

The rates of all the species give the $\dot{\boldsymbol{\xi}}$ vector, shown in equation (6.7) which is multiplied with the stoichiometry matrix $\mathbf{N}$, and divided by mass to yield the changes in moles of each species in the mechanism, according to the introductory equation (6.1).

$$\dot{\boldsymbol{\xi}} = \begin{pmatrix} \dot{\xi}_{\mathrm{A}} \\ \dot{\xi}_{\mathrm{B}} \\ \vdots \\ r_m \end{pmatrix} \tag{6.7}$$

The mole balance is thus obtained and can be integrated throughout the reactor, while the concentrations, mole numbers and state temperature are updated for each integration step.

6.2 Requirements to the kinetic reaction model

The kinetic model is of great importance for the model to accurately predict the rates of the reactions and hence predict the formation of products and byproducts. Due to the time scope of the thesis it is regarded better to use an existing reaction mechanism from literature, compared to developing a new reaction mechanism, which is a much more time consuming project. The general form of the framework PYTHON program gives the possibility to add several reaction mechanisms to the model, and easily switch between these.

The most important requirement for the kinetic model from a modelling perspective is that it manages to predict the reaction rates for the input concentrations and temperature. In addition, INEOS' have requirements to what the kinetic model should include. These are listed below.

Promotor

A promotor which enhances the cracking reactions should be included in the reaction mechanism. This promotor is carbon tetrachloride, CCl_4. The effect of this can be studied by simulations with ppm levels of CCl_4 in the feed stream.

Inhibitor

One inhibitor should also be part of the reaction mechanism, to investigate the effect of impurities in the form of inhibitors in the feed stream. The inhibitor to be studied is 1,1-dichoroethane (1,1-EDC)[2].

---

[2] Other byproducts, in addition to 1,1-EDC, could potentially have inhibitory effects.

Byproducts

As one of the aims of the thesis is to model the effect of temperature profile on byproduct formation, the most important byproducts should be included in the reaction model. The most important byproducts, based on a typical product composition from INEOS, are considered to be chloroprene and benzene. Also detected in the product stream are acetylene, dichloroethane (cis/trans-1,2 and 1,1) and 1,1,2,2-tetrachloroethane. The amount of byproducts formed can also be used to verify the accuracy of the model, comparing the simulation values with plant data.

6.3 The simplified global reaction model

The simplified kinetics model is represented by the global overall reaction, where 1,2-dichloroethane (EDC) thermally decomposes to vinyl chloride monomer (VCM) and hydrochloric acid (HCl).

$$\mathrm{C_2H_4Cl_2\ \ (EDC) \rightarrow C_2H_3Cl\ \ (VCM) + HCl} \tag{6.8}$$

With this reaction scheme, the stoichiometry matrix takes the simple form given below.

$$\mathbf{N_g} = \begin{array}{cc} \begin{pmatrix} -1 \\ 1 \\ 1 \end{pmatrix} & \begin{array}{c} \text{EDC} \\ \text{VCM} \\ \text{HCl} \end{array} \end{array} \tag{6.9}$$

where the column of $\mathbf{N_g}$ represents the only reaction in this kinetic model. The rate expressions for the global model are only dependent on the state temperature and the concentration of EDC, according to the first order rate expression.

$$-\,r_{\mathrm{EDC}} = r_{\mathrm{VCM}} = r_{\mathrm{HCl}} = \mathrm{A_g} \exp\left(-\mathrm{Ea_g}/\mathrm{R}T\right) c_{\mathrm{EDC}} \tag{6.10}$$

The parameters used in this kinetic model are listed in Table 6.1. These are given from INEOS [15] and are based on plant data.

Table 6.1. The rate parameters of the global reaction model.

Parameter	Value	Unit
Frequency factor, $\mathrm{A^3}_{\mathrm{g}}$	$10^{12.6}$	cal mol^{-1}
Activation energy, $\mathrm{E_a}$	47778	s^{-1}

Although the global model can not be used for extensive predictions of e.g. the byproducts, it is convenient to use for tuning of the heat transfer model. It is also implemented first to test the framework model for a simple reaction scheme, to verify that the model and the PYTHON program behaves as desired.

6.4 The extended kinetic model

To find a more sophisticated reaction model which meets the requirements listed in section 6.2, a comprehensive literature review was performed. This is summarised in section 2.4. Based on this review and the model requirements, it was decided to use a radical chain reaction model developed by Schirmeister et al. [5], which consists of 31 reactions and 24 compounds, where eight of the compounds are radicals. This model is thus much more complex than the global reaction model, although it is simplified compared to the most advanced kinetic models with up to 800 reactions. Simplifications are done with respect to data accuracy and optimisation, according to the article presenting the reaction model [5]. The model is relatively new (from 2009), and most of the rate expression parameters are taken from literature, while some are estimated. The article also claims that the reaction mechanism is in agreement with empirical experience and studies such as Borsa [6], which is the most complex model developed.

The 31 reactions which the model is built on are shown in Table 6.2. In this table, the short forms of the species in the mechanism are used. The complete list of species is found in Table 6.3, for the stable compounds, and Table 6.4, for the radicals. The stoichiometry matrix, $\mathbf{N}_\mathrm{s}$, for the Schirmeister model has the dimension $24 \cdot 31$, which gives a matrix of 744 elements[4]. Short forms of the stable compounds and their (most frequently used) name and formula are found in Table 6.3. Radicals of the mechanism with corresponding molecular formula is shown in Table 6.4. Reaction kinetic parameters are given in Appendix B, where the origin of all the rate parameters are given for the 31 reactions. Details of the experimental estimations or calculation of these parameters are provided in these references.

---

[3] 1 calorie = 4.18400 joules

[4] The matrix is *sparse*; most of the elements are zero.

Table 6.2. The reactions of the Schirmeister reaction mechanism. Short forms for compounds are used, these are found in Table 6.3 and 6.4.

No.	Reaction equation
1	$\mathrm{EDC} \rightarrow \mathrm{R1} + \mathrm{R2}$
2	$\mathrm{CCl_4} \rightarrow \mathrm{R1} + \mathrm{R8}$
3	$\mathrm{EDC} + \mathrm{R1} \rightarrow \mathrm{HCl} + \mathrm{R3}$
4	$\mathrm{EDC} + \mathrm{R5} \rightarrow \mathrm{VCM} + \mathrm{R3}$
5	$\mathrm{EDC} + \mathrm{R2} \rightarrow \mathrm{EC} + \mathrm{R3}$
6	$\mathrm{EDC} + \mathrm{R4} \rightarrow 1,1 + \mathrm{R3}$
7	$\mathrm{EDC} + \mathrm{R6} \rightarrow 1,1,2 + \mathrm{R3}$
8	$\mathrm{EDC} + \mathrm{R7} \rightarrow 1,1,1,2 + \mathrm{R3}$
9	$\mathrm{EDC} + \mathrm{R8} \rightarrow \mathrm{CHCl_3} + \mathrm{R3}$
10	$\mathrm{VCM} + \mathrm{R1} \rightarrow \mathrm{R4}$
11	$\mathrm{VCM} + \mathrm{R1} \rightarrow \mathrm{HCl} + \mathrm{R5}$
12	$\mathrm{VCM} + \mathrm{R5} \rightarrow \mathrm{CP} + \mathrm{R1}$
13	$\mathrm{VCM} + \mathrm{R4} \rightarrow \mathrm{C_4H_6Cl_2} + \mathrm{R1}$
14	$\mathrm{VCM} + \mathrm{R2} \rightarrow \mathrm{EC} + \mathrm{R5}$
15	$\mathrm{R3} \rightarrow \mathrm{VCM} + \mathrm{R1}$
16	$\mathrm{R5} \rightarrow \mathrm{C_2H_2} + \mathrm{R1}$
17	$\mathrm{R6} \rightarrow \mathrm{Di} + \mathrm{R1}$
18	$\mathrm{R7} \rightarrow \mathrm{Tri} + \mathrm{R1}$
19	$\mathrm{EC} + \mathrm{R1} \rightarrow \mathrm{HCl} + \mathrm{R2}$
20	$1,1 + \mathrm{R1} \rightarrow \mathrm{HCl} + \mathrm{R4}$
21	$1,1,2 + \mathrm{R1} \rightarrow \mathrm{HCl} + \mathrm{R6}$
22	$1,1,1,2 + \mathrm{R1} \rightarrow \mathrm{HCl} + \mathrm{R7}$
23	$\mathrm{CHCl_3} + \mathrm{R1} \rightarrow \mathrm{HCl} + \mathrm{R8}$
24	$\mathrm{CCl_4} + \mathrm{R5} \rightarrow \mathrm{Di} + \mathrm{R8}$
25	$\mathrm{CCl_4} + \mathrm{R4} \rightarrow 1,1,2 + \mathrm{R8}$
26	$\mathrm{CCl_4} + \mathrm{R6} \rightarrow 1,1,1,2 + \mathrm{R8}$
27	$\mathrm{R2} + \mathrm{R1} \rightarrow \mathrm{VCM} + \mathrm{HCl}$
28	$\mathrm{R3} + \mathrm{R8} \rightarrow \mathrm{Di} + \mathrm{HCl}$
29	$\mathrm{R6} + \mathrm{R8} \rightarrow \mathrm{Di} + \mathrm{CCl_4}$
30	$2\mathrm{C_2H_2} + \mathrm{R5} \rightarrow \mathrm{C_6H_6} + \mathrm{R1}$
31	$\mathrm{C_2H_2} + 2\mathrm{R1} \rightarrow 2\mathrm{C} + 2\mathrm{HCl}$

Table 6.3. The stable compounds of the reaction mechanism and their short forms used in the thesis.

No.	Short form	Compound	Formula
1	EDC	1,2-dichoroethane	$C_2H_4Cl_2$
2	VCM	Vinyl chlorid	C_2H_3Cl
3	HCl	Hydrogen chloride	HCl
4	$CHCl_3$	Trichloromethane	$CHCl_3$
5	CCl_4	Carbon tetrachloride	CCl_4
6	EC	Ethyl chloride	C_2H_5Cl
7	1,1	1,1-dichoroethane	$C_2H_4Cl_2$
8	1,1,2	1,1,2-trichoroethane	$C_2H_3Cl_3$
9	1,1,1,2	1,1,1,2/1,1,2,2-tetrachloroethane	$C_2H_2Cl_4$
10	Di	1,1-/cis-/trans-dichloroethylene	$C_2H_2Cl_2$
11	Tri	Trichloroethylene	C_2HCl_3
12	CP	1-/2-chloroprene	C_4H_5Cl
13	C_2H_2	Acetylene	C_2H_2
14	C_6H_6	Benzene	C_6H_6
15	$C_4H_6Cl_2$	3,4-dichlorobutene	$C_4H_6Cl_2$
16	C	Soot/Coke	C

Table 6.4. The radicals of the reaction mechanism, their short forms used in the thesis and their formulas.

No.	Short form	Formula
1	R1	$Cl^{\bullet}$
2	R2	$CH_2Cl - CH_2^{\bullet}$ / $CH_3 - CHCl^{\bullet}$
3	R3	$CH_2Cl - CHCl^{\bullet}$
4	R4	$CHCl_2 - CH_2^{\bullet}$
5	R5	$CHCl = CH^{\bullet}$ / $CH_2 = CCl^{\bullet}$
6	R6	$CH_2Cl - CCl_2^{\bullet}$ / $CHCl_2 - CHCl^{\bullet}$
7	R7	$CHCl_2 - CCl_2^{\bullet}$ / $CCl_3 - CHCl^{\bullet}$
8	R8	$CCl_3^{\bullet}$

Thermodynamic properties, assumptions and simplifications

The already developed reaction mechanism which is utilised is built on various assumptions, whereas some of these are listed above. In addition, some simplifications and assumptions is made in the implementation of the Schirmeister model. First of all, thermodynamic properties of the eight radicals in the model are difficult to find in literature. Therefore, average values for the enthalpies of formation and heat capacities are used for these species. This is a relatively safe simplification to make, as the radicals are only present in extremely low concentrations compared to the other compounds, as they are reacting further as soon as they are formed. This implies that the radicals are not contributing significantly to the total enthalpy of the process gas, and the simplification should thus not affect the energy balance.

Another assumption which is unavoidable in the way that the Schirmeister model is given, is posed by the use of several isomers in the component list of the Schirmeister model. As an example, both the *sis* and the *trans* versions of 1,1-dichloroethylene are listed to represent one species. These two monomers have different thermodynamic properties. In these cases (three in total), properties of one of the isomers are used. This could impact the simulations, but is assumed to not have a large influence.

Reaction classes of the Schirmeister mechanism

The reactions in the mechanism are divided into different reaction classes. The reaction classes and their respective assumptions as given in the Schirmeister model are listed below.

1. **Chain initiation**
   Initiation of the reactions is assumed to proceed through reaction 1 and 2, via *homolytic cleavage* of EDC and CCl_4.

2. **Chain propagation**
   Propagation of the reactions is assumed to proceed through four mechanisms, where the two first are; *hydrogen abstraction* from a stable compound, to form new radicals (reaction 3-9, 11, 19-23) and *decay of radicals*, which forms a Cl radical (R1) and stable compounds (reaction 15-18, and final step of reaction 30). The two last modes of of propagation are addition of a radical to double bonds (*back reaction of radical decay*, reaction 10, 12-14 and initial step of reaction 30) and *Cl radical abstraction* from CCl_4 (reaction 24-26).

3. **Chain termination**
   Termination reactions and total radical concentration decrease are assumed to occur through; *H abstraction* from radicals, which forms to stable species (reaction 27-29) and *carbon (coke) formation* from acetylene in reaction 31.

These assumption are specific for this reaction model, and are not necessarily valid. The model does not include HCl split-off, catalytic reactions at the wall surfaces and other complex pathways from other possible carbon precursors, such as instance benzene and choroprene [5].

6.5 Modeling issues and numerical approaches

Radicals (or *free radicals*) tend to react quickly, as they are very reactive species due to their unpaired valence electrons. The reactions in the Schirmeister mechanism have activation energies in a wide range, 10^{10} to 10^{15}. From the range of activation energies, it is expected that the reaction rates will also be distinctly different for the set of reactions. The set of differential equations for the species in this mechanism thus pose a *stiff* equation system, which is mainly caused by the mass balance equations (reaction system). In this section the challenges associated with such modelling issues are discussed, in addition to the different solution approaches which were tested to manage these challenges.

First, to illustrate the complexity of the Schirmeister model, the complete set of reactions paths are illustrated in Figure 6.1.

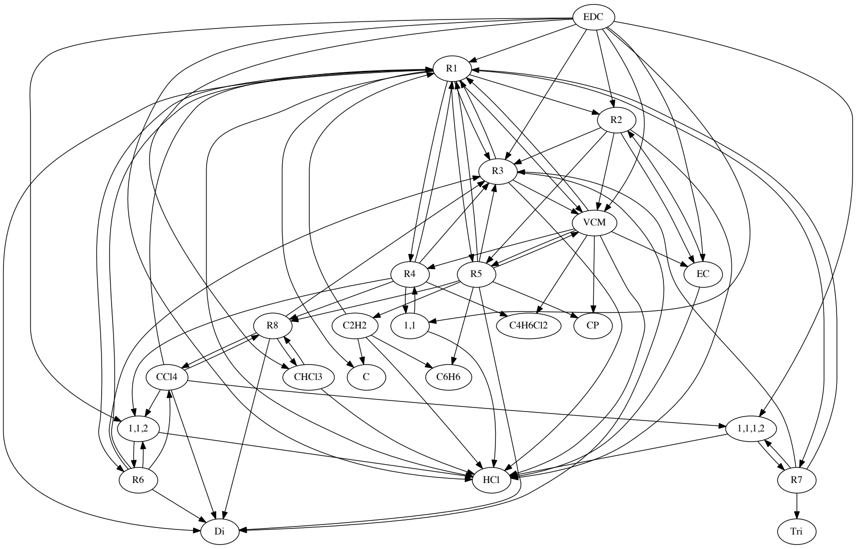

Figure 6.1. The complete reaction tree of the Schirmeister model.

Arrows in Figure 6.1 represents the reaction paths according to the 31 reactions in the model. The start node represents a reactant, whereas an end node of the arrow is (one of) the product(s). As the figure suggests, some of the species are involved in more reactions. This applies especially to the radicals R1 ($Cl^\bullet$) and R3 ($CH_2Cl - CHCl^\bullet$). Also EDC, VCM and HCl are represented in several of the reactions.

Modelling issues which were introduced by this reaction mechanism are mainly the stiffness of the system, and also negative mole rates were appearing during the integrations. These two issues are likely to be connected.

Initialisation of reaction generations

One suggested procedure to tackle the negative mole numbers was an *initialisation* procedure, to generate all the generations of species in the reaction mechanism. The different generations of species are illustrated in Figure 6.2.

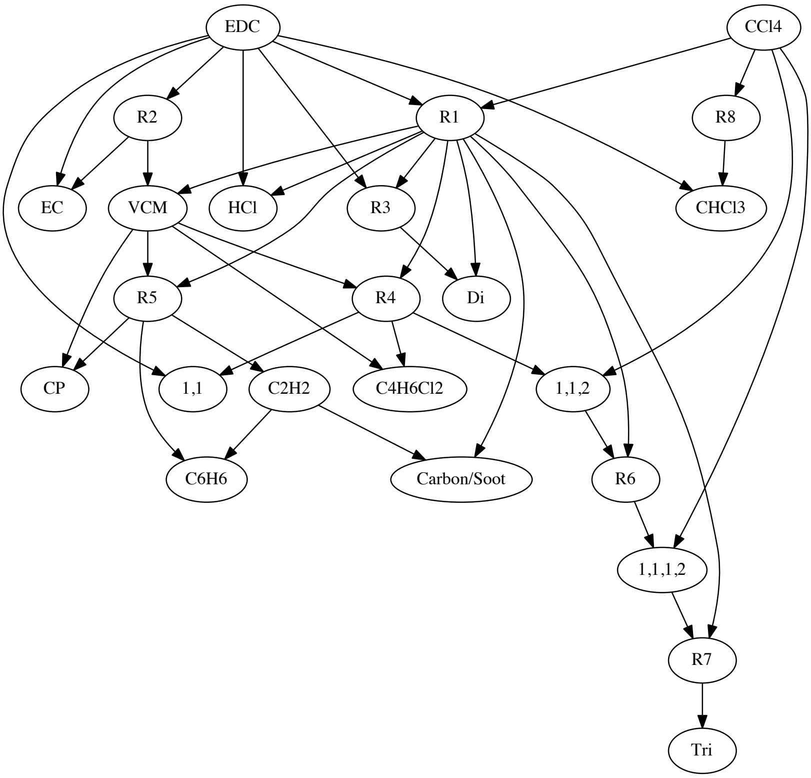

Figure 6.2. Reaction tree with main paths. The initialisation steps required to produce all components in the reaction mixture.

As Figure 6.2 illustrates, there are nine generations of species. The reaction mechanism starts, as previously explained, by the cleavage of EDC and CCl_4. The next steps included in the figure are the necessary reactions paths for all the species in the reaction mechanism to be generated. The idea behind the suggested procedure was to uncouple the thermodynamics and the energy balance for the first few steps of the integrations and let the temperature be constant, to let all the species be formed and to be present in “sufficient” amounts. When this is done, the thermodynamics and energy balance could be coupled back with the kinetics. Then negative mole rates could be avoided as the species are present in amounts large enough to start to proceed the reactions, compared to microscopic concentrations in ranges down to 10^{-50}, which is zero for all practical purposes. This procedure did, however, still produce negative values for some of the radicals.

Integrating the reactions with explicit polynomial function for temperature

A method which did yield expected mole profiles was to uncouple the energy balance and use an explicit polynomial function of temperature for the integration. The temperature polynom was obtained from plant data. A similar approach is used in Choi et al. [7]. In this procedure, the thermodynamics are updated during the integration steps (pressure and volume). The procedure gives results in agreement with plant data from INEOS, where the mole profiles resemble the expected ones. However, such a procedure is not applicable for simulations with different feed compositions and other cases of interest. This is due to the fact that the temperature profile will change if, as an example, the inlet concentration of CCl_4 is changed to a larger value. A higher value of promotor would increase the conversion, which again would lead to a lower temperature profile in the process coils, as a result of more heat being consumed in the reactions. Hence, this procedure is not regarded as sufficient for predictive simulations of the EDC cracker, and for using the simulation model for optimisation of the process.

Final integration procedure

The `SciPy` integrator `odeint` has additional optional parameters to be defined as inputs [38]. To solve the numerical issues with the integrations of the differential equation system, these options were investigated and several combinations of input parameters were tested. This involves forcing the integrator to take a maximum step length of `hmax` (the maximum absolute step length allowed) and trying to give the integrator critical values of z which were observed during integration. The conclusion from this testing was that the best approach was to let the integrator decide the step length and not trying to override this. The integrator of `odeint` which is used for stiff systems is based on a linear multistep method, which should be sufficient for this stiff equation system. The final procedure, on the other hand, involved changing the value of `mxstep`. This parameter defines the maximum number of steps allowed for each integration point. By setting this parameter to a sufficiently high value, the observed result was that the integrator finally managed to integrate through the reacton giving reasonable results. Unphysical values for the mole numbers were still an issue, however the negative numbers are close to zero. Thus, they do not seem to affect the integration significantly. The value of `mxstep` was set to 5000. The downside with this procedure is the highly increased computational time. Increasing the tolerance of step trials for each step interval makes the program much slower.

CHAPTER 7

THE HEAT TRANSFER MODEL

In order to predict the temperature inside the reaction coils of the 1,2-dichloroethane (EDC) cracker precisely, a model which describes the heat transfer from the hot combustion gases to the process fluid in the *firebox section* is necessary. This model includes heat transferred from the flue gas to the reaction coils in the form of radiation and convection, conduction through the coil wall, and finally convection in the coil pipe. The predicted process temperature is used to calculate the reaction rates in the kinetic model, which are highly temperature dependent. Hence, it is critical that the model provides an accurate prediction of this temperature, in order to give reliable results.

This chapter describes the development of the heat transfer model for the firebox section, and the assumptions and simplifications made during the development of the model. The model is implemented in the plug flow reactor (PFR) model in PYTHON as the function `firebox`[1]. Heat transfer parameters used in the heat transfer calculations are found in Appendix C.

Modeling of heat transfer in pyrolysis furnaces is reported in several studies in the literature, and is usually part of the coupled cracker model [1, 5, 8, 14, 45]. The developed heat transfer model in this study is inspired by these. However, several studies use computational fluid dynamics (CFD) or zonal methods (discretized) for modelling of the furnace. For this study, a more simplified approach is used, as will be presented.

7.1 Heat transfer in furnace

Combustion, which occurs in the burners at the firebox wall, is the source of heat in the cracker furnace. Heat from the flue gas of the combustion will be

---

[1] The simple adiabatic volume energy balance with $q = 0$ is implemented as the function `adiabatic`.

transferred mainly in the form of radiation and convection. The overall energy balance for the system (reaction coils) is written

$$\dot{Q}_{\text{rad}} + \dot{Q}_{\text{conv}} - \dot{Q}_{\text{loss}} = \dot{Q}_{\text{cond}} = \dot{H}_{\text{preheating}} + \dot{H}_{\text{vap}} + \dot{H}_{\text{rx}} \qquad (7.1)$$

In equation (7.1), $\dot{Q}_{\text{rad}}$ is the radiative heat transfer rate to the coil and $\dot{Q}_{\text{conv}}$ is convective heat transfer rate to the coil. $\dot{Q}_{\text{loss}}$ represents the heat loss rate to the surroundings and $\dot{Q}_{\text{cond}}$ is the conduction heat transfer rate through the pipe wall. $\dot{H}_{\text{rx}}$, $\dot{H}_{\text{preheating}}$ and $\dot{H}_{\text{vap}}$ represent the changes in enthalpy as a result of the pyrolysis reactions, preheating (convection section) and heat of vaporization. As the equation indicates, some of the combustion heat from the combustion in the furnace is used to preheat and evaporate the 1,2-dichloroethane (EDC). These processes are mostly occurring in the convection and shock section. Most of the generated heat is used in the endothermic cracking reactions in the firebox (radiation) section, where EDC thermally decomposes. The heat loss from the furnace is mostly through the flue gas existing at the stack. Some heat is also lost through the furnace wall.

Energy balance for firebox section

The aim of the heat transfer model is to predict the heat transfer to the reaction coils[2], as a function of the dimensionless reactor length, z, given as

$$\left(\frac{\partial h}{\partial z}\right)^{(ss)} = Cq(z) \qquad (7.2)$$

where (capital) C is the circumference of the coil section, which should not be confused with the symbol for moles per kilogram from the mass balance, c. To find a model for the heat load $q(T, z)$ (energy per mass) in equation (7.2), the energy balance of the firebox section is required.

The different modes of heat transfer in the firebox are illustrated in Figure 7.1, which gives an overview of the heat transfer model. As can be seen in this figure, there is a radial temperature gradient in the coil segment. As a one dimensional plug flow reactor (PFR) model is utilized, a *mean* temperature is used for the process gas. Temperature gradients in the furnace are also neglected, with the assumption of an *isothermal* and *uniform* furnace temperature.

Further developing the energy balance for the firebox section, the different heat contributions are elaborated as follows

---

[2] As described in Chapter 3, the heat transfer is based on heat per mass and surface area

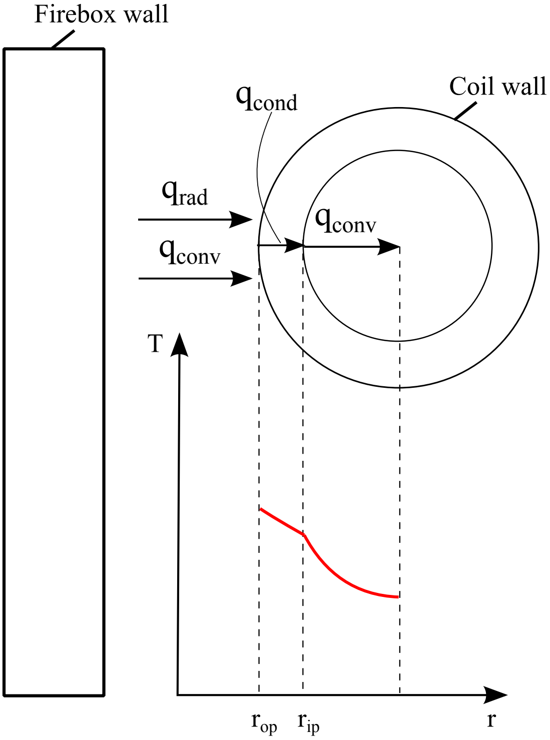

Figure 7.1. The plug flow reactor coil with heat transfer. $q_{\mathrm{rad}}[W]$ = heat transfer through radiation, q_{conv} = heat transfer through convection and q_{cond} = heat transfer through conduction. Below the reaction coil, an illustrative temperature profile (as a function of radial position) is shown. r_{op} and r_{ip} are the outer and inner radius, respectively.

$$\begin{aligned}\underbrace{\mathrm{A}_{\mathrm{so}}\sigma(\varepsilon_{\mathrm{f}}T_{\mathrm{f}}^4-\alpha_{\mathrm{f}}T_{\mathrm{po}}^4)}_{\text{Radiation flue gas to coil}} \quad + \quad \underbrace{\mathrm{A}_{\mathrm{so}}h_{\mathrm{f}}(T_{\mathrm{f}}-T_{\mathrm{po}})}_{\text{Convection flue gas to coil}} \quad &= \\ \underbrace{\frac{2\pi\mathrm{L}k_{\mathrm{coil}}}{\mathrm{d}_{\mathrm{pi}}\ln(\mathrm{d}_{\mathrm{po}}/\mathrm{d}_{\mathrm{pi}})}(T_{\mathrm{po}}-T_{\mathrm{pi}})}_{\text{Conduction through coil wall}} \quad = \quad \underbrace{\mathrm{A}_{\mathrm{si}}h_{\mathrm{p}}(T_{\mathrm{pi}}-T)}_{\text{Convection to center of coil}} &\end{aligned} \tag{7.3}$$

where σ is *Boltzmann's constant* ($\sigma = 5.67{\cdot}10^{-8}\ \mathrm{Wm^{-2}K^{-4}}$), ε_{f} is the flue gas emissivity, α_{f} is the absorptivity of the flue gas and k_{coil} is the conductivity of the coil. For the convection terms, h_{f} and h_{p} are the convection coefficients of the flue gas and the process gas (in the PFR), respectively. A_{so} and A_{si} are the surface areas of the outer and inner coil, while d_{po} and d_{pi} [m] are the outer and inner diameters of the coil pipe. The temperatures T_{f}, T_{po} , T_{pi} and T are the temperatures of the flue gas, outer coil wall, inner coil wall and process fluid, respectively. The following requirement should be valid for the temperatures in the model:

$$T_{\mathrm{f}} > T_{\mathrm{po}} > T_{\mathrm{pi}} > T \tag{7.4}$$

The different terms of the energy balance, and the developed numerical solution procedure will be described later in this chapter. First, the general assumptions and the combustion will be given attention.

7.2 General assumptions in the heat transfer model

As heat transfer modelling is a complex field of study, especially when it comes to radiative heat transfer, several simplifications and assumptions are made in the model to make the differential equation for the heat balance solvable in the PYTHON program. The following list mentions the most essential assumptions.

Steady state

The cracker model is developed for steady state simulations, and this assumption is also applied to the heat transfer model. Heat rate laws are thus based on steady state rate laws, where heat transfer rate is constant for a certain value of z, but is varying with the axial coordinate through the reactor.

Isothermal furnace temperature

For simplification, a uniform and isothermal temperature is assumed for the furnace temperature. More complex temperature gradients can be difficult to obtain unless *computational fluid dynamics* (CFD) tools are used. A possibility for a more advanced model could be to divide the furnace into zones, according to the *zonal method*[3]. However for this time scope and work, the simplified model is regarded as sufficient. The composition of the flue gas is also assumed to be constant.

Ideal blackbodies and the *gray gas model*

The outer coil surfaces are assumed to be idealized blackbodies, which absorb all incident radiation. For the radiation calculations, the gray gas model is used. It is a simplified model which could potentially introduce errors to the model. However, more advanced band models require much more computational power and time, and are therefore not considered as

---

[3] The zone method was first introduced by Hotell, and has been further improved by Cohen, Hotell and Sarofim [46]. In this method, the furnace is divided into several surface and volume elements, where the temperature and radiation properties are assumed to be uniform in each zone.

convenient to use in this case. Only CO_2 and H_2O are assumed to absorb and emit radiation in the flue gas mixture[4].

Heat loss

Heat loss in the furnace is occurring through the flue gas and to a small extent through the furnace walls. However, the heat model is set up without regarding this heat loss. This is due to the fact that the temperature of the furnace is nevertheless used as a tuning parameter, as discussed later.

Scattering in flue gas is neglected

As the flue gas consists mainly of nitrogen, water vapour, oxygen and carbon dioxide, it is regarded as a safe assumption to neglect scattering. It has been argued that this is a valid assumption, as scattering is of minor influence unless the gas is containing larger particles, e.g. dust [34].

Reaction coils are opaque to transmission

Modelling of surface radiative heat transfer is usually done with the assumption of opaque, diffuse walls [45]. For the model developed in this thesis, the reaction coils are assumed to be opaque to transmission.

Property dependency on temperature and not pressure

The relevant heat transfer properties are assumed to be dependent on temperature and not pressure. This applies to the dynamic and kinematic viscosities, thermal conductivities and Prandtl numbers. Values for different variables are looked up in tables, and the values used are listed in Appendix C. For temperatures which lay between the table values, interpolation is used through polynomial fitting of the curves for the variable plotted against temperature. Care is taken when interpolation is performed.

Shadow effects

So-called shadow effects for the two coil pipes are neglected. This is worth noticing as the reactor consists of two pipes in parallel. There is a probability that shadow effects could lead to a lower actual heat absorption than the one estimated, as studies have suggested [45]. However, the two pipes are shifted vertically to minimise such effects. Additionally, the uncertainty which is already introduced by using the gray gas model is assumed to be higher and thus this simplification is not decisive.

7.3 Generation of heat - combustion of fuel gas

The heat in the firebox is generated through combustion of the *fuel* gas. For the heat calculations, the composition of the *flue* gas (combustion product)

---

[4] Trace amounts of nitrous compounds such as NO_x and CO from incomplete combustion are neglected.

and the velocity of this gas through the firebox section are required[5]. The composition of the flue gas is assumed to be the one given in Table 7.1[6].

Table 7.1. The fuel gas composition.

Compound	Compound name	Concentration [vol%]
CH_4 (g)	Methane	36
H_2 (g)	Hydrogen	63
C_2H_6 (g)	Ethane	1.0

As Table 7.1 shows, the fuel gas consist mostly of methane and hydrogen gas. The *excess air coefficient*, λ, is held at approximately 1.15-1.20 (15-20% excess air), in case of periods where the fuel gas composition deviates from the one given in the table.

Combustion is a difficult process to model mathematically, as it involves the simultaneous processes of radiative and convective heat transfer, turbulent mixing, fuel evaporation and chemical kinetics [32]. However, with a few simplifications, the flue gas composition can be calculated. The combustion equations for each fuel gas species is then required. The general form of the combustion equation of hydrocarbons burning with excess air is as follows.

$$\mathrm{C_xH_y} + \mathrm{z}\lambda(\mathrm{O_2} + 3.76\mathrm{N_2}) \rightarrow \mathrm{xCO_2} + \frac{\mathrm{y}}{2}\mathrm{H_2O} + \mathrm{z}(\lambda - 1)\mathrm{O_2} + \mathrm{z}\lambda 3.76\mathrm{N_2} \tag{7.5a}$$

$$\mathrm{z} = \mathrm{x} + \frac{\mathrm{y}}{4} \tag{7.5b}$$

For the three species in the fuel gas, this yields the following balanced combustion reaction equations.

$$\textbf{Methane}: \mathrm{CH_4} + 2\lambda(\mathrm{O_2} + 3.76\mathrm{N_2}) \rightarrow \mathrm{CO_2} + 2\mathrm{H_2O} + 2(\lambda - 1)\mathrm{O_2} + 7.52\lambda\mathrm{N_2} \tag{7.6a}$$

$$\textbf{Hydrogen}: \mathrm{H_2} + 0.5\lambda(\mathrm{O_2} + 3.76\mathrm{N_2}) \rightarrow \mathrm{H_2O} + 0.5(\lambda - 1)\mathrm{O_2} + 1.88\lambda\mathrm{N_2} \tag{7.6b}$$

$$\textbf{Ethane}: \mathrm{C_2H_6} + 3.5\lambda(\mathrm{O_2} + 3.76\mathrm{N_2}) \rightarrow 2\mathrm{CO_2} + 3\mathrm{H_2O} + 3.5(\lambda - 1)\mathrm{O_2} + 13.16\lambda\mathrm{N_2} \tag{7.6c}$$

---

[5] Composition and velocity of the flue gas is required for estimation of the gas emissivity and absorptivity, as well as the convection coefficient for heat transfer from the flue gas to the coil.

[6] The fuel gas composition is based on a typical fuel gas composition at INEOS' VCM plant at Rafnes.

In these equations, $3.76 = c_{\mathrm{g}}^{\mathrm{vol}}/c_{\mathrm{O_2}}^{\mathrm{vol}} = 79/21$, i.e. the ratio between the volume concentration of "other gases" and oxygen in the air. The air is assumed to consist of only oxygen and nitrogen, hence the nitrogen concentration in the air is assumed to be 79 vol%.

Assuming complete combustion for the three combustion reactions, (7.6a)-(7.6c), the composition of the flue gas (product of combustion) is calculated. Analysis of the flue gas at INEOS gave an oxygen value of 3.3 vol%, so the parameter λ was "tuned" to give this oxygen composition. This gave an excess air value of 21%, or equivalently $\lambda = 1.21$. The composition of flue gas is found in Table 7.2.

Table 7.2. The flue gas composition (after combustion)

Compound	Compound name	Concentration [vol%]
CO_2 (g)	Carbon dioxide	20.1
H_2O (g)	Water vapor	5.54
O_2 (g)	Oxygen	3.28
N_2 (g)	Nitrogen	71.1

The procedure to calculate the required mass of fuel gas, which is needed to find the velocity of the flue gas for convection calculations, is found in Appendix E.

7.4 Radiation flue gas to coil

To estimate the radiative heat transfer to the coil, the emissivities and absorptivites of the flue gas are estimated using the gray gas model. As the data from Hottel's charts have a large experimental uncertainty[7], Leckner's charts are utilised for the estimation of gas mixture emissivity and absorptivity, as these are claimed to have a higher accuracy [33].

From Leckner, the following set of equations are used to estimate the emissivity and absorptivity, according to the second order polynomials given.

$$\ln \varepsilon = a_0 + \sum_{i=1}^{2} a_i \lambda^i \tag{7.7a}$$

$$a_i = c_{0i} + \sum_{j=1}^{2} c_{ij} \tau^j \tag{7.7b}$$

The coefficients c_{ij} for CO_2 and H_2O are found in Leckner [47], and are given in Appendix D. λ and τ are obtained from the following expressions.

---

[7] The data are obtained in 1954, and especially the high temperature values pose high uncertainties due to extrapolation [33].

$$\lambda = \log(pL_e) \tag{7.8}$$

$$\tau = \frac{T}{1000} \tag{7.9}$$

Here, L_e is the characteristic length obtained as in equation (4.14), with the surface area being the total area of the coils. T_f is the temperature of the flue gas. As the furnace (flue gas) temperature is constant in the calculations, the emissivity remains constant. The absorptivity however is calculated at the outer pipe temperature, T_po. The obtained $\varepsilon_{\mathrm{CO_2}}$, $\varepsilon_{\mathrm{H_2O}}$, $\alpha_{\mathrm{H_2O}}$ and $\alpha_{\mathrm{CO_2}}$, in addition to $\Delta\varepsilon$ and $\Delta\alpha$ (also obtained from Leckner), are added to find the total gas emissivity and absorptivity:

$$\varepsilon_\mathrm{f} = \varepsilon_{\mathrm{CO_2}} + \varepsilon_{\mathrm{H_2O}} - \Delta\varepsilon \tag{7.10a}$$

$$\alpha_\mathrm{f} = \alpha_{\mathrm{H_2O}} + \alpha_{\mathrm{CO_2}} - \Delta\alpha \tag{7.10b}$$

Plots of the total gas emissivity and absorptivity are given in Figure 7.2. Here, the flue gas temperature is set to $\mathrm{T_f} = 1170$ K for the absorptivity calculation, with a varying outer coil pipe temperature, T_po. For the emissivity calculation, the flue gas temperature, T_f, is varying.

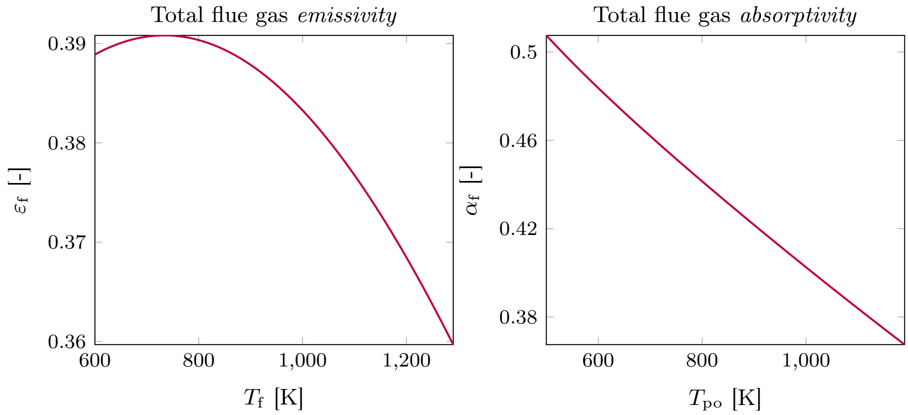

Figure 7.2. Total flue gas emissivity and absorptivity. To the left: flue gas emissivity,ε_f, as a function of flue gas temperature. To the right: absorptivity as a function of outer pipe wall (surface) temperature, with the flue gas temperature set to 1170 K.

In the heat transfer model, the flue gas emissivity is set to a constant value, depending on the value set for T_f. For the absorptivity, the value is varying as the outer coil pipe temperature is varying. This is calculated consecutively as the integration through the reactor proceeds, based on a polynomial fit of the absorptivity (which is calculated based on the constant flue gas temperature). Additional plots of the emissivity and absorptivity of H_2O and CO_2, respectively, are found in Appendix D.

Finally, the radiative heat transfer rate from the flue gas to the pipe section is obtained by

$$q_{\mathrm{rad}} = \mathrm{A}_{\mathrm{so}}\sigma\left(\varepsilon_f T_{\mathrm{f}}^4 - \alpha_{\mathrm{f}} T_{\mathrm{s}}^4\right) \tag{7.11}$$

where A_{so} is the outer surface area of the coils.

7.5 External and internal convection - flue gas and process gas

To estimate heat transfer through convection from the flue gas to the outer coil, and between the inner coil to the process gas, the convection coefficients must be estimated. The first case is characterised as *external flow*, while the latter can be said to be a type of *internal flow*.

Convective heat transfer from flue gas to coil

The convection coefficient for the external flue gas to the coil pipe can be estimated through a correlation for the Nusselt number. As the Nusselt number is a function of the Reynolds and Prandtl number, ref. equation (4.3) in Chapter 4, these are first calculated.

The Reynolds number of the process fluid is calculated through equation (7.12)

$$Re_{d_{\mathrm{po}}} = \frac{u_{\mathrm{f}} d_{\mathrm{po}}}{\nu_{\mathrm{f}}} \tag{7.12}$$

where d_{po} is referring to the outer pipe diameter and u_f is the velocity of the flue gas. The Prandtl number for the gases are found as a function of temperature in Incropera and DeWitt [9].

To calculate the Nusselt number, first the *bank of tubes* approach was tested[8]. However, based on the Re number (which was found to be in the range of 10^2-10^3), the flow through the pipes was approximated as if there was one single, isolated cylinder. The utilised correlation for the isolated cylinder approach is

---

[8] The bank of tubes approach is a correlation for the Nusselt number, when the flow case is external flow through a bank of staggered or aligned tubes [9].

$$Nu_{\mathrm{f}} = \frac{h_{\mathrm{f}}\mathrm{d_{po}}}{k_{\mathrm{f}}} = CRe_{d_{po}}^{m}Pr^{1/3} \tag{7.13}$$

where Nu_{f} refers to the Nusselt number for the external flow of flue gas around the reaction pipes, and k_f is the thermal conductivity of the fluid (flue gas). C and m are obtained from Incropera and DeWitt [9], for a Reynolds number in the range of 40-4000 ($C = 0.683$, and $m = 0.466$). The relation in equation (7.13) is used for $Pr \gtrsim 0.7$, which holds for the flue gas (the gases all have a Pr number of approximately 0.7). The thermal conductivity, k_{f}, is calculated as an average for the flue gas composition given as

$$k_{\mathrm{f}} = \sum_{i=1}^{n} x_i k_i \tag{7.14}$$

where the flue gas is consisting of n components and species i has a thermal conductivity k_i and volume (molar) fraction x_i. Using equation (7.14) might give an overprediction of the thermal conductivity of the flue gas mixture [48, 49]. In the convection coefficient calculations, all temperature dependent properties are evaluated at the flue gas temperature.

Convection in coil pipe

The convection coefficient for the internal flow in the reaction pipes is found in a similar approach to the one described in the last section. The Nusselt number relation used in this case is known as the *Dittus-Boelter equation*, for turbulent flow in a smooth circular tube [9, 45], given as

$$Nu_D = 0.023Re_{d_{pi}}^{4/5}Pr^{n} \tag{7.15}$$

where $n = 0.4$ for heating, which is the case for the coil pipe. The correlation in equation (7.15) is experimentally confirmed to be valid for the following conditions:

$$0.6 \lesssim Pr \lesssim 160$$

$$Re_D \gtrsim 10000$$

$$\frac{L}{D} \gtrsim 10$$

These conditions are met in the reaction pipes. The Reynolds number of the internal pipe is calculated through equation (7.17).

$$Re_{d_{pi}} = \frac{u_{\mathrm{p}}\mathrm{d}_{\mathrm{pi}}}{\nu_{\mathrm{p}}} = \frac{\rho_{\mathrm{p}} u_{\mathrm{p}}\mathrm{d}_{\mathrm{pi}}}{\mu_{\mathrm{p}}} \tag{7.17}$$

In this case the characteristic length is the inner pipe diameter, d_{pi} . Ideal gas law is used to calculate the density of the process gas fluid, ρ_{p}, to obtain the kinematic viscosity, ν_{p}, from the dynamic viscosity, μ_{p}. The process gas properties are evaluated at the state temperature T.

The convection coefficient of the internal flow in the process pipe is eventually calculated from equation (7.18).

$$Nu_{\mathrm{p}} = \frac{h_{\mathrm{p}} d_{\mathrm{pi}}}{k_{\mathrm{p}}} \tag{7.18}$$

7.6 Conduction through the pipe wall

The temperature drop through the coil wall is dependent on the heat conductivity of the coil material[9]. Conductive heat transfer through a potential coke layer is neglected. This heat layer would introduce an additional resistance to the heat transfer, as illustrated in Figure 7.3.

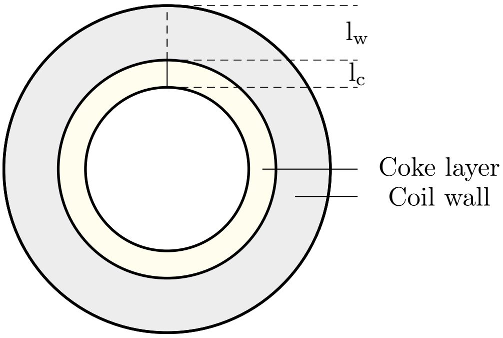

Figure 7.3. The coil wall with a coke layer increasing the overall heat transfer resistance (and decreasing the overall heat transfer conductvity). l_{w} and l_{c} are the thicknesses of the coil wall and the coke layer, respectively.

If coke resistance was added to the model, the problem would be regarded as conduction processes in series. In such cases, heat transfer coefficients add inversely [9]:

$$\frac{1}{h} = \frac{1}{h_{\mathrm{w}}} + \frac{1}{h_{\mathrm{coke}}} \tag{7.19}$$

---

[9] The coil is made of Incoloy/Inconel 800 HT.

where h_{coke} and h_{w} are the heat transfer coefficients of the coke layer and the coil wall, respectively. Fouling layers, which could also potentially increase the heat resistance, are also neglected, and thus neither coke or fouling is taken into account in the total heat transfer calculations.

For the conductive heat transfer calculation, the conduction relation for a cylindrical wall is used, which follows the equation [9][10]:

$$q_{\mathrm{cond}} = \frac{2k_{\mathrm{w}}}{d_{pi}\ln(\mathrm{d_{po}}/\mathrm{d_{pi}})}\left(T_{\mathrm{po}} - T_{\mathrm{pi}}\right) \tag{7.20}$$

where k_{w} is the thermal conductivity of coil. T_{po} and T_{pi} are the temperatures of the outer and inner pipe wall, respectively.

7.7 Numerical solution procedure of the heat transfer model

The heat transfer model returns the value q, which is the heat transferred from convection and radiation to the coil pipe. As this model is coupled to the kinetic model as described earlier, the state temperature, T, will be given (from the last state update) for the heat calculations[11].

There are then three unknown temperatures: T_{f}, T_{po} and T_{pi}. The suggested solution procedure is to use the isothermal temperature in the furnace as a tuning parameter, and “guess” values for this until the model gives accurate values according to experimental plant data. PYTHON’s `fsolve()` function (part of `SciPy`’s `optimize` module) is used to find the roots of the following set of nonlinear equations[12]:

$$\mathrm{A_{so}}\sigma(\varepsilon_{\mathrm{f}}T_{\mathrm{f}}^4 - \alpha_{\mathrm{f}}T_{\mathrm{po}}^4) + \mathrm{A_{so}}h_{\mathrm{f}}(T_{\mathrm{f}} - T_{\mathrm{po}}) - \frac{2\pi \mathrm{L}k_{\mathrm{coil}}(T_{\mathrm{po}}, T_{\mathrm{pi}})}{\mathrm{d_{pi}}\ln(\mathrm{d_{po}}/\mathrm{d_{pi}})}(T_{\mathrm{po}} - T_{\mathrm{pi}}) = 0 \tag{7.21a}$$

$$\frac{2\pi \mathrm{L}k_{\mathrm{coil}}(T_{\mathrm{po}}, T_{\mathrm{pi}})}{\mathrm{d_{pi}}\ln(\mathrm{d_{po}}/\mathrm{d_{pi}})}(T_{\mathrm{po}} - T_{\mathrm{pi}}) - \mathrm{A_{si}}h_{\mathrm{p}}(T_{\mathrm{pi}} - T) = 0 \tag{7.21b}$$

A third equation, for the thermal conductivity of the coil material is added. This is a function of temperature, as the equations indicate. The coil wall

---

[10] The equation for cylindrical conduction does not give a linear temperature profile, as for a plane wall.

[11] The initial temperature is given, and for the next steps this temperature is returned after the state updates, after the program solves for T, V and $\mathbf{c}$ through the thermodynamic solver `hpn_vs_tvn_solver()`.

[12] A Newton-Raphson procedure could also have been applied, but the built in module is used for convenience.

conductivity is evaluated at the average temperature of T_{po} and T_{pi}. Additionally, a fourth equation is added for the polynomial of gas absorptivity. The four equations, as well as guessed values for T_{po}, T_{pi}, k_{coil} and α_{f}, are passed to `fsolve()`. The converged values of these are returned and used to calculate the head transfer to the reactor, which is then used to find the state temperature. This procedure is repeated for different values of T_{f} until the conversion and temperature profile is close to the experimental plant data for these variables. Reasonable values for T_{po} and T_{pi} should also be achieved.

Chapter 8

Results and discussion

The cracker model developed in Chapter 5 - 7 is used to run simulations of the industrial reactor. The aim of the simulations is to evaluate the *validity* of the model, through comparison with plant data. It is also of interest to investigate the *behavior* of the model for different initial conditions. More specifically, the effect of temperature on the conversion and byproduct formation is evaluated. In addition, the effects of the promotor, carbon tetrachloride (CCl_4), and the inhibitor, 1,1-dichloroethane (1,1-EDC), are studied.

In this chapter, the results from the simulations are presented. Simulations were conducted for both the global reaction model and the extended (Schirmeister et al. [5]) kinetic model. The global reaction model is based on the overall reaction, where the parameters are fitted according to plant data. Hence, this model is only descriptive, in contrast to the extended kinetic model, which is predictive. Data obtained through simulations are compared to plant data, for the cases when such data are available. Several simulation cases were run for the extended kinetic model. This include simulation with the nominal feed composition, varying flue gas temperature and with varying feed concentration of the promotor CCl_4 and the inhibitor 1,1-EDC, respectively.

In the figures of this chapter, the firebox is scaled to the range $0 \leq z < 1$ and the adiabatic volume is scaled according to the range $1 \leq z \leq 1.5$. For clarity, the above mentioned ranges are expressed as;

$$z\ \text{range} = \begin{cases} \text{Firebox section}, & 0 \leq z < 1 \\ \text{Adiabatic section}, & 1 \leq z \leq 1.5 \end{cases} \tag{8.1}$$

A basis of 1 $\mathrm{kg\,s^{-1}}$ for the feed mass flow rate is used in the simulations. The actual total mass rate is approximately 15.4 $\mathrm{kg\,s^{-1}}$. Conversion refers to the *weight basis* conversion of 1,2-dichloroethane (EDC), as defined in equation

(3.26) in Chapter 3, and the selectivity is defined on a molar basis, as defined in equation (3.27) in the same chapter.

8.1 The global reaction model

In order to validate the heat transfer model and to investigate the behavior of the global reaction model, simulations with this kinetic model coupled with the developed heat transfer model were conducted. This kinetic model only includes EDC, vinyl chloride monomer (VCM) and hydrochloric acid (HCl). For these simulations, the isothermal flue gas temperature in the furnace was given the value $T_f = 1177$ K (904 °C), to approximately meet the industrial conversion of 60 wt%. Both the Euler and Runge-Kutta integration routines were sufficient for the numerical integrations with this kinetic model.

Key results from simulation with global reaction model

Key values which summarises the simulation with the global reaction model are presented in Table 8.1.

Table 8.1. Key values obtained from simulations with global reaction model

Variable	Model value	Measured value
Conversion, firebox	55-57 wt%	51 wt%
Conversion, final	60 wt%	60 wt%
Temperature at outlet of firebox	498.6 °C	494.1 °C
Temperature, final	450.0 °C	453.6 °C

As indicated in Table 8.1, overall the model gives values within reasonable deviation from plant data. The values from the table will be discussed in more detail in the next sections.

Mass fractions of the components

The obtained mass fractions for the simulation with the global reaction model are presented in Figure 8.1. As Figure 8.1 suggests, there is no reaction in the system until a certain value of z is reached, which corresponds to a critical temperature. The mass of VCM and HCl in the product stream fit the plant data to a sufficient degree. The two products are formed in equal molar amounts according to the global reaction. However, the mass profiles of VCM and HCl are shown in Figure 8.1 to differ, as VCM has a higher molecular weight. The obtained product composition gives a conversion of 60 wt.%, which is in agreement with the plant value [15]. Out of the firebox section, the simulation gives a conversion of 51 wt.%. According to plant data this value should be around 55-57 wt.%, with an increase in the adiabatic section of about 3-5 wt.% [15].

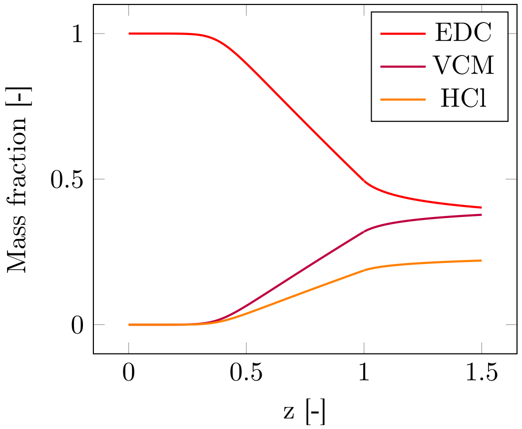

Figure 8.1. Mass fractions from simulation with global reaction model. $T_\mathrm{f} = 1177$ K ($= 1450$ °C), and the feed contains pure EDC.

Thus, the conversion at the end of the firebox section is underestimated, while the conversion in the adiabatic volume is overestimated by the model. This is further elaborated in the discussion of temperature profiles in the next section.

Temperature profiles - firebox section and adiabatic volume

Estimated model temperatures from the simulation with the global reaction model is given in Figure 8.2. Figure 8.2 shows that the temperatures of the

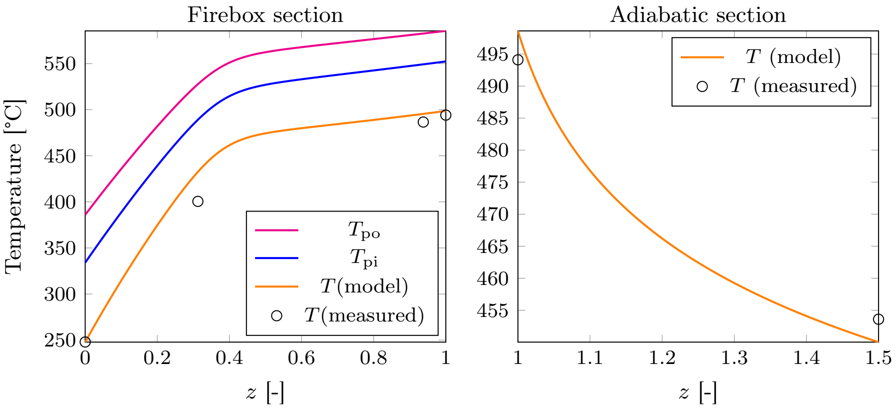

Figure 8.2. Temperatures from simulation with global reaction model. The left plot shows the temperatures in the firebox section, where T_po is the outer coil pipe temperature and T_pi is the inner coil pipe temperature.

outer coil pipe (T_po), inner coil pipe (T_{pi}) and process gas (T) temperature are correlated, which is essentially a result of the developed heat transfer model (see Chapter 7). As expected, the process temperature is stabilizing as the endothermic reactions start. According to the model outputs for mass fractions and temperatures, a detectable conversion is found at approximately 350 °C. However, at 461 °C the conversion is still below 4 wt%, which is in accordance with the simulations performed by Schirmeister et al. [5]. Figure 8.2 also indicates that the simulated temperature in the reactor is higher than the measured values, especially at the second experimental measurement. Here, the simulation temperature reaches the maximum deviation of 8% from the measured temperature, whereas the final temperature out of the firebox deviates with 1% from the measured value (corresponding to an error of 4 °C).

For the outer coil pipe temperature, T_{po}, the range is found to be approximately 560-585 °C. This is higher than the reported values of approximately 530-560 °C from thermographic measurements performed at INEOS' industrial cracker [15]. No plant measurements exist for the inner pipe temperature, hence presently making comparison impossible. With the inaccuracy introduced by use of the gray gas model for the heat transfer calculations, a deviation of approximately 10 % for the outer pipe temperature is deemed to be acceptable. A small error in the emissivity or absorptivity calculated from Leckner's charts [47][1] would lead to a large error in the heat transfer calculations, as $\dot{Q}_{\text{rad}} \propto T^4$. Errors are also introduced assuming an isothermal flue gas temperature. While this assumption does not hold in practice, it appears that the calculations give satisfying results in this case.

Regardless, the process gas temperature is the most important prediction from the heat transfer model, as it governs the kinetics. The deviation in this temperature is smaller than the deviations of T_{po} and T_{pi}. The other temperatures are used as a step to estimate the process gas temperature, and thus error in these variables does not directly affect the reaction kinetics.

In the adiabatic volume section, a temperature drop is expected as $\dot{Q}_{\text{ad}} = 0$. Thus, the temperature will decline as the pyrolysis reactions proceed and thus absorb more heat. This decline is observed in the simulation. The inlet temperature of the adiabatic volume (at $z = 1.0$) deviates with 1% from the plant data. For the outlet of the adiabatic volume, the deviation of the calculated temperature to the measured temperature is approximately 4 °C, which also corresponds to a deviation of 1%. Thus, Figure 8.2 suggests that the model predicts the temperature in the adiabatic volume with reasonable accuracy.

---

[1] The maximum error for the emissivities calculated from Leckner's chart is estimated to be around 10% [33].

Heat transfer rates, firebox section

To study the heat input to the reactor, the convective and radiative heat transfer rates are shown in Figure 8.3. The convective heat transfer is the external convection to the outer coil. Here, $z \subset [0, 1)$, as heat transfer is restricted to the firebox section.

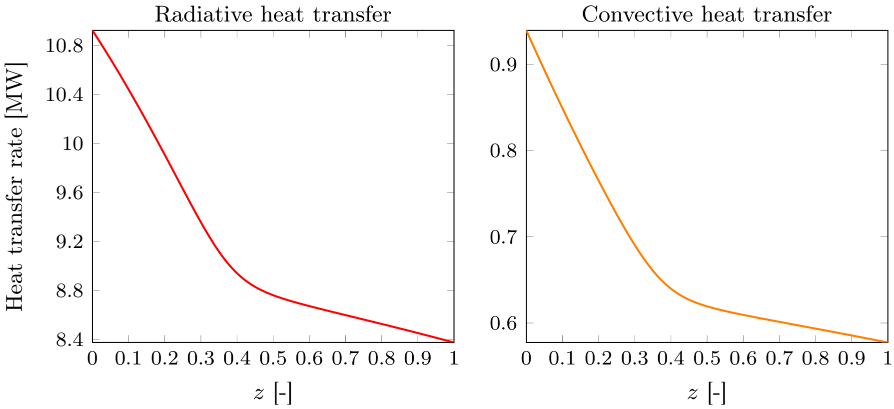

Figure 8.3. Heat transfer rates from simulation with the global reaction model. Note the different scales in the two plots, and that the heat transfer rate here is the total heat transfer to the reactor of industrial size.

As Figure 8.3 indicates, the radiative heat transfer accounts for most of the total heat transfer to the reactor. Note that in these plots, the *total* heat rates according to the industrial size of the reactor are used, and not per 1 $\mathrm{kg\,s^{-1}}$ gas fed to the reactor. Convective heat transfer contributes with less than 8% (between 6.5% and 8%) of the heat absorbed by the coil surface. In the literature, the convective heat transfer rate is typically reported to be less than 5% of the total heat rate [5]. Hence, the simulation results are regarded as reasonable.

Reaction rates

Figure 8.4 presents the reaction rates (of formation) of VCM and HCl through the firebox and the adiabatic volume. By examining Figure 8.4 it is seen that the reaction rate is negligible up to approximately 25% of the reactor volume. At this point, the reaction rate increases steeply before it reaches a maxima and declines slightly towards the end of the firebox. The maximum rate is reached when the concentration of EDC is still high, and the temperature is close to the maximum value. Recalling that the rates are exponentially dependent on the temperature according to the Arrhenius equation (given in equation (6.4)), the steep curve of the reaction rate in the firebox section is reasonable. Similarly,

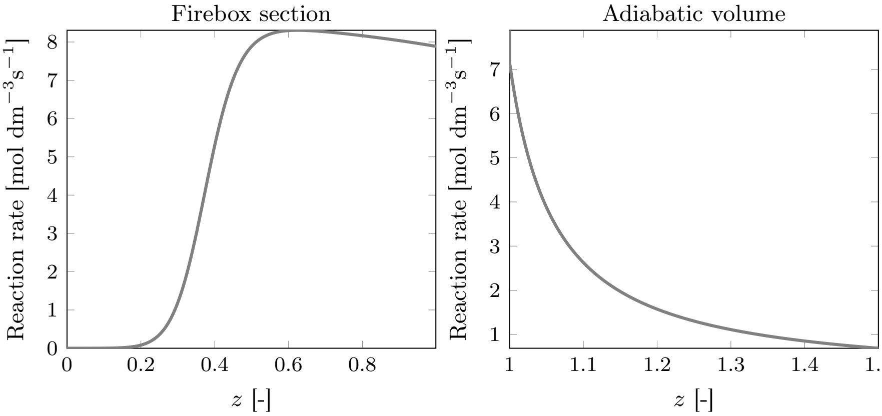

Figure 8.4. Reaction rate (formation of VCM and HCl) through the reactor.

this exponential dependence appears in the steep decline of the reaction rate in the adiabatic section. This decline in rate is explained both by the declining temperature and by the lower concentration of EDC.

Pressure drop and gas volume

In Figure 8.5 the pressure drop and volume in the reactor are shown, where the volume is per kilogram of process gas.

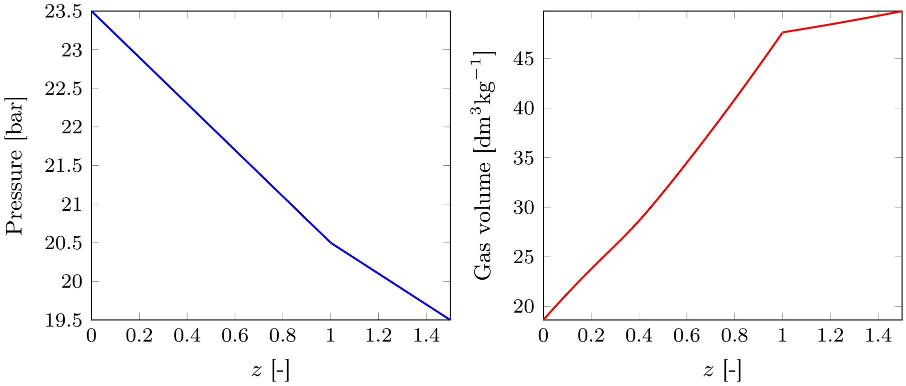

Figure 8.5. Pressure drop (left) and process gas volume per mass (right) through the firebox (up to $z = 1$) and the adiabatic volume (up to $z = 1.5$).

As Figure 8.5 illustrates, the pressure drop has the highest rate in the firebox section. The value of the linear pressure drop is decided a priori in the momentum balance of the model, as given in section 5.2. Hence, the model is not predictive with respect to pressure. However, the pressure drop shown in Figure 8.5 allows verification of the numerical integration through the reactor. In the firebox section, the pressure as shown in the plot is correctly ranging from 23.5 bar to 20.5 bar. In the adiabatic volume, the pressure ranges from 20.5 bar to 19.5 bar, where 19.5 bar is the pressure at the quenching point of the cracker. More complex pressure drop relations are given in the EDC pyrolysis literature, e.g. taking into account the higher pressure drop in the bending zones of the reactor [7].

The components are modeled using the ideal gas equation of state, as discussed in section 5.6. Thus, the observed volume profile is inversely proportional to the a priori given pressure profile.

8.2 The extended kinetic model - nominal case

Simulation with the nominal feed composition were conducted, with initial feed composition values from Table 5.2 in Chapter 5. This composition is based on average values from INEOS' plant from the last 12 months. In this simulation, the flue gas temperature, T_f, was given the value 1170 K (896 °C).

Key results from extended kinetic model - nominal case

The key values obtained in the simulation case with the extended kinetic model and the nominal feed composition are given in Table 8.2.

Table 8.2. Key values obtained from simulations with extended reaction model, using the nominal feed concentration.

Variable	Model value	Measured value
Conversion, firebox	55-57 wt%	53 wt%
Conversion, final	60 wt%	61 wt%
Selectivity	0.98	0.99
Temperature at outlet of firebox	482.0 °C	494.1 °C
Temperature, final	443.9 °C	453.6 °C

As for the global reaction model, Table 8.2 indicates that the conversion is underestimated in the firebox section. The temperature at the outlet of the firebox and the outlet of the adiabatic volume deviates with 2-3% from the measured values. The achieved selectivity deviates with 1% from the reported plant value. As the deviations are relatively small, the extended kinetic model give overall satisfactory results. Details and discussion of the results from this simulation are given in the next sections.

Products and byproducts

Product and byproduct mass fractions from simulation with the nominal feed composition are shown in Figure 8.6. Here, the curves of benzene and trichloroethylene are not included, as they are not formed or consumed in noticeable quantities according to the simulation. The nominal mass fractions of benzene and trichloroethylene are in the order of 10^{-3}. This is in accordance with the kinetic parameters of the Schirmeister model. In this kinetic model, benzene is only formed from acetylene, which also reacts to coke and HCl. The reaction where coke is formed seems to be favored as it involves the chlorine radical which is donated from both EDC and CCl_4.

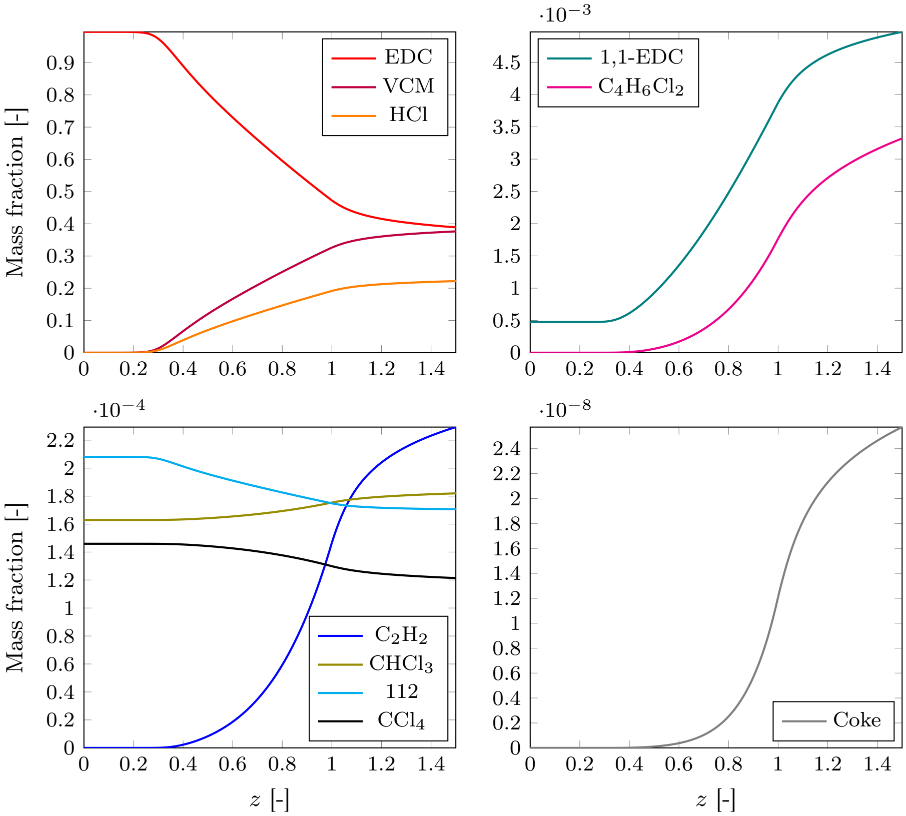

Figure 8.6. Mass fraction of products and byproducts, $T_f = 1170$ K, nominal feed composition. The component names are abbreviated in accordance with Table 6.3.

Comparison of the byproduct quantities (mass fractions) from the model with the plant data from INEOS reveal large deviations. As stated by Schirmeister et al., the kinetic constants were fitted to yield the empirically observed product composition of their technical plant. The adjustments were within ±5% for the main products, and as high as ±30% for the byproducts [5]. These adjustments could lead to large errors for the byproducts when applying this kinetic model to other plants than the one investigated by Schirmeister et al. Thus, other kinetic models should be investigated and possibly implemented, as discussed in section 9.4.

The observed rate of coke formation is directly related to the observed acetylene formation rate, as evident from Figure 8.6. This is due to the assumption by Schirmeister et al. that acetylene is the only coke precursor, shown explicitly in the coke reaction (reaction 31 in Table 6.2). Other studies (Borsa et al., Zychlinski et al.) that have been conducted suggest that the only species formation rate that correlates strongly with the rate of coke formation is that of chloroprene [26, 28]. These studies conclude that acetylene has a small impact. Thus, the assumption by Schirmeister et al. seems questionable, and the predicted coke formation rate from the current model should be used with care.

By studying Figure 8.7, it can bee seen that the total mass fraction of byproducts is below 10^{-2} up to approximately $z = 1$, or the end of the firebox section. This value seems to be reasonable and is in agreement with literature, where less than 1% of the mass of EDC is stated to be converted to byproducts [6,26]. After this point, the byproduct formation continues to increase in the adiabatic volume. In this simulation, the total relative increase of byproducts in the adiabatic volume is 28%. The relative increase of VCM is 15 % in the same section of the reactor.

Temperature profile: firebox and adiabatic section

The temperature profile from the simulation with the nominal feed concentration is given in Figure 8.8. At the four measurements points, the calculated temperature is in good agreement with the plant data. This is especially noticeable at the second measurement point, which coincides with an observed inflection point in the temperature profile at $z = 0.3$ and $T = 400$ °C. Compared to the temperature profile from the simulation with the global reaction model, as shown in Figure 8.2, it is clear that the two profiles are distinctly different. While both match the plant data with reasonable accuracy, the trends displayed are opposite. The global reaction model displays a continuous temperature increase through the reactor, while the Schirmeister model has an inflection point. As both are close to the plant values, it can be argued that they are both equally correct based on only these points.

In both the simulation with the global reaction model and the extended kinetic model, the same heat transfer model is used (but with a small difference in flue gas temperature). Thus, the observed difference of the two temperature

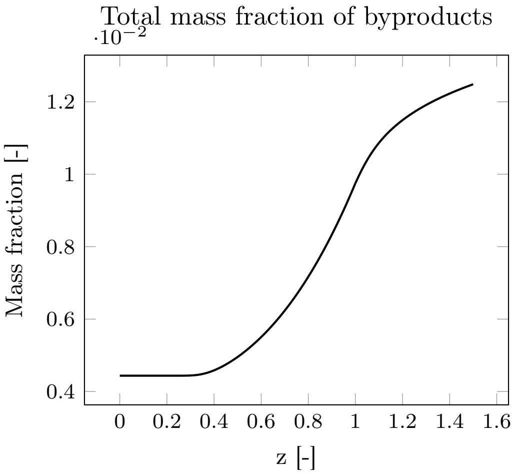

Figure 8.7. Total mass fraction of byproduct, nominal feed concentration scenario.

profiles is thus assumed to be caused by the kinetics. There seems to be a factor which slows the temperature increase at the inflection point for the Schirmeister model, giving a slope close to zero at this point. This could indicate that the reactions have been suppressed up to this point, possibly by temperature. As the Schirmeister model includes radicals, a sudden high increase in reaction rates is expected when the reactions first starts to occur in the reactor. When this critical point is reached, the reaction rate could get a high increase, leading to a greater absorption of heat and decrease in the temperature slope. The temperature profile for the global kinetic model indicates that the reaction rates are balanced by the heat load, as the temperature profile has a more stable profile. Simulating with discretised temperatures rather than an isothermal flue gas temperature for the extended kinetic model, could possibly give a more similar temperature profile to the one obtained by the global reaction model. At the industrial cracker, the most powerful burners are placed at the beginning of the reactor. This gives a better control of the temperature profile, and thus gives more control of the reaction rates. Discretizing of the furnace into zones with respective isotherm temperatures is hence one of the suggestions for future work (see section 9.4).

In the adiabatic section, the temperature profile is lower than the measured values, but only deviates with between 2% and 3% at the two measurement points. Except from this small deviation, it is observed that the curve is continuously declining which is consistent with the endothermic nature of the overall reaction.

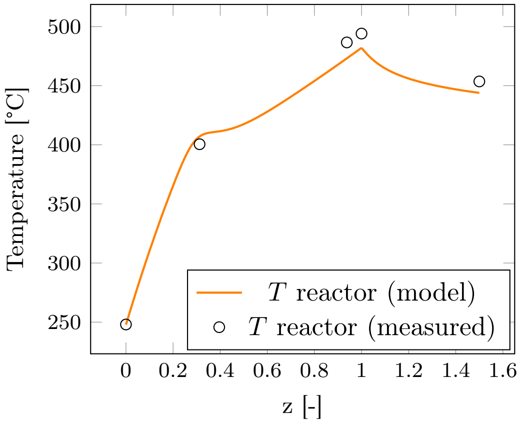

Figure 8.8. Temperature profile obtained from simulation with the nominal feed concentration and the Schirmeister kinetic model.

Conversion and selectivity

The final conversion and selectivity are predicted with small deviation from plant data (as shown in Table 8.2). In Figure 8.9, the profiles of conversion and selectivity through the firebox section and the adiabatic volume are given. Note that selectivity is plotted from the point where a detectable amount of EDC has reacted, as it does not makes sense to look at this variable until the reactions have started.

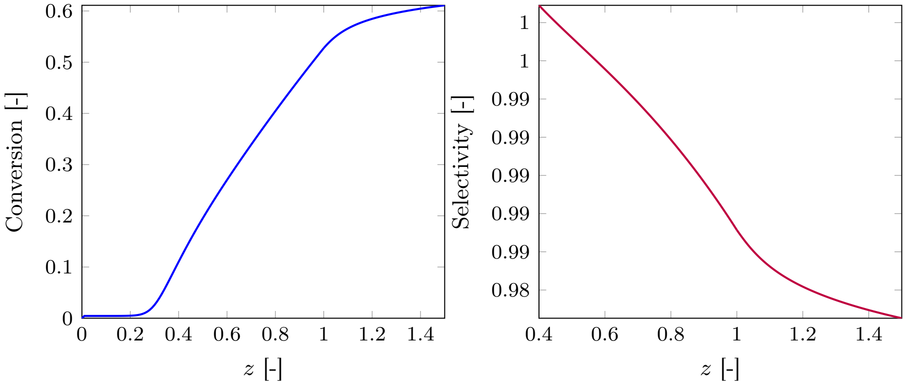

Figure 8.9. Conversion (weight basis) and selectivity (mole basis). Note that selectivity is plotted from $z = 0.4$, as it does not makes sense to look at this variable until the reactions have started.

The observed trend from Figure 8.9 is that the selectivity decreases as the conversion increases. The conversion profile is observed to stabilize in the adiabatic section. This is due to the decrease in temperature in the adiabatic section. Nevertheless, the selectivity is still high due to the fact that the formation of byproducts is still relatively low, according to this simulation.

8.3 Effect of temperature

As it is of interest to investigate the effect of temperature on conversion and byproduct formation, simulation with the nominal feed concentration was also performed with a lower flue gas temperature. The flue gas temperature was given the value T_f = 1160 K, and this case is compared to the simulation with T_f = 1170 K in Figure 8.10 and 8.11. For both cases the nominal feed composition was used.

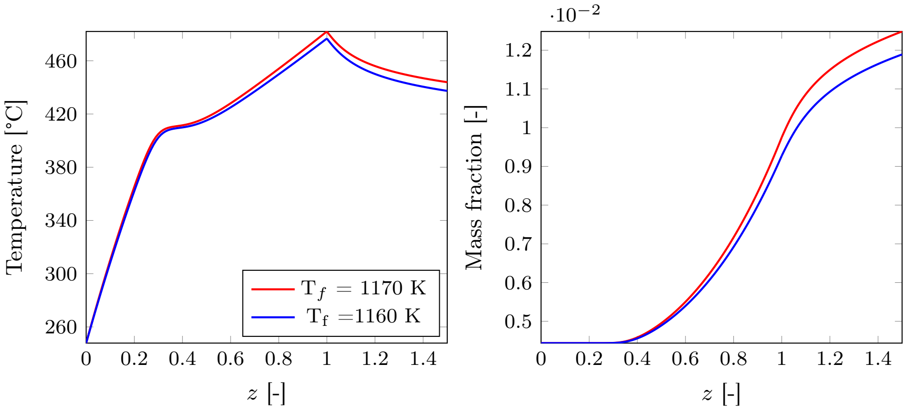

Figure 8.10. Temperature profile and total mass fraction of byproducts. T_f = 1160 K (887 °C) and 1170 K (897 °C).

From Figure 8.10, it is observed that for a lower flue gas temperature and thus a lower process gas temperature, the total amount of byproducts decreases. This is explained by the higher temperature which yields a higher cracking conversion for the endothermic reactions, as shown in Figure 8.11. The lowered selectivity is connected to the increase in byproducts. In the adiabatic volume the increase in byproduct formation accompanied by a decline in selectivity is particularly evident. This observation is in agreement with the literature, where conversion is reported to be kept at low values to avoid a high formation of byproducts and a low selectivity [5, 6].

8.4 Effect of promotors and inhibitors

To investigate the effect of promotors and inhibitors on the cracking process, simulation with varying concentration of CCl_4 (promotor) and 1,1-EDC (in-

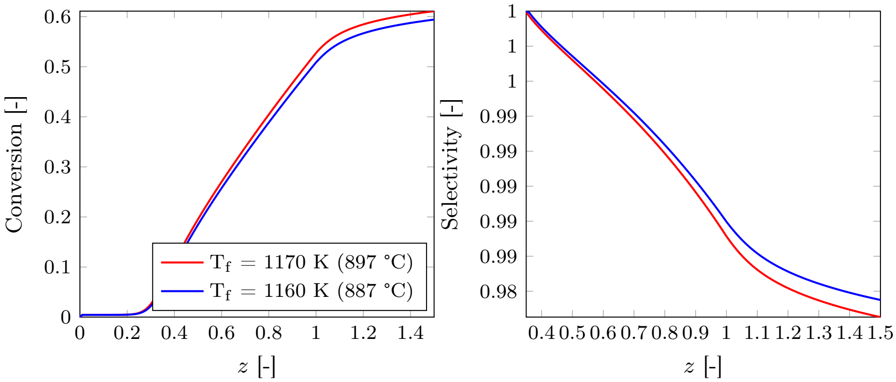

Figure 8.11. Conversion (left) and selectivity (right) as a function of reactor coordinate, z, for flue gas temperature, T_f = 1160 K (887 °C) and 1170 K (897 °C).

hibitor) were conducted.

Effect of promotor - carbon tetrachloride (CCl_4)

To investigate the isolated effect of the promotor, simulations were performed with a feed of pure EDC and a varying concentration of CCl_4; 0 ppm, 146 ppm (which is the nominal value), 400 ppm, 800 ppm, 1200 ppm and 2000 ppm, on a weight basis. A flue gas temperature of 1170 K (897 °C) was used in the simulations with the extended kinetic model. In Figure 8.12 and 8.13, the effect of the promotor is illustrated, in the plots of selectivity and conversion, process gas temperature and total byproduct formation.

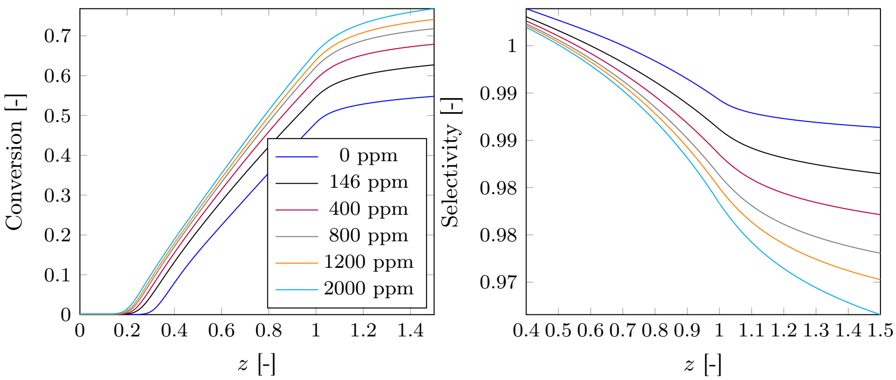

Figure 8.12. Conversion and selectivity for varying inlet concentration of the promotor CCl_4.

Figure 8.12 suggest that the kinetic model is sensitive with respect to the concentration of the promotor CCl_4, and even small additions of promotor cannot be neglected. This effect of CCl_4 is notably evident comparing the case with no addition of promotor with the cases that have CCl_4 in different concentrations in the feed stream. The suggested trend is that conversion increases and selectivity decreases, in accordance with theory [5]. The promotor behaves as expected, and enhances the reaction of EDC to VCM, HCl and byproducts. As described in Chapter 2, the role of the promotor in the reaction mechanism is to donate Cl radicals which enables the propagation of the reactions.

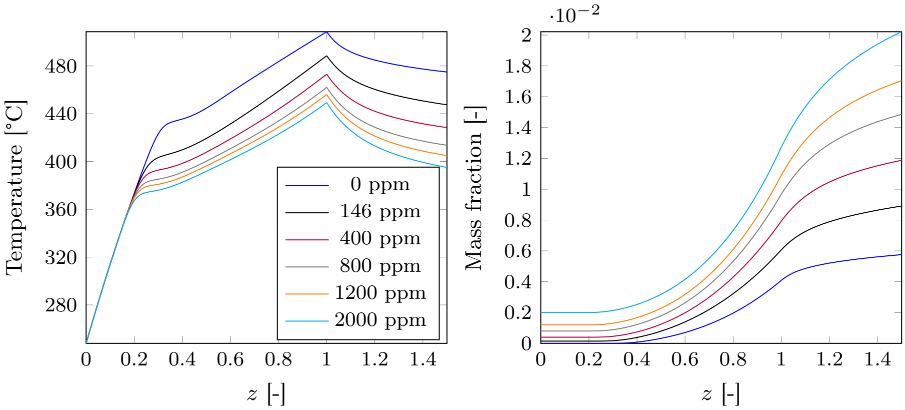

Figure 8.13. To the left: Temperature profile in firebox section (up to $z = 1$) and the adiabatic section (up to z=1.5), for varying feed concentrations of CCl_4. To the right: total mass fraction of byproducts formed with different CCl_4 concentrations.

It is seen from the plots in Figure 8.13 that as the conversion increases and selectivity declines, the temperature decreases and total mass of byproducts increases. However, the temperature of the respective cases of promotor concentrations do not differ until the reactions start. These trends are correlated to the increased heat absorption as a result of the enhanced reactions, leading to a lower process gas temperature. In the adiabatic volume, the effect of the promotor is the most evident. Here, the concentration of EDC is decreased compared to the feed value, and thus the promotor is an even more important contributor for the propagation of the reactions, providing Cl radicals for the chain propagation. The increase in byproduct formation seems to be an effect of the increased conversion, and not directly a cause of the promotor itself.

From experiments performed by INEOS [15], a decrease in outlet temperature of the firebox of up to 20 °C was experienced by increasing the CCl_4 concentration from approximately 100 ppm to 2000 ppm. In the current simulations, comparing the case with 146 ppm with the one of 2000 ppm CCl_4, the difference in outlet temperature of the firebox (at $z = 1$) is approximately 40 °C (449 °C for 2000 ppm CCl_4 and 488.5 °C for the case with 146 ppm CCl_4). However, in the experiments performed by INEOS, the conversion of EDC was held approximately constant by controlling the heat load to the cracker. In the simulations, the flue gas temperature was given the same value for all simulations, $T_f = 1170K$. Thus, the conversion was not attempted to be controlled. This justifies the larger observed effect of increasing the promotor concentration, compared with the experimental data from INEOS. For the simulation with 2000 ppm CCl_4, the conversion is 76 wt.%. This large increase in conversion is followed by a large decline in process gas temperature (as the cracker reactions absorb more heat), which explains the large temperature difference for the simulations. To summarise this, the *qualitative* trends of CCl_4 are as expected from a promotor. The *quantitative* effect of the promotor cannot be directly compared to the experimental data, due to difference in operational conditions.

Effect of inhibitor, 1,1- Dichloroethane (1,1-EDC)

To investigate the effect of the inhibitor, 1,1-EDC, a varying feed concentration of this compound was used in simulations with the extended kinetic model. The values used for the simulations were 0 ppm, 476 ppm, 800 ppm, 1200 ppm and 2000 ppm. To study the effect at regular plant conversion (around 60%), the feed was also set to include 146 ppm CCl_4. Except from these two compounds, the feed was consisting of pure EDC.

In Figure 8.14, the conversion and selectivity for the different cases of feed (weight) concentration of 1,1-EDC are displayed. As seen in Figure 8.14, the effect of an increased concentration of 1,1-EDC is small. The final conversion is

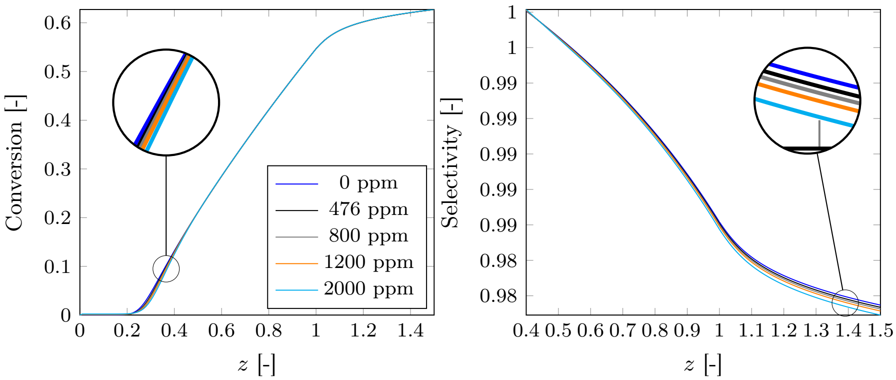

Figure 8.14. Conversion and selectivity for different feed concentrations of 1,1-EDC. The ppm values are on a weight basis.

approximately 63 wt% for each of the simulations. A small effect is observed for the selectivity, however this is almost negligible. Figure 8.15 gives the process gas temperature profile and the total mass of byproducts for the same cases as Figure 8.14.

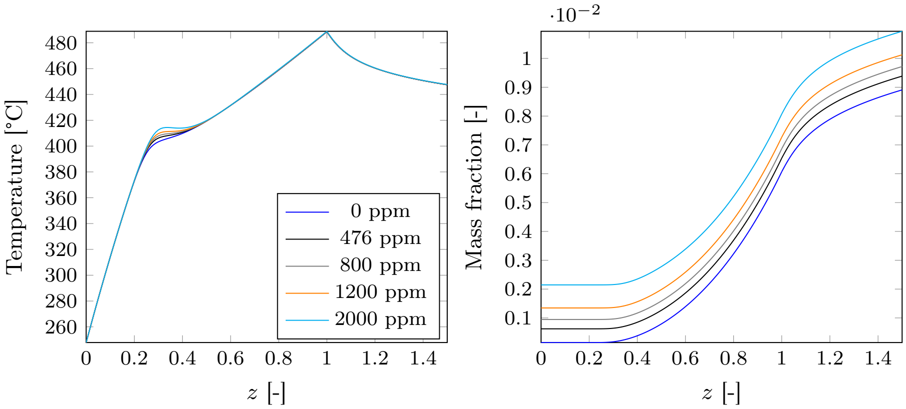

Figure 8.15. Temperature profile and total mass fraction of byproducts for varying concentrations of 1,1-EDC.

It is observed from Figure 8.14 that the effect of increasing the value of 1,1-EDC is small. There is no distinct temperature difference for the different scenarios. Figure 8.15 display an increase in byproduct quantity (mass fraction) for an increasing inlet concentration of 1,1-EDC. However, this increase is deemed to be a result of the increase in the inhibitor itself (regarding the value of the change from 0 ppm and 2000 ppm 1,1-EDC) and not from the increase in formation of other byproducts.

Hence, no clear inhibitory effect of 1,1-EDC was found in the simulations with the extended kinetic model. It could be that the effect of the promotor, CCl_4, is larger and is thus masking the effect of the inhibitor, 1,1-EDC. However, even for an inlet concentration of 2000 ppm 1,1-EDC and 146 ppm CCl_4, the effect is small. If the inhibitor has a large impact in the kinetic model, it would be expected that the effect should be notable for this case. The small decrease in conversion is more likely to be caused by the decrease in EDC concentration as a consequence of a less pure feed, than the inhibitor itself.

CHAPTER 9

CONCLUSION AND FURTHER WORK

In this study, a simulation model for a 1,2-dichloroethane (EDC) pyrolysis cracker has been developed and implemented in PYTHON. The framework PYTHON program is developed by Associate Professor Tore Haug-Warberg, and the program was modified and extended for this thesis. Two kinetic models were implemented, one based on plant data from INEOS (the *global* reaction kinetic model) and one extended kinetic model from literature (the *Schirmeister et al.* [5] kinetic model). The extended kinetic model includes the most important byproducts, in addition to one promotor (carbon tetrachloride, CCl_4) and one inhibitor (1,1-dichloroethane, 1,1-EDC). Additionally, a heat transfer model was developed, which was coupled to the kinetic model.

Simulations with the developed model have been performed, where different inlet conditions (initial values) have been tested. The simulation scenarios include simulation with the nominal feed concentration based on plant data from INEOS and simulations with varying flue gas temperature and inlet concentrations of the promotor, CCl_4 and inhibitor, 1,1-dichloroethane (1,1-EDC), respectively. The output data from the simulations were used both with respect to model validation and to evaluate the effect of the different inlet conditions on the cracking process.

9.1 Behavior of the model

Overall, the model is in good agreement with experimental data. The program behaves as desired for a wide range of initial values. However, the model seems to underpredict the conversion in the firebox section and overpredict the conversion in the adiabatic section, although the deviations are maximum 3% compared to the plant data. *Total* mass fraction of byproducts is predicted within reasonable values, but the model fails to predict quantities of the specific byproducts. The model framework provides a good basis for predictions of the cracker process, with room for improvements and further expanding the complexity of the model (see Further work below).

9.2 Effect of temperature, promotor and inhibitor

As the temperature in the reactor is increased, the observed trend is that the conversion and total quantity of byproducts increases, and selectivity decreases. An increased feed concentration of the promotor, CCl_4, is found to increase the conversion, while the outlet temperature is observed to decline. Even small feed concentrations of the promotor (100 ppm) has an effect on the cracking process, according to the simulations with extended kinetic model. No clear inhibitory effect was detected from the simulations with different inlet concentrations of the inhibitor, 1,1-EDC.

9.3 The adiabatic volume section

The simulations indicate that there is a large relative increase in byproduct formation in the adiabatic volume. Especially for the simulations with a large feed concentration of the promotor this trend was evident. This observation illustrates the tradeoff between running the process at greater conversions yielding a larger production rate of VCM, and maintaining the selectivity and purity of the product at desired values.

9.4 Further work

Improvements and extension of the developed cracker simulation model is possible. First of all, as the respective byproducts were not predicted well by the implemented kinetic model, it is recommended to implement additional kinetic models or to adjust the parameters in the Schirmeister model. This can be easily done, as the framework program has a very general form. For the heat model, more accurate temperature predictions might be achieved by discretizing the furnace into zones with different flue gas temperatures, rather than using one uniform temperature. Pressure drop could also be modelled in a more extensive way. Also part of the possible future work is extension of the model to include radiative effects, to obtain a two-dimensional model.

BIBLIOGRAPHY

[1] Chaochun Li, Guihua Hu, Weimin Zhong, Wangli He, Wenli Du, and Feng Qian. Coke deposition influence based on a run length simulation of a 1,2-dichloroethane cracker. *Industrial and Engineering Chemistry Research*, 52:17501–17516, 2013.

[2] Dietrich Braun. PVC - Origin, Growth and Future. *Journal of Vinyl & Additive Technology, December 2001*, 7(4):168–176, 2001.

[3] Karel Mulder and Marjolijn Knot. PVC plastic: A history of systems development and entrenchment. *Technology in Society*, 23:265–286, 2001.

[4] Michael W. Allsopp and Giovanni Vianello. Poly (Vinyl chloride). *Ullmann's Encyclopedia of Industrial Chemistry*, 1992.

[5] Reinhard Schirmeister, John Kahsnitz, and Michael Träger. Influence of EDC cracking severity on the marginal costs of vinyl chloride production. *Industrial and Engineering Chemistry Research*, 48:2801–2809, 2009.

[6] Borsa Alessandro G. Industrial Plant/Laboratory Investigation and Computer Modeling of 1,2-dichloroethane Pyrolysis, 1999.

[7] Byung-seok Choi, Joo Seok Oh, Sang-wook Lee, Hwayong Kim, and Jongheop Yi. Simulation of the Effects of CCl$_4$ on the Ethylene Dichloride Pyrolysis Process. *Industrial & Engineering Chemistry Research*, 40:4040–4049, 2001.

[8] E. Ranzi, M. Dente, and M. Rovaglio. Pyrolysis and Chlorination of Small Hydrocarbons, Chem. Eng. Comm., Vol. 117, 1992.

[9] Frank P Incropera, David P DeWitt, Theodore L Bergman, and Adrienne S Lavine. *Fundamentals of Heat and Mass Transfer*, volume 6th of *Dekker Mechanical Engineering*. John Wiley & Sons, 2007.

[10] Christie John Geankoplis. *Transport Processes and Separation Process Principles.* Prentice Hall Professional Technical Reference, 4th edition, 2009.

[11] E. N. Bird, B. R., Stewart, W. E., Lightfoot. *Transport Phenomena.* John Wiley & Sons, New York, revised se edition, 2007.

[12] Tore Haug-Warberg. *Den termodynamiske arbeidsboken.* Kolofon Forlag AS, 2006.

[13] Alexandre C. Dimian and Costin Sorin Bildea. Vinyl Chloride Monomer Process. In *Chemical Process Design: Computer-Aided Case Studies*, chapter 7, pages 201–229. John Wiley & Sons, 2008.

[14] Younggeun Park, Byung Seok Choi, and Jongheop Yi. Simulation of imbalance reduction between two reactors in an ethylene dichloride cracker. *Chemical Engineering Science*, 60:1237–1249, 2005.

[15] Private communication with INEOS (Torbjørn Herder Kaggerud), May., 2015.

[16] D. H. R. Barton. The Kinetics of the Dehydrochlorination of Substituted Hydrocarbons. Part I. Induced Dehydrochlorination. (14), 1948.

[17] D. H. R. Barton and K. E. Howlett. Kinetics of the Dehydrochlorination of Substituted Hydrocarbons. Part II. The Mechanism of the Thermal Decomposition of 1:2-Dichloroethane. *J. Chem. Soc.*, pages 156–164, 1949.

[18] K. E. Howlett. The pyrolysis of 1 : 2-dichloroethane. *Transactions of the Faraday Society*, 48:25, 1952.

[19] K. A. Holbrook, R. W. Walker, and W. R. Watson. The Pyrolysis of 1,2-Dichloroethane. *Journal of the Chemical Society B: Physical Organic*, pages 577–582, 1971.

[20] W Gardner, J Owen, and R Sutton. Chlorine-catalysed Pyrolysis of 1,2-Dichloroethane —Experimental results and proposed mechanism. *Journal of the Chemical Society, Faraday Transactions 1: Physical Chemistry in Condensed Phases*, pages 657–676, 1982.

[21] Joseph a. Incavo. A Detailed Quantitative Study of 1,2-Dichloroethane Cracking to Vinyl Chloride by a Gas Chromatographic Pyrolysis Device. *Industrial & Engineering Chemistry Research*, 35(1956):931–937, 1996.

[22] G. Huybrechts and G. Wouters. Mechanism of the pyrolysis of 1,2-dichloroethane in the absence and presence of added chlorine. *International Journal of Chemical Kinetics*, 34(Table I):316–321, 2002.

[23] Ki Yong Lee. Numerical Simulations of the Pyrolysis of 1 , 2 Dichloroethane. *KSME International Journal*, 16(1):102–108, 2002.

[24] S. H. Mousavipour, V. Saheb, F. Pirhadi, and M. R. Dehbozorgi. Experimental and theoretical study on the kinetics and mechanism of thermal decomposition of 1,2-dichloroethane. *Journal of the Iranian Chemical Society*, 4(3):279–298, 2007.

[25] Isao Mochida, Tadanori Tsunawaki, Chiaki Sotowa, and Yozo Korai. Coke Produced in the Commercial Pyrolysis of Ethylene Dichloride. *Industrial & Engineering Chemistry Research*, 35(96):3803–3807, 1996.

[26] Alessandro G. Borsa, Andrew M. Herring, J. Thomas McKinnon, Robert L. McCormick, and Glen H. Ko. Coke and Byproduct Formation during 1,2-Dichloroethane Pyrolysis in a Laboratory Tubular Reactor. *Industrial & Engineering Chemistry Research*, 40:2428–2436, 2001.

[27] Alessandro G. Borsa, Andrew M. Herring, J. Thomas McKinnon, Robert L. McCormick, Shinji Yamamoto, Yasunobu Teraoka, and Yukikazu Natori. Characterization of Coke Formed in Vinyl Chloride Manufacture. *Industrial & Engineering Chemistry Research*, 38:4259–4267, 1999.

[28] W Zychlinski, FD Kopinke, D Rodewald, and G Boettger. The coke formation during the pyrolysis of 1, 2-dichloroethane-results of radiotracer experiments. 1990.

[29] Tore Haug-warberg. Plug Flow Reactor Part III . Modelling Issues. 2011.

[30] H.a. Jakobsen. *Chemical Reactor Modeling, Multiphase Reactive Flows.* Springer, second edi edition, 2008.

[31] H. Scott Fogler. Elements of chemical reaction engineering. *Chemical Engineering Science*, 42:1000, 1999.

[32] R Viskanta and M. P. Mengüç. Radiation heat transfer in combustion systems. *Progress in Energy and Combustion Science*, 13(2):97–160, 1987.

[33] Peiyong Wang, Faqing Fan, and Qiong Li. Accuracy evaluation of the gray gas radiation model in CFD simulation. *Case Studies in Thermal Engineering*, 3:51–58, 2014.

[34] J H Lienhard. Heat Transfer. *Journal of Heat Transfer*, 82(1):198, 2010.

[35] Hoyt C. Hottel. Radiant heat transmission. In Editor. McGraw-Hill, McAdams WH, editor, *Heat transmission.* New York, 1954.

[36] A. Soufiani and E. Djavdan. A comparison between weighted sum of gray gases and statistical narrow- band radiation models for combustion applications. *Combustion and Flame*, 97(2):240–250, 1994.

[37] Myoung Jong Yu, Seung Wook Baek, and Jae Hyun Park. Extension of the weighted sum of gray gases non-gray gas radiation model to a two phase mixture of non-gray gas with particles. *International Journal of Heat and Mass Transfer*, 43(10):1699–1713, 2000.

[38] Eric Jones, Travis Oliphant, Pearu Peterson, and Et Al. SciPy: Open source scientific tools for Python.

[39] John Denholm Lambert. *Numerical methods for ordinary differential systems: the initial value problem.* John Wiley & Sons, Inc., 1991.

[40] Kenneth J. Beers. *Numerical Methods for Chemical Engineering - Applications in Matlab.* 2006.

[41] Erwin Kreyszig. *Advanced Engineering Mathematics.* John Wiley & Sons, 9th editio edition, 2006.

[42] Mark. E. Davis. *Numerical Methods & Modeling for Chemical Engineers.* John Wiley & Sons, New York, 1984.

[43] John C. Butcher. *Numerical Methods for Ordinary Differential Equations.* Second edition, 2008.

[44] R. L. Rowley and Et al. *DIPPR data compilation of pure chemical properties.* Design Institute for Physical Properties, 2006.

[45] Luciane S. Ferreira and Jorge O. Trierweiler. Modeling and simulation of the polymeric nanocapsule formation process. *IFAC Proceedings Volumes (IFAC-PapersOnline)*, 7(PART 1):405–410, 2009.

[46] H.a.J. Vercammen and G.F. Froment. An improved zone method using monte carlo techniques for the simulation of radiation in industrial furnaces. *International Journal of Heat and Mass Transfer*, 23(3):329–337, 1980.

[47] B. Leckner. Spectral and total emissivity of water vapor and carbon dioxide. *Combustion and Flame*, 19(1):33–48.

[48] T. H. Kaggerud. *Modeling an EDC Cracker using Computational Fluid Dynamics (CFD).* Master thesis, Norwegian University of Science and Technology, 2007.

[49] Y. S. Touloukian, P. E. Liley, and S.C. Saxena. Thermal conductivity. Nonmetallic liquids and gases, volume 3. In *Thermophysical properties of matter.* IFI/ Plenum., second edi edition, 1977.

[50] Malcolm W Chase. JANAF thermochemical tables. *JANAF thermochemical tables, by Chase, MW Washington, DC: American Chemical Society; New York: American Institute of Physics for the National Bureau of Standards, c1986.. United States. National Bureau of Standards.*, 1, 1986.

[51] A. E. Shilov and R.D. Sabirova. Mechanism of the Primary Act of the Thermal Decomposition of Methane Derivatives. *Zh. Fiz. Khim.*, 6, 1959.

[52] M Schneider and J. Wolfrum. Mechanisms of By-Product Formation in the Dehydrochlorination of 1,2-Dichloroethane. *Berichte der Bunsengesellschaft für physikalische Chemie*, pages 1058–1062, 1986.

[53] Sidney W. Benson and Maia Weissman. Mechanism of the pyrolysis of C$_2$HCl$_5$, molecular and radical steps. *International Journal of Chemical Kinetics*, 14(12):1287–1304, 1982.

[54] Mikhail G. Bryukov, Irene R. Slagle, and Vadim D. Knyazev. Kinetics of reactions of Cl atoms with ethane, chloroethane, and 1,1,-dichloroethane. *Journal of Physical Chemistry A*, 107(34):6565–6573, 2003.

[55] Selim M Senkan and David Quam. Correlation of Reaction Rate Coefficients for the Abstraction of Hydrogen Atoms from Organic Compounds by Chlorine Radical Attack. 10842(13):10837–10842, 1992.

[56] P. Goldfinger, G. Huybrechts, and G. Martens. Elementary Rate Constants in Atomic Chlorination Reactions, Part 2. *Laboratoire de Chimie Physique I, Universite de Bruxelles*, 1961.

[57] Geoffrey F. Hewitt. *Heat exchanger design handbook vol. 98.* Begell House, 2008.

[58] Special Metals Corporation. INCOLOY alloy 800H & 800HT. pages 1–16, 2004.

Appendices

APPENDIX A

THERMODYNAMIC DATA

The ideal gas model is used for thermodynamic calculations. Thus, ideal gas heat of formation for the respective compounds in the model are required. This appendix includes the thermodynamic data used in the models, and a comparison between the utilized DIPPR heat capacity model with values from the JANAF tables [50].

A.1 Thermodynamic data for process gas

Table A.1 gives the enthalpies of formation and the absolute entropies for ideal gas, which are used in the Schirmeister kinetic model. The values for 1,2-dichloroethane, vinyl chloride monomer and hydrochloric acid are also used in global reaction model. Values are taken from the DIPPR96 database [44].

Table A.2 gives the ideal gas heat capacity coefficients for the DIPPR ideal heat capacity calculation. Shorts forms are used in this table, see Table A.1 above for full names.

A.2 Comparison of Cp model

The C_p model used in the thesis is the DIPPR model. To verify the implementation of this heat capacity model, comparisons with table values from JANAF were made. If the JANAF values are correct, this means that also the obtained DIPPR values are valid. All of the compounds were not found in the JANAF tables, hence comparison for all compounds were performed. An example, where heat capacity of HCl calculated from the two models are compared, is given in Figure A.1. In this plot, the two models seems to be in good agreement for the calculation of the heat capacity.

Table A.1. Ideal gas heat of formation and absolute entropy, obtained from DIPPR96.

Compound	h_0^{ig}, J kmol^{-1}	s_0^{ig}, J kmol^{-1} K
1,2- dichloroethane	-129790000.0	308280.0
Vinyl chloride	28450000.0	273540.0
Hydrochloric acid	-92310000.0	186786.0
Trichloromethane	-102900000.0	295600.0
Carbon tetrachloride	-95810000.0	309910.0
Ethylchloride	-112260000.0	275780.0
1,1-dichloroethane	-129410000.0	305010.0
1,1,2-dichloroethane	-142000000.0	337100.0
1,1,1,2-tetrachloroethane	-149400000.0	355850.0
1,1-cis-dichloroethylene	2600000.0	287870.0
Trichloroethylene	-9620000.0	325090.0
Chloroprene	73010000.0	320600.0
Acetylene	228200000.0	200810.0
Benzene	82880000.0	269300.0
3,4-dichlorobutene	-64400000.0	371000.0
Carbon (soot/coke)	716680000.0	157991.0

Table A.2. Ideal gas heat capacity coefficients, obtained from DIPPR96.

Compound	c_1, J kmol^{-1} K	c_2, J kmol^{-1} K	c_3, K	c_4, J kmol^{-1} K	c_5, K
EDC	65271.0	112540.0	1737.6	87800.0	795.45
VCM	42364.0	87350.0	1649.2	65560.0	739.07
HCl	29157.0	9048.0	2093.8	-107.0	120.0
$CHCl_3$	39420.0	65730.0	928.0	49300.0	399.6
CCl_4	37582.0	70540.0	512.1	48500.0	236.1
EC	5680.0	129670.0	1599.2	85900.0	708.8
1,1	55210.0	120500.0	1502.0	87190.0	653.5
1,1,2	66554.0	112570.0	1545.4	97196.0	717.04
1,1,1,2	73037.0	108350.0	1235.6	87500.0	-555.21
Di	53886.0	78062.0	1609.4	66979.0	705.58
Tri	58086.0	73380.0	1232.0	64206.0	-549.52
CP	57090.0	147540.0	1193.4	97060.0	517.5
C_2H_2	31990.0	54240.0	1594.0	43250.0	607.1
C_6H_6	44420.0	232050.0	1494.6	172130.0	678.15
$C_4H_6Cl_2$	140940.0	126000.0	1274.0	-59100.0	6.61
C	20733.0	3680.0	6582.0	230.0	450.0

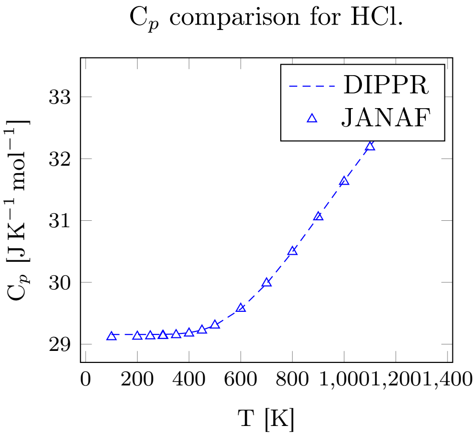

Figure A.1. C_p comparison for HCl.

APPENDIX B

KINETIC PARAMETERS

The corresponding rate parameters for the Schirmeister reaction model are listed in Table B.1. These are taken from Schirmeister et al. [5]. The origin of the parameters are given in the *Reference* column. To read more about how the kinetic parameters are estimated numerically and experimentally, these references offer more extensive details.

Table B.1. Rate law parameters from Schirmeister et al [5]. A is the frequency factor, E_a is the activation energy and n is the reaction order. Origin of the parameters is cited.

No.	A $[\mathrm{cm}^{3(n-1)}\mathrm{mol}^{-(n-1)}\mathrm{s}^{-1}]$	E_a $[\mathrm{kJ\ mol}^{-1}]$	n	Reference
1	$5.9 \cdot 10^{15}$	342	1	Barton [17], Huybrecths [22]
2	$2.2 \cdot 10^{12}$	230	1	Shilov [51]
3	$1.3 \cdot 10^{13}$	7	2	Borsa [6], Huybrechts [22]
4	$1.2 \cdot 10^{13}$	34	2	Borsa [6]
5	$1.0 \cdot 10^{12}$	42	2	Borsa [6]
6	$5.0 \cdot 10^{11}$	45	2	Schirmeister [5]
7	$2.0 \cdot 10^{11}$	48	2	Schirmeister [5]
8	$1.0 \cdot 10^{11}$	56	2	Schirmeister [5]
9	$1.0 \cdot 10^{12}$	63	2	Borsa [6]
10	$9.1 \cdot 10^{10}$	0	2	Huybrechts [22]
11	$1.2 \cdot 10^{14}$	56	2	Schneider [52]
12	$5.0 \cdot 10^{11}$	31	2	Borsa [6]
13	$2.0 \cdot 10^{10}$	30	2	Schirmeister [5]
14	$3.0 \cdot 10^{11}$	61	2	Borsa [6]
15	$2.1 \cdot 10^{14}$	84	1	Benson [53], Ashmore [20]
16	$5.0 \cdot 10^{14}$	90	1	Schirmeister [5]
17	$2.0 \cdot 10^{13}$	70	1	Schirmeister [5]
18	$2.5 \cdot 10^{13}$	70	1	Benson [53]
19	$1.7 \cdot 10^{13}$	4	2	Bryukov [54]
20	$1.2 \cdot 10^{13}$	6	2	Bryukov [54]
21	$1.7 \cdot 10^{13}$	15	2	Senkan [55]
22	$1.7 \cdot 10^{13}$	17	2	Senkan [55]
23	$1.6 \cdot 10^{13}$	14	2	Goldfinger [56]
24	$5.0 \cdot 10^{11}$	33	2	Schirmeister [5]
25	$1.0 \cdot 10^{12}$	33	2	Borsa [6]
26	$5.0 \cdot 10^{11}$	33	2	Schirmeister [5]
27	$1.0 \cdot 10^{13}$	13	2	Borsa [6]
28	$1.0 \cdot 10^{13}$	12	2	Schirmeister [5]
29	$1.0 \cdot 10^{13}$	13	2	Schirmeister [5]
30	$1.0 \cdot 10^{14}$	20	2	Schirmeister [5]
31	$1.6 \cdot 10^{14}$	70	2	Borsa [6]

Appendix C

HEAT TRANSFER PARAMETERS

This appendix provides all the temperature dependent heat transfer parameters used in the heat transfer model of the thesis.

C.1 Flue gas heat parameters

Values of the flue gas parameters are obtained from Incropera and DeWitt [9]. In Table C.1 - C.8, the symbols T, μ, ν, k and Pr are used to denote temperature, dynamic and kinematic viscosity, thermal conductivity, and the Prandtl number, respectively.

Table C.1 - C.4 give the heat parameters for carbon dioxide (CO_2), nitrogen (N_2), oxygen (O_2) and water vapour (H_2O).

Table C.1. Heat transfer parameters for CO_2 (g)

T [K]	600	650	700	750	800
μ [10^7N s m^{-2}]	270	288	305	321	337
ν [10^6m^2 s^{-1}]	30.6	35.4	40.3	45.5	51.0
k [mW m^{-1} K]	40.7	44.5	48.1	51.7	55.1
Pr [-]	0.717	0.712	0.717	0.714	0.716

Table C.2. Heat transfer parameters for N_2 (g)

T [K]	600	700	800	900	1000	1100	1200
μ [10^7N s m^{-2}]	290.8	321.0	349.1	375.3	399.9	423.2	445.3
ν [10^6m^2 s^{-1}]	51.79	66.71	82.90	100.3	118.7	138.2	158.6
k [mW m^{-1} K]	44.6	49.9	54.8	59.7	64.7	70.0	75.8
Pr [-]	0.701	0.706	0.715	0.721	0.721	0.718	0.707

Table C.3. Heat transfer parameters for O_2 (g)

T [K]	600	700	800	900	1000	1100	1200
μ [10^7N s m^{-2}]	343.7	380.8	415.2	447.2	477.0	505.5	532.5
ν [10^6m^2 s^{-1}]	53.59	69.26	86.32	104.6	124.0	144.5	166.1
k [mW m^{-1} K]	47.3	52.8	58.9	64.9	71.0	75.8	81.9
Pr [-]	0.729	0.744	0.743	0.740	0.733	0.736	0.725

Table C.4. Heat transfer parameters for H_2O (g)

T [K]	600	650	700	750	800	850
μ [10^7N s m^{-2}]	206.7	224.7	242.6	260.4	278.6	296.9
ν [10^6m^2 s^{-1}]	56.60	66.48	77.26	88.84	101.7	115.1
k [mW m^{-1} K]	42.2	46.4	50.5	54.9	59.2	63.7
Pr [-]	0.993	0.996	1.00	1.00	1.01	1.02

C.2 Process gas parameters

For the process gas heat parameters, values from the Heat Exchanger Design Handbook [57]. The mixture values are obtained as if the gas was consisting only of 1,2-dichloroethane (EDC), vinyl chloride monomer (VCM) and hydrochloric acid (HCl). In the tables, the symbols T, μ, ν, k and Pr are used to denote temperature, dynamic and kinematic viscosity, thermal conductivity, and the Prandtl number, respectively. Table C.5 - C.7 provides the parameters for EDC, VCM and HCl, respectively.

Table C.5. Heat transfer parameters for EDC (g)

T [K]	273	298	373	473	573	673	773	873
μ [10^7N s m^{-2}]	8.46	9.20	11.38	14.21	16.95	19.64	22.27	24.85
k [mW m^{-1} K]	7.33	8.58	12.75	19.21	26.55	34.64	43.35	52.59
Pr [-]	0.86	0.84	0.79	0.76	0.72	0.69	0.67	0.64

Table C.6. Heat transfer parameters for VCM (g)

T [K]	273	298	373	473	573	673	773	873
μ [10^7N s m^{-2}]	9.35	10.24	12.80	16.01	19.01	21.83	24.50	27.03
k [mW m^{-1} K]	10.49	12.11	17.38	25.18	33.68	42.69	52.10	61.81
Pr [-]	0.73	0.73	0.73	0.73	0.72	0.71	0.69	0.68

Table C.7. Heat transfer parameters for HCl (g)

T [K]	273	298	373	473	573	673	773	873
μ [$10^7 \mathrm{N\,s\,m^{-2}}$]	13.40	14.64	18.30	23.02	27.51	31.73	35.63	39.17
k [$\mathrm{mW\,m^{-1}\,K}$]	13.10	14.41	18.15	22.76	26.95	30.78	34.28	37.49
Pr [-]	0.82	0.81	0.81	0.81	0.83	0.84	0.87	0.89

C.3 Coil material parameters

The heat properties of the coil material, INCOLOY alloy 800H, are found in Table C.8. Values are taken from *Special metals Corporation* [58].

Table C.8. Thermal conductivity of INCOLOY alloy 800H and 800HT.

Temperature [°C]	Thermal conductivity [$\mathrm{W\,m^{-1}\,°C^{-1}}$]
20	11.5
100	1.035
200	1.089
300	1.127
400	1.157
500	1.191
600	1.122
700	1.251
800	1.266
900	1.283
1000	1.291

Appendix D

EMISSIVITIES AND ABSORPTIVITIES

D.1 Coefficients for emissivity and absorptivity calculations

In Table D.1 and D.2, the coefficients for equation (7.7a) and (7.7b) in Chapter 7 are found, for water vapor and carbon dioxide. These are used to calculate the gas emissivity and gas absorptivity of water and carbon dioxide, according to Leckner [47].

Table D.1. Coefficients used in the estimation of absorptivity and emissivity of water, from Leckner [47].

i	c_{0i}	c_{1i}	c_{2i}
0	-2.2118	-1.1987	0.035596
1	0.85667	0.93048	-0.14391
2	-0.10838	-0.17156	0.045915

Table D.2. Coefficients used in the estimation of absorptivity and emissivity of carbon dioxide, from Leckner [47].

i	c_{0i}	c_{1i}	c_{2i}	c_{3i}
0	-3.9893	2.7669	-2.1081	0.39163
1	1.2710	-1.1090	1.0195	-0.21897
2	-0.23678	0.19731	-0.19544	0.044644

D.2 Plots of emissivity and absorptivity

Plots of the calculated total gas emissivities and absorptivities as a function of flue gas temperature, T_f and outer coil pipe temperature, $\mathrm{T_{po}}$, respectively, are found in Figure D.1 and D.2. For these calculations, the flue gas temperature was given the value $\mathrm{T_f} = 1170$ K. This value is changed for the simulations using other values for the flue gas temperature.

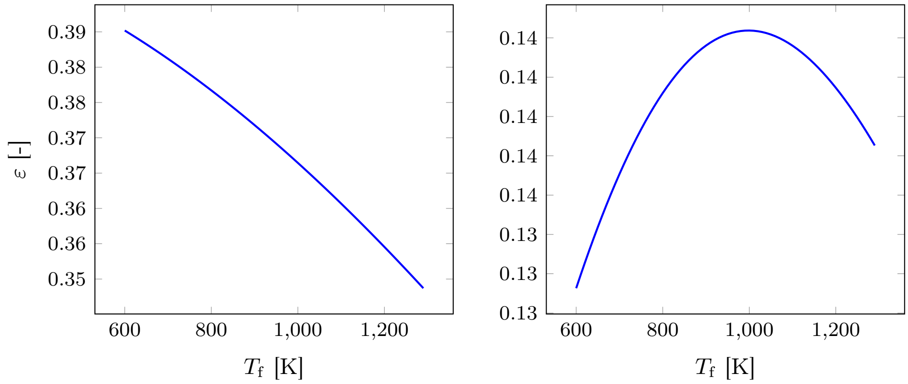

Figure D.1. Emissivity of H_2O (g) and CO_2 (g), as a function of flue gas temperature, T_f.

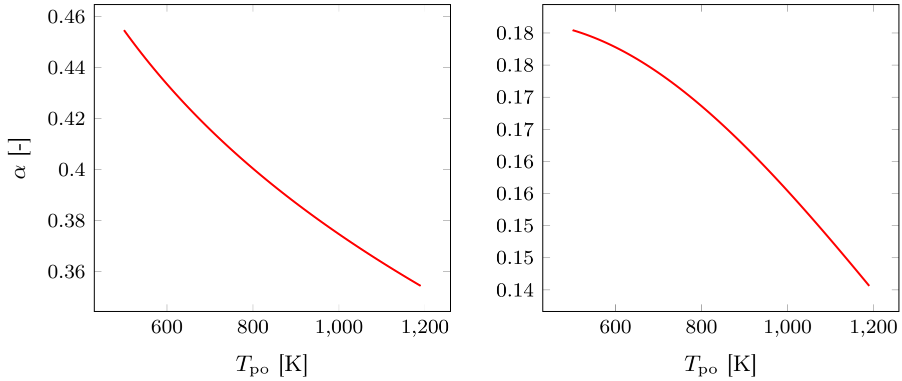

Figure D.2. Left: absorptivity of H_2O (g) and right: absorptivity of CO_2 (g), as a function of outer coil pipe temperature, T_po. Here, $\mathrm{T_f}$ is set to 1170 K.

Appendix E

COMBUSTION CALCULATIONS

E.1 Calculation of the required mass of fuel gas

For calculation of the convection coefficient of the flue gas, the velocity of the flue gas is needed to determine the nature of the flow (i.e. the Reynolds number). The first step to find this velocity is to find the required mass of fuel gas and air to give a fired heat rate of 17.2 MW. The mass and energy balances for the combustion process, under stationary, nonadiabatic conditions are given as

$$\dot{M}_{\text{fuel,air}} = \dot{M}_{\text{flue}} \triangleq \dot{M} \tag{E.1a}$$

$$\dot{H}_{\text{out}} - \dot{H}_{\text{in}} = \dot{M}(h_{\text{out}} - h_{\text{in}}) = \dot{Q}_{\text{comb}} \tag{E.1b}$$

where $\dot{H} = \dot{M}_{\text{f}} h$. The required mass of fuel gas and air, which is equal to the mass of flue gas, can then be calculated, setting the value of $\dot{Q}_{\text{comb}}$ to be 17.2 MW. Enthalpy change for the combustion process is shown in (E.2), using molar enthalpies.

$$\sum_{\text{prod.}} \dot{n}_{\text{out}} \left(\Delta_{\text{f}} h_i^0(T_{\text{in}}) + \int_{T_{\text{in}}}^{T_{\text{out}}} C_{p,i}(T)\text{d}T \right) - \sum_{\text{react.}} \dot{n}_{\text{in}} \Delta_{\text{f}} h_i^0(T_{\text{in}}) = \dot{Q}_{\text{comb}} \tag{E.2}$$

As T_{in} is set to 298 K (reference temperature), there is no C_p integral for the reactant enthalpies. The DIPPR model (ref. equation (5.16)) is utilised for the heat capacity function. The mole balances for the combustion reactions (equation (7.6a) - (7.6c)) are combined with equation (E.2) to calculate the number of moles of fuel and air. The mass flow is thus obtained through the molecular weights. Ideal gas law is then used to calculate the volumetric flow rate of the flue gas. Finally, the velocity of the flue gas (which because of the buoyancy is flowing upwards and exits at the stack), u_f $[\mathrm{m\,s^{-1}}]$, is calculated by dividing the volumetric flow rate V_f $[\mathrm{m^3 s^{-1}}]$ by the cross section area of the furnace, A_f.

$$u_\mathrm{f} = \frac{\dot{V}_\mathrm{f}}{A_\mathrm{f}} \tag{E.3}$$

Appendix F

VERIFICATION OF THE ODE SOLVERS

To verify the integrators implemented in the framework PYTHON program, the integrators were tested for a set of two differential equations with a known analytical solution. In Figure F.1 and F.2, the solutions obtained by integrating with the numerical integrators `odeint` and `ode` from `Scipy` are given. As shown, the deviation is negligible for two integrators for this specific set of integrators. This does not necessarily mean that they are able to integrate other systems of differential equations, however the test provide a confirmation of the expected behavior in this case.

F.1 Comparison of integrators with analytical solution

The set of differential equations which was tested is given in equation (F.1).

$$\begin{pmatrix} \mathrm{d}x/\mathrm{d}t \\ \mathrm{d}y/\mathrm{d}t \end{pmatrix} = \begin{pmatrix} 0 & 1 \\ \text{-c} & 0 \end{pmatrix} \quad \begin{pmatrix} x \\ y \end{pmatrix} \tag{F.1}$$

In this equation, c is an arbitrary constant, which in this case was set to $c = 1$. The analytical solution for this case is:

$$x = x_0 \cos \sqrt{c}t + y_0 \frac{1}{\sqrt{c}} t \sin \sqrt{c}t$$
$$y = -x_0 \sqrt{c} \sin \sqrt{c}t + y_0 \cos \sqrt{c}t$$

For the calculations, the initial conditions are set to the following values.

$$x_0 = 1, y_0 = 0$$

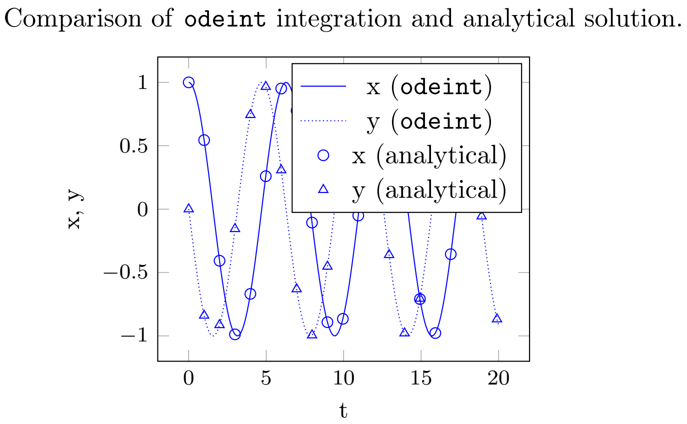

Comparison of `odeint` integration and analytical solution.

Figure F.1. Solution of differential equation with `odeint`.

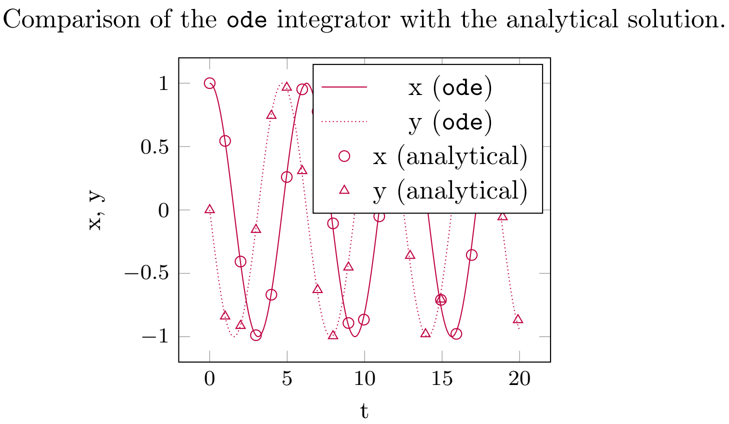

Comparison of the `ode` integrator with the analytical solution.

Figure F.2. Solution to differential equation set with `ode`.